UNIVERSITY OF THE WEST OF SCOTLAND

DOCTORAL THESIS

Photoacoustic Analyzer for Natural Gas and Short-Chain Hydrocarbon Isotopologues

Author:
Marc-Simon BAHR

Supervisors:
Prof. Des GIBSON
Prof. Marcus WOLFF

A thesis submitted in fulfillment of the requirements for the degree of Doctor of Philosophy

in the

School of Computing, Engineering and Physical Sciences

November 2023

Declaration

I declare that this thesis has been composed by myself.
No portion of this work referred to in this thesis has been submitted in support of an application for another degree or qualification of this or any other university or institute of learning.

Acknowledgements

I would like to take this opportunity to thank my Lead Supervisors Prof. Des Gibson and Dr. David Hutson and my Assessor Dr. Carlos Garcia Nunez at the University of the West of Scotland, for their support and numerous consultations throughout my doctoral studies.

My special thanks go to Prof. Marcus Wolff, who supervised me at the Hamburg University of Applied Sciences, initiated the entire research project at the Heinrich Blasius Institute for Physical Technologies and allowed me to join the project. Without his outstandig support, guidance and comprehensive knowledge it would not have been possible to realize this project.

Furthermore, my special thanks go to Bernd Lübbers. He introduced me to the subject of gas chromatography with his excellent knowledge through a multitude of discussions and on-site support.

UNIVERSITY OF THE WEST OF SCOTLAND

Abstract

School of Computing, Engineering and Physical Sciences

Doctor of Philosophy

Photoacoustic Analyzer for Natural Gas and Short-Chain Hydrocarbon Isotopologues

by Marc-Simon BAHR

One of the most important energy sources of our time is natural gas. Knowledge of its composition, whose main part is methane (75-99% on average), allows a variety of conclusions to be drawn, including its origin and energy content. This information is of great importance for both the natural gas producer and the end user. In discussions, the main driver of climate change is quickly identified: carbon dioxide (CO_2) emissions. In fact, methane (CH_4) as a short-chain hydrocarbon has a 34 times greater negative impact on global warming than CO_2. For this reason, it is essential to be able to identify the sources of hydrocarbons, especially methane. There are existing two main methane-isotopologues $^{12}CH_4$ and $^{13}CH_4$, whose natural abundance is 98.1% and 1.1%, respectively. Depending on the source, this shares varies, so that each source has a "fingerprint", defined as $\delta^{13}CH_4$ value on the basis of which the methane source can be traced. In addition to natural sources, such as thawing permafrost or cows, anthropogenic methane emissions occur during the extraction and transportation of natural gas. Furthermore, knowledge of the $\delta^{13}CH_4$ value of the methane main isotopologues of the natural gas allows further conclusions to be drawn regarding its maturity and the natural gas surrounding rock, which can be used to optimize the drilling technology. The object of this work is the development of a sensor based on photoacoustic spectroscopy (PAS) which, contrary to the usual field of application of PAS, namely the detection of trace gases, is capable of measuring concentrations of the main alkanes as well as of methane isotopologues. Since the alkanes show partly strongly overlapping absorption spectra, the determination of

the optimal average wavelength of the laser source used is not trivial, as far as different molecules have to be differentiated simultaneously. Therefore, a mathematical algorithm was developed which calculates the optimal wavelength based on the theoretical absorption spectra. The heart of the new sensor is an interband cascade laser (ICL), which emits in the mid-infrared range around 3.3 μm wavelength. By applying the injection-current modulation mode of the laser, it is possible to achieve accurate and precise measurement results. The behavior of the laser in this mode was initially unknown and has been analyzed in this work with a specially developed method. Calibration mixtures were produced, using a specially developed gas mixer, whose PA spectra detected by an analog microphone were recorded by the implemented digital signal processor (DSP) real-time signal processing. The resulting spectra were used to train the downstream machine-learning based algorithm Partial Least Squares Regression (PLSR), which subsequently determines the concentrations of the main methane isotopologues and the main alkanes. The evaluation of the developed sensor was carried out on the basis of prepared laboratory gas mixtures, as well as with the help of real natural gas samples from various sources11. It could be shown that PAS is suitable to determine highly concentrated natural gas with respect to the composition of the main alkanes but also the methane main isotopologues.

Contents

List of Figures

List of Tables

List of Abbreviations

AI	**A**rtifical **I**ntelligence
CRDS	**C**avity **R**ingdown **S**pectroscopy
DFB-ICL	**D**istributed-**F**eedback **I**nterband **C**ascade **L**aser
DC	**D**irect **C**urrent
DFT	**D**iscrete **F**ourier **T**ransformation
DSP	**D**igital **S**ignal **P**rocessor
GC	**G**as **C**hromatography
GWP	**G**lobal **W**arming **P**otential
IRMS	**I**sotope **R**atio **M**ass **S**pectroscopy
PA	**P**hoto **A**coustic
PAS	**P**hoto **A**coustic **S**pectroscopy
SNR	**S**ignal-to-**N**oise **R**atio
QTF	**Q**uartz **T**uning **F**ork

Chapter 1

Introduction

In 2022, the global primary energy consumption was 160,764 TWh. The energy share of natural gas was almost 25% (Our World in Data, 2022). At this point, it becomes clear how important natural gas still is as an energy source worldwide. As a result of millions of years of biological processes, the underground energy-rich gas accumulations are the target of the gas extraction industry worldwide. The exact composition of natural gas, which consists primarily of short-chain hydrocarbons, provides both natural gas producers and end users a variety of important information. Thus, the exact composition provides information about the origin of the natural gas and about its energy content (Faramawy et al., 2016). The latter in particular is important for both the natural gas producer and the end consumer. Knowledge of the composition allows valuable geological information and also provides information about the deposit itself (Wiersberg and Erzinger, 2007). The energy content provides both billing-relevant information and the basic information for the optimal control of its combustion process (Park et al., 2021; Leicher et al., 2017). From these facts, it is clear that a reliable in-situ real-time determination of the actual composition of the natural gas offers significant advantages and, in some cases, is indispensable. Gas chromatography (GC) is considered the gold standard for natural gas analysis (Karpash et al., 2010; ISO, 2012). The gas chromatograph used in this analysis technique offers very accurate and precise results with relative errors $< 2\%$ in a dynamic range with regard to the concentrations of the individual components from ppb (parts per billion) up to 100%, but requires different operating gases, e.g. helium, synthetic air and hydrogen, depending on the explicit configuration of the measurement system. The measurement time is up to 45 minutes depending on the selected resolution with respect to the molecule types. In addition, recurring calibration measurements are necessary to maintain the low measurement error (Poole, 2021).

While the climate-damaging effect of carbon dioxide (CO_2) is widely known, the up to 34-fold greater negative impact on global warming of methane, the main component of natural gas, is poorly acknowledged (Jacobson, 2021). The main reason is that the influences of the individual methane sources on climate change have been extremely insufficient characterized. The source types are known, but it is hardly possible to quantify the emissions of the methane sources on a global scale in order to develop mitigation strategies based on this. Each methane source has its individual so-called "methane signature", which results from the ratio of the two main methane isotopologues $^{12}CH_4/^{13}CH_4$. The two main isotopologues have a natural abundance of 98.9% and 1.1%, respectively. Depending on the explicit source, the ratio known as $\delta^{13}CH_4$ deviates from the standard Pee Dee Belemnite value, allowing conclusions to be drawn about the source (Schwietzke et al., 2016). In order to identify the source, it is therefore necessary to determine the ratio of the main methane isotopologues $^{12}CH_4/^{13}CH_4$ in the form of the $\delta^{13}CH_4$ value of a sample. Knowing the $\delta^{13}CH_4$ value of the methane in the natural gas reveals more information about the natural gas itself. Thus, statements can be made about its degree of maturity and origin. Valuable geological information can be obtained about the porosity and permeability of the rock containing the natural gas, which can be profitably used to optimize natural gas production (Zhang and Krooss, 2001).

Gas chromatography in combination with isotope ratio mass spectroscopy (GC-IRMS) is considered the gold standard for isotopologue analysis (Sessions, 2006). The gas chromatograph is extended by a mass spectrometer to determine the $^{12}CH_4/^{13}CH_4$ ratio and thus the $\delta^{13}CH_4$ value of a sample. This method provides extremely accurate results within the error range equivalent to gas chromatography or even better. However, several calibration measurements with standard samples are necessary during an operating day to maintain accuracy. The complexity of this measurement setup is very high. In addition, for technical reasons, the methane samples must be oxidized to CO_2 before the mass spectrometer can identify the isotopologue ratio (Rodrigues et al., 2013). Laboratory conditions are also essential for accurate and reproducible results. In-situ measurements are therefore impossible.

Another established method of $\delta^{13}CH_4$ analysis is Cavity Ring Down Spectroscopy (CRDS). This spectroscopic method also provides very precise measurement results with relative measurement errors in the per mil range in a

few seconds, but the interfering components must be known and their concentrations must not exceed limit values. While in-situ measurements are possible, the dynamic range in terms of concentration is significantly limited compared to GC-IRMS and is restricted to the ppm range, depending on the instrument. Furthermore, recalibration measurements are required within specified intervals to maintain precision (PICARRO, INC., 2022).

A sensor that can both analyze the major constituents of natural gas hydrocarbons and determine the $\delta^{13}CH_4$ value of methane, and perform these measurements in-situ in real time, without significant errors and cross-sensitivities would be a significant technological advance.

Photoacoustic spectroscopy (PAS) is an established method for the identification of trace gases (Palzer, 2020). The laser radiation emitted by a laser is absorbed by the gas molecules contained in the sample. Complex relaxation processes lead to energy conversions, which cause a temperature increase in the gas (Schilt et al., 2006). Due to the constant volume of the measuring cell, in which the sample is located, the pressure changes. This pressure change is detected by a sound detector, e.g. a microphone. The composition-dependent signal allows the quantitative determination of the gas molecules contained in the sample. Within the scope of this work, the applicability of this spectroscopy method for the analysis of the composition of natural gas with respect to the highly concentrated main alkanes, as well as the hydrocarbon isotopologues, and real natural gas samples is investigated.
In order to accurately determine the concentrations of the individual gas molecules, whose absorption spectra overlap strongly in some cases, a very narrow-band laser radiation source is required, which emits in the mid-infrared range around 3.3 μm wavelength. The distributed feedback interband cascade lasers (DFB-ICL) are semiconductor lasers which emit single-mode in the wavelength range in mention with a linewidth of less than 3 MHz (nanoplus, 2023). This enables high-resolution spectroscopy, which allows the differentiation of even strongly overlapping spectra and thus its gas molecules.
To enable real-time measurements, the measurement and demodulation of the photoacoustic signal is performed using an efficient implementation of the discrete fourier transform (DFT) on a digital signal processor (DSP) (Elliott, 1987). Since the resulting spectra are highly non-linear depending on the individual molecule concentrations, the quantiative evaluation requires artificial intelligence (AI). In this work, the applicability of the machine-learning

based Partial Least Squares Regression (PLSR) algorithm established for the evaluation of spectroscopic data is demonstrated. This algorithm is capable of quantitatively characterizing even complex mixtures with more than two gas components with respect to the individual concentrations (Zifarelli et al., 2020).
The sensor to be developed is validated with the help of artificial samples similar to natural gas produced in the laboratory, as well as with the help of real natural gas samples from various sources. The established GC acts as a reference.
PAS has already been successfully applied in its special embodiment as quartz enhanced photoacoustic spectroscopy (QEPAS) with respect to its applicability to artificial natural gas like samples (Luo et al., 2022). However, no analysis of real natural gas samples, which naturally contain a large number of residual components, was performed.

1.1 Project Description and Outline of the Thesis

The main goal of this research project is the development of a sensor which allows the detection of the main alkanes methane (CH_4), ethane (C_2H_6) and propane (C_3H_8) for natural gas like compositions in the high-percentage range and the methane main-isotopologues ($^{12}CH_4$ and $^{13}CH_4$), i.e. the $\delta^{13}CH_4$ value.
To achieve this aim, the following subtasks have to be completed:

- Determining the optimal center wavelength for PAS of main alkanes and methane isotopologues.
- Spectral characterization of injection-current modulated ICL.
- Development of a PA setup for main alkane detection and isotope-selective measurements, including the implementation of the machine learning algorithm Partial Least Squares Regression.
- Calibration of the sensor using calibration gas mixtures prepared with a gas mixer developed in-house.
- Validation of the sensor by measurements of real natural gas samples using GC reference.

The above mentioned points are corresponding to milestones of this project. Parts of their results have already been published in scientific journals. The

sensor to be developed is not a prototype of a marketable product. Within the scope of this work, only the applicability of PAS to in the percentage range concentrated short-chain hydrocarbon samples is demonstrated.

Brief descriptions of the following chapters are given below.

In Chapter 2, an introduction to the topic of methane and its main isotopologues and their relevance is given. Furthermore, natural gas is presented with regard to its deposits and the associated production possibilities, its compositions and the applications. In addition, a description of the established methods of measuring the short-chain methane main-isotopologues as well as the main alkanes is given.

Both the main methane isotopologues and the main alkanes show partially strongly overlapping absorption spectra regions. For the spectroscopic differentiation of various gas molecules, it is therefore essential to determine an optimal center laser wavelength, which allows the measurement of complex gas mixtures with respect to their composition. Chapter 3 therefore describes a newly developed mathematical algorithm which determines the optimal center wavelength for spectroscopy on the basis of the theoretical absorption spectra of the individual gas molecules.

In order to obtain accurate and precise measurements of the concentrations of the main methane isotopologues and main alkanes, an exact knowledge of the spectral behavior of the ICL used in the selected injection-current modulation mode is essential for the application of PAS. For this reason, Chapter 4 presents a detailed description of a specially developed Michelson interferometer-based method, which allows the determination of the absolute wavelength in direct injection-current modulation mode of the ICL as a function of the laser operating current.

In Chapter 5 the principle of the photoacoustic effect, which is the basis of PAS, is described in detail. Furthermore, a detailed explanation of the self-developed PAS measurement setup and gas mixer, which was used for the preparation of the calibration gas mixtures, is given. Subsequently, the results obtained with the sensor are presented and discussed in detail. These include measurements of natural gas like methane main-isotopologue mixtures prepared under laboratory conditions.

Chapter 6 presents the advanced PAS measurement setup, which provides DSP-based real-time analysis of gas samples. The calibration of the sensor based on artificially produced natural gas like gas mixtures and subsequently the validation of the sensor based on real natural gas samples is presented. A GC is used as a reference for the measurements.

A summary of the results obtained, as well as an outlook on possible optimizations of the sensor, is presented in Chapter 7.

Chapter 2

Methane and its Main Isotopologues and Natural Gas

As described in Chapter 1, the sensor aims to analyze the natural gas in terms of its methane, ethane and propane composition, as well as detect the main methane isotopologue concentrations. To understand the background of the sensor, the natural gas and the main methane isotopologues are described in more detail in the following sections. Their structures, sources, applications and established analysis techniques will be comprehensively explained.

2.1 Natural Gas

Natural gas is one of the most important energy sources of our time and plays a significant role in the global energy supply. It consists of 75-99% methane, 1-15% ethane and 1-10% propane, as well as other small amounts of longer-chain hydrocarbons such as butane and pentane, but also of small amounts of nitrogen, carbon dioxide and noble gases (Hammer et al., 2003). As a product of long-term geological formation, created by the decomposition of organic materials such as plants and microorganisms over millions of years, the exact composition of natural gas is highly dependent on its origin (Decourt et al., 2014). Table 2.1 shows the strong location dependence of the methane content.

Natural gas is divided into two groups according to its origin: conventional natural gas and unconventional natural gas. Conventional natural gas is the most common type. It is trapped in cavities in the mantle of the earth and can be extracted by simply drilling from the earth's surface. Unconventional natural gas is trapped in shale rock (shale gas), coal seams (coalbed gas) or sandstone or limestone (tight gas) (Faramawy et al., 2016). Since the rocks in which the unconventional gas is trapped are not sufficiently porous and

TABLE 2.1: Natural gas methane share in dependence of its origin (Decourt et al., 2014).

Origin	Country	Methane share
Fayetteville Shale	US	97.3%
Jingbian-Hengshan	China	97.1%
Dovletabad	Turkmenistan	95.2%
Troll Est	Norway	92.8%
Margarita-Huacaya	Bolivia	90.5%
North Dome	Qatar	84.1%
Kangan	Iran	84.1%
Groningen	Netherlands	81.2%
Gorgon	Australia	76.0%
Spleiper	Norway	76.0%
Orenburg	Russia	66.7%
Ghawar	Saudi Arabia	55.6%
Astrakhan	Russia	44.4%
Natuna	Indonesia	26.9%

thus impermeable, fracking technology must be applied. Fracking, the well-known short term for hydraulic fracturing, involves pumping a mixture of water, sand and chemicals under high pressure into the rock, causing cracks to form and releasing the natural gas (Pană et al., 2022).
The crack formation and the subsequent gas release is, to a certain extent, uncontrollable (Meiners et al., 2013). This makes it necessary to identify gas leaks and thus contain potential environmental damage.

When drilling for gas production, gas samples can be taken at various drilling depths that have a composition similar to natural gas. These samples allow geological conclusions regarding the surrounding rock, but also about the expected gas deposit, based on the compositions of the samples (Wiersberg and Erzinger, 2007).
Furthermore, the composition of natural gas is extremely important for its combustion. The proportions of the individual hydrocarbons determine the energy content of the natural gas and thus its calorific value. In a mixture the different components contribute according to their concentrations (Park et al., 2021, Leicher et al., 2017).
Optimal operating parameters of gas-fired devices depend on composition because methane, ethane and propane require different amounts of oxygen for a complete combustion (Demoulin et al., 2008). If the ratio of oxygen

to gas components is not correct, incomplete combustion can occur, reducing energy efficiency and potentially causing harmful emissions. The knowledge of the composition helps to set the right combustion conditions to ensure optimal and environmentally friendly combustion (Wei et al., 2021).
In addition, the composition of natural gas has a significant influence on the monetary value of the natural gas. Both industrial and private customers of natural gas receive bills based on average values of the natural gas composition and thus the energy content. The actual energy content sometimes varies significantly from the values used for billing, which often results in financial disadvantages for the customer. Knowing the actual composition of the natural gas purchased would make it possible to create correct bills regarding the energy content (Paulus and Lemort, 2023). The knowledge of the exact composition of natural gas is of utmost importance in many aspects.

2.1.1 Natural Gas Analysis Techniques

Gas Chromatography (GC)

Gas chromatography (GC) is considered the gold standard of natural gas analysis. The individual natural gas components are separated in a separation column and then quantitatively detected, for example with a flame ionization detector (FID) (Rhoderick, 2003; Brown et al., 2004). The advantage of GC is the high accuracy and the high dynamic range regarding the concentrations. With a gas chromatograph, measurements with deviations of 1-2% are possible in a dynamic range starting in the ppb range up to 100%. The flame of the FID can be problematic in places with a high risk of explosion, for example at drilling sites. Furthermore, a variety of operating gases are required, such as helium as carrier gas, synthetic air and hydrogen as combustion gas for the FID. Additionally, the analysis time can be up to 45 minutes depending on the selected analysis parameters. For reliable operation of the gas chromatograph, specially trained personnel is also required, since the operation of the instrument is complex and even small operating errors can completely falsify the measurement (Poole, 2021).

Spectroscopic Methods

Infrared spectroscopy in various forms was tested. The wavelength range was typically 1,000 - 2,000 nm.

A variety of measuring instruments exist which can detect methane, the main component of natural gas, by means of infrared absorption spectroscopy (Compur Monitors, 2021, Mueller-Elektronik AG, 2023). These devices are very compact and thus allow field measurements with very short measuring times. The disadvantage, however, is that they cannot perform a complete natural gas analysis and thus only provide an indication of natural gas leakage.

Infrared absorption spectroscopy can also be performed from higher altitudes. Unmanned flying objects (drones) and satellites are used for this purpose (Iwaszenko et al., 2021; Pandey et al., 2023). Their emitted laser radiation is reflected at the earth's surface and thus also allows conclusions to be drawn about the presence of methane in the atmosphere. The advantage of these methods is the large measurement area that can be covered. Since the reflectivity depends on the existing topography of the reflecting point and the interaction path is large due to the measurement height, cross-sensitivities causing larger deviations are to be expected with this measurement method.

Fourier transform near-infrared (FTNIR) spectroscopy is a well-known embodiment of infrared spectroscopy (Haghi et al., 2017). Based on a Michelson interferometer, an absorption spectrum is generated in conjunction with the Fourier transform, from which the proportions of the individual components of the gas sample can be determined.

Another method of infrared spectroscopy is transmission spectroscopy based on hollow-core photonic bandgap fibers (Li et al., 2012). The gas mixture to be analyzed flows into the fiber, where the interaction between the laser radiation and the natural gas occurs. By tuning the laser, an absorption spectrum can be recorded by means of an intensity detector. The resulting spectra can also be used to quantify the individual gas components.

The advantage of both methods is the comparatively short measurement time in the range of seconds compared to gas chromatography. Water exhibits strong absorption lines in the spectral range mentioned, so that large cross-sensitivities can occur, which leads to considerable measurement deviations. Furthermore, there is a temperature dependency for both methods, which negatively influences the accuracy. Due to the mechanically sensitive structures, vVibrations also have a significant negative influence on the measurement results. For these reasons, field measurements are hardly possible.

A further spectroscopy method, which enables the detection of almost all natural gas components, is Raman spectroscopy (Dąbrowski et al., 2019; Kiefer

et al., 2008; Petrov et al., 2022). This measurement technique based on the Raman Effect requires laser power in the Watt range, which makes it expensive and eye safety becomes an important issue. Furthermore, a set of calibration measurements are prerequisite to obtain reliable results under a wide range of measurement conditions. One of the most recently published spectroscopic technologies for natural gas analysis is based on proton Nuclear Magnetic Resonance (NMR) spectroscopy (Duchowny et al., 2022). The advantage of this method is the high accuracy of the results, the relative error is less than 1% in relation to the GC reference. Measurements under different temperature and pressure conditions are also possible. Nevertheless, field measurements are hardly possible since a benchtop NMR, such as the Spinsolve 60 ULTRA NMR spectrometer from Magritek (Aachen, Germany), weighs 60 kg and measures 58 x 43 x 40 cm.

When modulated laser radiations hits molecules, which absorb the energy of the photons, complex intermolecular relaxation processes can occur. Subsequently, a thermal wave is generated, which leads to a pressure wave. This phenomenon is well known as the photoacoustic effect which is applied in photoacoustic spectroscopy. The resulting sound wave is typically amplified by means of an acoustic resonator and detected by a microphone (Palzer, 2020).
Photoacoustic spectroscopy is well known as an analytical method for the detection of trace gases in the ppb to ppm range (Sigrist, 1995).
QEPAS (Quartz Enhanced Photoacoustic Spectroscopy) represents a special embodiment of PAS. In this case, the microphone is replaced by a quartz tuning fork, which typically has a Q-factor greater than 10,000 (Sampaolo et al., 2022).
QEPAS has already been successfully used to study the relaxation processes of gas mixtures consisting of methane, ethane and propane, each with fractions in the lower percentage range (Menduni et al., 2022).
First QEPAS measurements involving the simultaneous detection of synthetic natural gas-like mixtures consisting of methane, ethane, and propane under laboratory conditions were presented Luo et al., 2022. The evaluation is based on the signal amplitude at discrete wavelengths. The measurements are so far limited to synthetic mixtures.

2.2 Methane and its Main Isotopologues

2.2.1 Methane

Methane is the natural gas main component and the shortest alkane, which is composed of one carbon atom and 4 hydrogen atoms in a tetrahedral structure. The structural formula is shown in Figure 2.1.

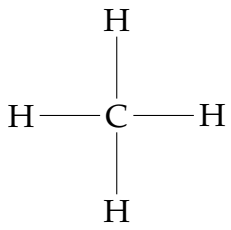

FIGURE 2.1: Methane structural formula.

Methane is stored and emitted from a variety of sources around the world. The 3 largest sources include wetlands, agriculture, and methane emitted from power generation. In total, 570 Mt per year are released into the atmosphere (IEA, 2023). The influence of a chemical compound on global warming, and thus on climate change itself, is described by the Global Warming Potential (GWP). The reference here is the effect of CO_2, whose GWP is accordingly exactly 1. If we consider an impact period of 100 years, the 100-year GWP of methane is determined to be 34 (Jacobson, 2021). This means that 1 ton of emitted methane in our atmosphere has the same impact as 34 tons of emitted CO_2, accumulated over a time period of 100 years. Thus, the effect of each unit of emitted methane is many times more harmful to the climate than CO_2. Figure 2.2 below shows the evolution of methane content in the atmosphere since 1994. The rising course of the graph in Figure 2.2 shows the urgency to curb methane emissions in a targeted systematic way in order to avoid a further continuously rising methane content in our atmosphere. To achieve this goal, it is imperative to identify the sources of methane emission. This is possible by measuring the isotopologue ratio $^{12}CH_4/^{13}CH_4$. In the following subsection the explanation of the two main methane isotopologues is given.

2.2.2 Methane Main Isotopologues

Two main methane isotopologues exist: $^{12}CH_4$ and $^{13}CH_4$. The natural abundance of these two molecules are 98.9% and 1.1%, respectively. The isotopologic composition of methane differs depending on the emission source. A

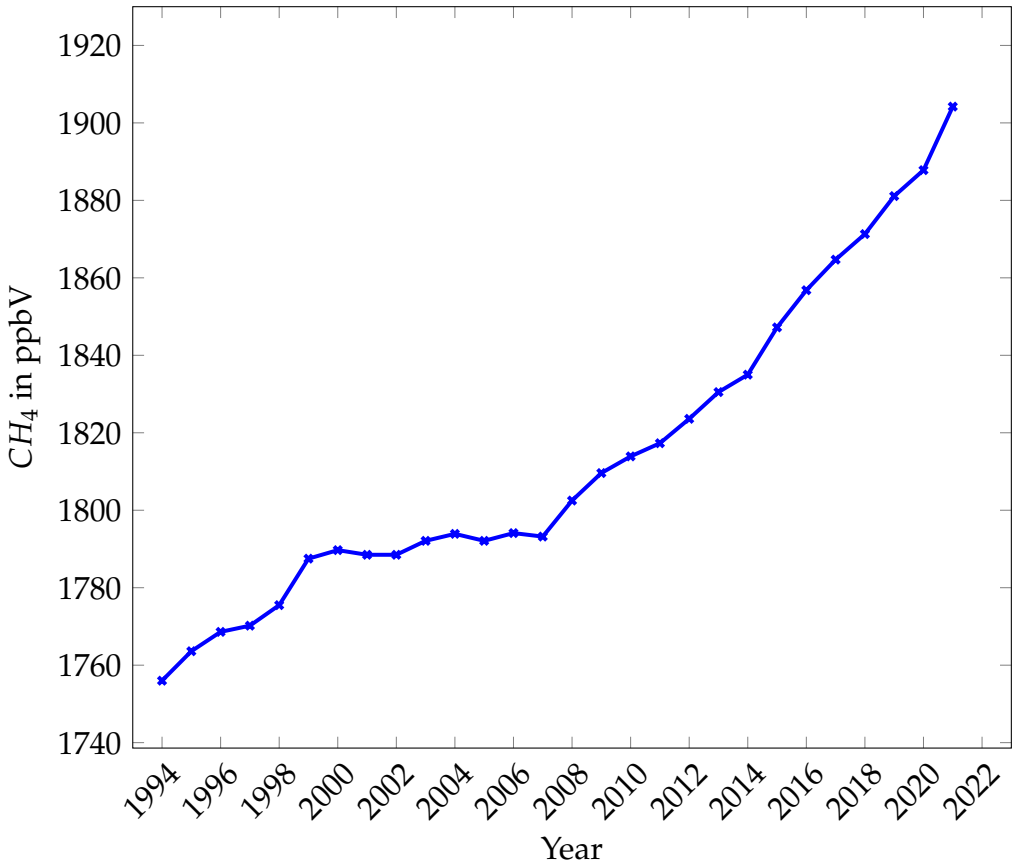

FIGURE 2.2: Methane share world trend of the World Meteorological Organization (WMO), determined as of the first month of each year. (Federal Environmental Agency Germany, 2023).

sensitive and selective detection of the two main isotopologues, $^{12}CH_4$ and $^{13}CH_4$, could allow it to determine whether methane traces originate from biogenic or anthropogenic sources (Schwietzke et al., 2016). The fact that anthropogenic sources tend to a have slightly higher $^{13}CH_4$ content can help identify and contain them and, thus, reduce the associated contribution to climate change (Schroll et al., 2020).

Furthermore, the $^{13}C/^{12}C$ concentration ratio of natural gas allows conclusions to be drawn about the type of gas and its source (Fuex, 1977). Shale gas, for instance, exhibits a specific main alkane composition and $^{13}C/^{12}C$ ratio. It is depleted in its $^{13}CH_4$ share in comparison to other types of natural gas. Due to the fact that the fracking technique implicates increased methane emissions into the atmosphere, its identification is of utmost importance (Howarth, 2019). Furthermore, the isotope ratio can be used to determine the shale porosity and permeability. These parameters, amongst others,

determine the most suitable conveyor technique. The data can also help to optimize the shale stimulation treatment, saving cost and water and thus protecting the environment. Furthermore, the isotope ratio represents an important parameter for the horizontal drilling control (Zhang and Krooss, 2001).

Another application that requires the isotopologic analyses of high methane concentrations can be found in planetary and cometary research. The investigation of the atmospheric composition of planets such as Neptune, Titan and Uranus delivers important information about their formation and evolution (Fletcher et al., 2009; Moses et al., 2020). Astronomic theories, e.g. the core accretion and collapse model (Pollack et al., 1996) which explains the formation scenario of the Solar System, could be confirmed in that way.

The isotopologic "signature" of methane, i.e. the concentration ratio of $^{12}CH_4$ and $^{13}CH_4$, is usually expressed as the deviation from the Pee Dee Belemnite standard in per mill (parts per thousand). This $\delta^{13}CH_4$ value is defined as:

$$\delta^{13}CH_4 = \left(\frac{R_{sample}}{R_{std}} - 1 \right) \cdot 1000‰ \tag{2.1}$$

where R_{sample} is the $^{12}CH_4/^{13}CH_4$ ratio of the sample and $R_{std} = 0.0112372$ (*Reference and intercomparison materials for stable isotopes of light elements. Proceedings of a consultants meeting held in Vienna, 1-3 December 1993*, 1995).

Figure 2.3 shows different $\delta^{13}CH_4$ values in promill for different methane sources. It can be seen that the range is more than 60 promill and that the sources can be clearly distinguished with regard to the $\delta^{13}CH_4$ value.

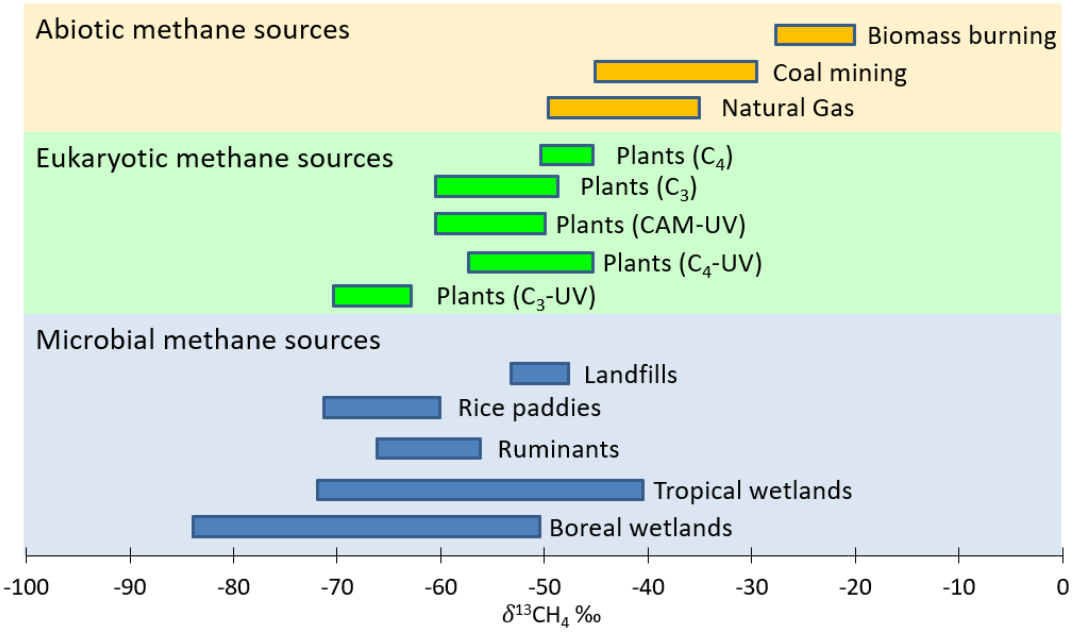

FIGURE 2.3: Isotope-ratio of different carbon sources (Schroll et al., 2020, edited).

The two main isotopologues differ according to their mass number by 1 neutron and are structurally identical according to Figure 2.4.

FIGURE 2.4: Structural formulas of $^{12}CH_4$ (left) and $^{13}CH_4$ (right).

However, they differ minimally in their absorption spectra, as Figure 2.5 shows.

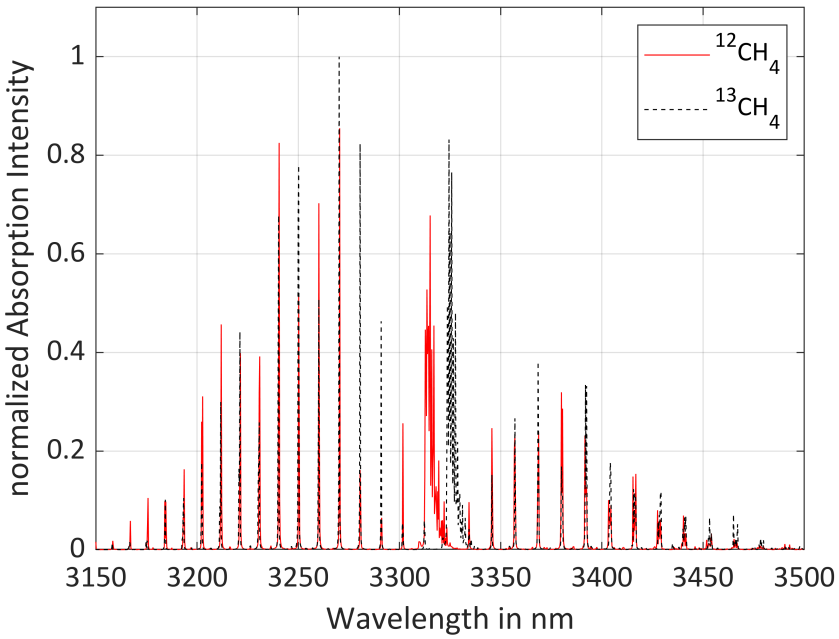

FIGURE 2.5: Fundamental vibrational absorption spectra of $^{12}CH_4$ and $^{13}CH_4$ (Gordon et al., 2022).

2.2.3 Methane Main Isotopologues Analysis Techniques

Due to the identical structure and the hardly differing absorption spectra, the identification of the two molecules is very challenging. In the following, the two established methods for methane main isotopologue analysis will be described.

Gas Chromatography - Isotope Ratio Mass Spectroscopy (GC-IRMS)

A very established and precise method for the analysis of gas mixtures is gas chromatography (GC). This technique allows molecular components to be separated by means of a separation column. The individual molecules are sequentially released from the separation column with a time delay, the so-called retention time, and subsequently detected by a detector, e. g., a flame ionization detector. The resulting chromatogram shows which types of molecules were present in the sample and their respective concentrations (Poole, 2021). However, since different isotopologues of the same molecule do hardly differ in their retention time, an isotope analysis only by GC is not possible. In order to achieve this, GC is combined with mass spectrometry. The so-called isotope-ratio mass spectrometry (IRMS) represents the gold standard for isotope analyses.

The main methane isotopologues separated by the gas chromatograph must first be oxidized to CO_2 in the next step. This step converts the isotopologues into molecules with a mass-to-charge ratio of 44-45. The ionized molecules then pass through an upstream magnetic field, which deflects them onto individual paths depending on their specific mass-to-charge ratios. The isotopologue ratio of the original methane main isotpologues can then be measured by the downstream Faraday detector (Sessions, 2006).
In order to achieve exact and reproducible results with a GC-IRMS system, in addition to special user know-how, daily reference measurements with reference samples are required to compensate for the drift of the system. Due to the complexity of the measurement setup and the high demands on stable ambient conditions, field measurements are hardly possible.

Cavity Ringdown Spectroscopy (CRDS)

Another established method for determining the methane isotopologue composition is cavity ringdown spectroscopy (CRDS). In a resonator, laser radiation is reflected by one or more mirrors, whereby a part of the radiation is transmitted by the mirrors, as they do not reflect perfectly. The transmitted part is detected by a photodetector, the intensity of which depends on the previous absorption in the resonator by the gas molecules present in the natural gas sample. The photodetector detects an exponentially decreasing intensity, whereby its decay is constant in connection with the emitted wavelength provides information about the gas composition. By tuning the wavelength of the laser used, the $\delta^{13}CH_4$ can be determined. Since the measurement principle is primarily based on the absorption of laser radiation, cross-sensitivities due to the absorption of the laser radiation by other gas molecules present are inevitable and lead to erroneous results, even with small concentrations of unknown molecules of the gas matrix. The typical precision of this analysis technique is in the per mill range. Monthly recalibration measurements are required to maintain the specified precision (PICARRO, INC., 2022). Therefore, field measurements are difficult to realize.

Photoacoustic Spectroscopy (PAS)

An alternative to GC-IRMS and CRDS could be photoacoustic spectroscopy (PAS) (Palzer, 2020). PAS is mainly suitable for the detection of trace gases but has been shown to enable the identification and quantification of methane isotopologues in the single-digit per mill range (Giglio et al., 2022) down to

the parts per million (ppm) range (Loh and Wolff, 2019/2019b). The latter corresponds to typical concentrations in the atmosphere (van Amstel, 2012).

In this work, the applicability of PAS is presented for both the main alkane composition analysis and isotopologic analysis of highly concentrated methane samples. The investigation of natural gas like compositions and real natural gas samples were carried out in the methane, ethane and propane concentration range of 7-87%, 4-5% and 0.5-1.0%, respectively. The measurements of $^{12}CH_4/^{13}CH_4$ mixtures are performed in nitrogen with concentrations of 25–70% and 0.28–3.00%, respectively, under laboratory conditions.

Note: Parts of the Introduction were published in *Bahr and Wolff, 2022* and are partially edited.

Chapter 3

Optimal Center Wavelength Determination

Optical spectroscopy is nowadays a well-established method for the analysis of gaseous mixtures. As soon as a high spectral resolution is required, spectrometers usually apply lasers as radiation sources (Demtröder, 2014a, Demtröder, 2014b, Werle et al., 2002). In order to be able to probe different absorption features with a single laser, it is advantageous if its emission wavelength can be varied. Therefore, semiconductor lasers are predestined for this task, because they can be spectrally tuned via their operating temperature and current. The tuning range of distributed feedback interband cascade lasers is, for example, of the order of 10 nm at constant laser temperature with an emission linewidth in the single-digit megahertz range (nanoplus, 2023, Zeller et al., 2010, Vurgaftman et al., 2015, Meyer et al., 2020).

When designing a laser spectrometer, the definition of the laser's emission wavelength or, if tunable, its spectral range is crucial for its potential applications. As a matter of course, all the components of interest should exhibit absorption within the range. Furthermore, it is desirable that the absorption strengths of all components are high in order to achieve high detection sensitivity. Simultaneously, interferences of the absorbing compounds should be excluded to the greatest possible extent in pursuance of avoiding metrological ambiguity and, thus, reach high detection selectivity (Demtröder, 2014a; Demtröder, 2014b).

The identification of the optimal spectral range for a certain application, i.e. for the analysis of a certain mixture of gases, is not trivial. In practice it is usually an educated guess based on the known spectra (Demtröder, 2014b; Dyroff, 2009; Lackner, 2007). The spectra evaluation, i.e. the determination of the concentrations of the individual components, is then typically carried

out using a multivariate calibration such as partial least squares regression. However, the quality of the results, especially the selectivity, strongly depends on the selected wavelength range and the selection becomes increasingly difficult if the single spectra strongly overlap, and even more so if the single components are very similar and their spectra differ only slightly.

The following procedure is customized for lasers of a certain tuning range, such as semiconductor lasers, and delivers its optimal center wavelength. The following section describes the mathematical procedure. After that results regarding the main alkanes and methane main isotopologues are presented.

3.1 Mathematical procedure

For the application of the method, knowledge of the absorption spectra of all gaseous components in the mixture is required. The spectra can be measured beforehand, e.g. with a Fourier Interferometer, or extracted from databases such as HITRAN, 2022; GEISA, 2022; JPL, 2022 or NIST, 2022. The flow chart of the method is shown in Figure 3.1. The individual steps are explained in the following subsections.

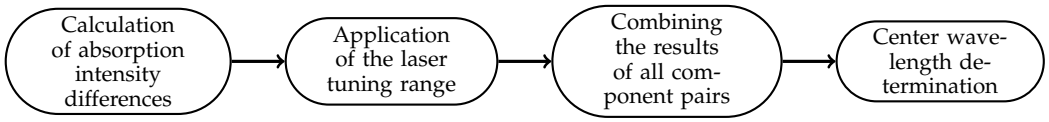

FIGURE 3.1: Flowchart of the mathematical procedure (Bahr et al., 2022, edited).

3.1.1 Calculation of absorption intensity differences

In order to measure the individual gas components selectively or with least interference, it is necessary to identify the wavelengths at which the absorption spectra maximally differ from one another (Tomberg et al., 2018). To find these spectral regions, all spectra are normalized to 1. A total number n of gases (spectra) results in:

$$\binom{n}{2} = \frac{n!}{2 \cdot (n-2)!} \tag{3.1}$$

dyads of spectra (Vialar, 2016). The individual absorption intensities of each gas $S(\lambda)$ are then used to calculate the intensity differences for each pair of gases (i and j) as function of the wavelength λ:

$$\Delta S_{ij}(\lambda) = S_i(\lambda) - S_j(\lambda). \tag{3.2}$$

3.1.2 Application of the laser tuning range

Semiconductor lasers exhibit a limited spectral tuning range. In the case of an interband cascade laser the tuning range $\Delta\lambda$ is typically of the order of 10 nm (nanoplus, 2023, Zeller et al., 2010, Zeller et al., 2010, Vurgaftman et al., 2015, Meyer et al., 2020). This has to be considered for the determination of best suited spectral range. The influence is represented by a sliding integral (Q-function) of the individual differences:

$$Q_{ij}(\lambda) = \int_{\lambda-\frac{\Delta\lambda}{2}}^{\lambda+\frac{\Delta\lambda}{2}} \left|\Delta S_{ij}(\lambda')\right| d\lambda' \tag{3.3}$$

Q_{ij} represents a measure of the spectral deviation of the species i and j in the wavelength range from $\left(\lambda - \frac{\Delta\lambda}{2}\right)$ to $\left(\lambda + \frac{\Delta\lambda}{2}\right)$. Due to the dependence of the integral limits on the wavelength, the integral acts like a window function. This window is sliding over the entire spectral range. Thus, the integral can also be described as a sliding integral.

Differences $\Delta S_{ij}(\lambda)$ of components with weak absorption can lead to inaccurate results in the following steps and, therefore, need to be suppressed. In order to do this, an auxiliary value D_{ij} is defined:

$$D_{ij} = \int_{\lambda_0}^{\lambda_1} \left|\Delta S_{ij}(\lambda)\right| d\lambda. \tag{3.4}$$

Here, λ_1 and λ_0 are the lower and the upper boundary of the wavelength range under evaluation. Subsequently, a parameter $0 < p \ll 1$ has to be determined empirically, which is related to the threshold values of the individual Q-functions:

$$Q_{ij,th} = p \cdot D_{ij}. \tag{3.5}$$

The threshold values are needed to obtain an unambiguous result for the optimal laser wavelength. The parameter p is chosen optimally if Equation (3.9) provides only a single range – the absolute maximum. $Q_{ij,th}$ is applied to

$Q_{ij}(\lambda)$ according to:

$$\widetilde{Q}_{ij}(\lambda) = \begin{cases} Q_{ij}(\lambda), \text{ if } Q_{ij}(\lambda) > Q_{ij,th} \\ 0, \text{ else} \end{cases}. \tag{3.6}$$

In a next step the Q-functions are multiplied by the difference spectra:

$$\Delta S_{ij,Q}(\lambda) = \Delta S_{ij}(\lambda) \cdot \widetilde{Q}_{ij}(\lambda). \tag{3.7}$$

$\Delta S_{ij,Q}(\lambda)$ can be considered to be the difference spectrum for the gas pair i and j filtered by the Q-functions.

3.1.3 Combining the results of all component pairs

The "filtered" difference $\Delta S_{ij,Q}(\lambda)$ is large for wavelength regions, in which the spectra of a certain gas pair differs and, at the same time, absorption is strong. In order to consider the contribution of all possible gas pairs, all filtered differences are multiplied:

$$P(\lambda) = \prod_{i,j=1}^{n} \Delta S_{ij,Q}(\lambda), \text{ where } i < j. \tag{3.8}$$

The product $P(\lambda)$ is large if the previous conditions are satisfied for all gas component dyads. For absorption-weak wavelengths or wavelengths at which the spectra of the species do not differ significantly, the product $P(\lambda)$ is small. Thus, wavelength ranges with large values of $P(\lambda)$ mark the regions preferable for a sensitive and selective measurement. In order to consider the limited tuning range of semiconductor lasers an integral parameter equivalent to Equation (3.3) is introduced:

$$P_{int}(\lambda) = \int_{\lambda-\frac{\Delta\lambda}{2}}^{\lambda+\frac{\Delta\lambda}{2}} \left|P(\lambda')\right| d\lambda'. \tag{3.9}$$

3.1.4 Center wavelength determination

The wavelength region around the maximum of $P_{int}(\lambda)$ indicates the spectral range in which the center wavelength of the semiconductor laser should ideally be located. The median of P_{int} is chosen as center wavelength since it considers all values of P_{int} and is therefore "well-balanced".

In general, the median m of a function $f(x)$ is defined as (Georgii, 2015):

$$\int_{-\infty}^{m} f(x)\,dx = \frac{1}{2}\int_{-\infty}^{+\infty} f(x)\,dx. \tag{3.10}$$

The application of this definition leads to the optimal center wavelength λ_c of the laser:

$$\int_{\lambda_0}^{\lambda_c} P_{int}(\lambda)\,d\lambda = \frac{1}{2}\int_{\lambda_0}^{\lambda_1} P_{int}(\lambda)\,d\lambda. \tag{3.11}$$

With the aid of software like MATLAB, 2022 it is easy to extract λ_c from this equation.

3.2 Exemplary results

The mathematical procedure described above was programmed in MATLAB and applied to assumptive gas mixtures. The absorption spectra of the single components were measured beforehand or extracted from the HITRAN database, respectively (Loh and Wolff, 2017, Loh and Wolff, 2019a, HITRAN, 2022).

The algorithm was tested on combinations of gaseous, i.e. short-chained, hydrocarbons. Their strongest absorption is associated with the fundamental vibrations and occurs in the mid-infrared wavelength region, typically between 3 and 4 μm (Alrefae et al., 2014). The lower and the upper boundary of the wavelength range under evaluation (λ_0 and λ_1) are 3000 nm and 3600 nm, respectively. Since the absorption spectra strongly overlap, it is often not possible to visually identify the optimal spectral range for the analysis.

3.2.1 Mixture of $^{12}CH_4$ and $^{13}CH_4$

In a first test, the a mixture of the two main isotopologues of methane, $^{12}CH_4$ and $^{13}CH_4$. Figure 3.2 shows both absorption spectra normalized to one. The graph of the $^{12}CH_4$ isotopologue does not reach intensity "one" because downsampling had to be performed after normalization so that the described computational operations can be applied to both isotopologues.

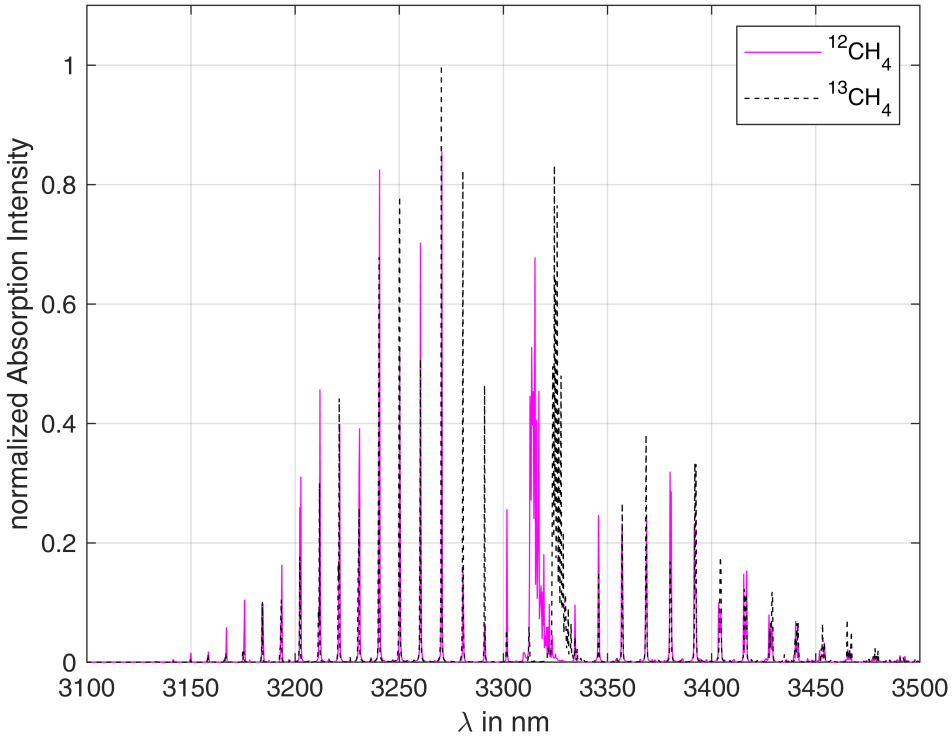

FIGURE 3.2: Absorption spectra of $^{12}CH_4$ and $^{13}CH_4$, based on HITRAN, 2022 (Bahr et al., 2022).

The two gases were selected because the spectral positions of the single rotational lines in the respective P- and R-branch are almost identical, but the positions of the Q-branches clearly differ. The $^{12}CH_4$ Q-branch is approximately located between 3310 and 3320 nm; the $^{13}CH_4$ one between 3320 and 3330 nm. Since the Q-branches additionally exhibit relatively high absorption strength, it would be expected that the laser of a perfectly suited spectrometer (tunability: 10 nm) covers a large part of these regions.
Because this mixture contains only two gases, the measure of the spectral deviation filtered with the Q-function, $\Delta S_{ij,Q}(\lambda)$, equals the product parameter $P(\lambda)$ according to Equation (3.8) which is displayed in Figure 3.3. $P_{int}(\lambda)$, the integral of $P(\lambda)$ over the 10 nm laser tuning range according to Equation (3.9), is shown as well.

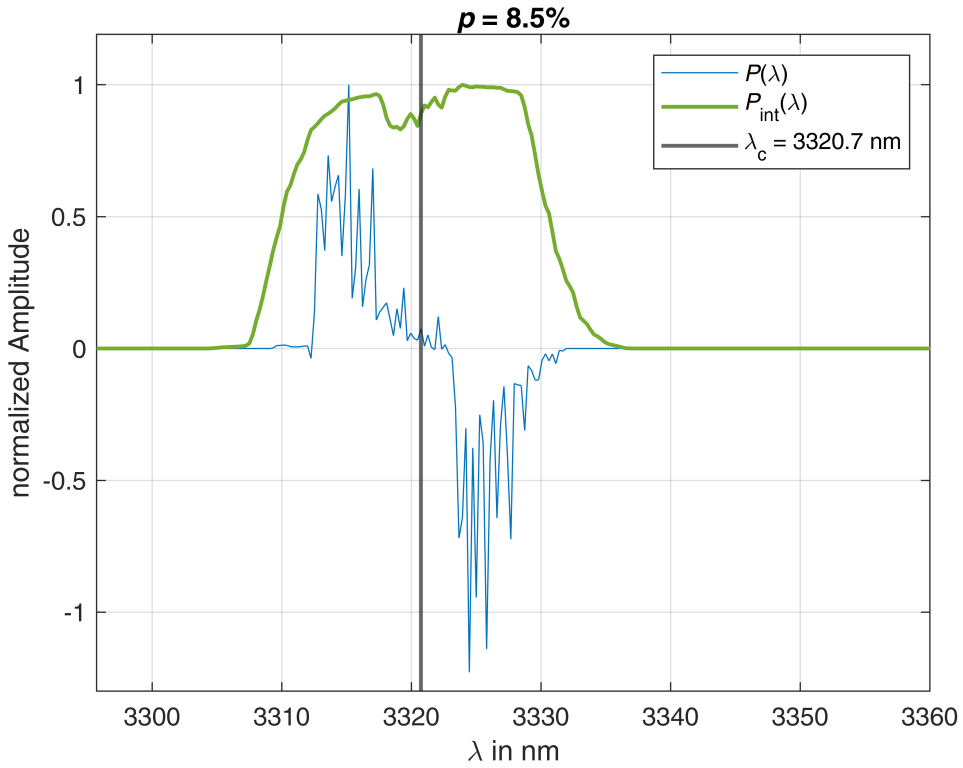

FIGURE 3.3: Evaluation of the mixture $^{12}CH_4$ and $^{13}CH_4$, all quantities are normalized to "one" (Bahr et al., 2022).

Figure 3.3 shows $P_{int}(\lambda)$ for $p = 8.5\%$ on the larger scale whereas the dark grey vertical line represents its median which corresponds to the optimal center wavelength of the laser according to Equation (3.11). The laser exhibits a center wavelength of 3320.7 nm and reaches from 3315.7 to 3325.7 nm. Since this covers a large part of the Q-branches of $^{12}CH_4$ and $^{13}CH_4$ as it would have been expected, the test represents an evidentiary confirmation of the mathematical procedure.

The parameter p according to Equation (3.8) determines the quality of the result to a large extent. Figure 3.4 shows $P_{int}(\lambda)$ around its absolute maxima at 3315 and 3326 nm for values of p between 1 and 9%. The individual curves are shifted by 0.5 relative to each other in vertical direction so that the progress can be clearly seen. With increasing p the secondary maxima between 3200 and 3300 nm and between 3350 and 3450 nm successively disappear whereas the main maximum remains almost unaffected. From 8.5% on only the absolute maximum remains, and for that reason this value was chosen in the previous paragraph.

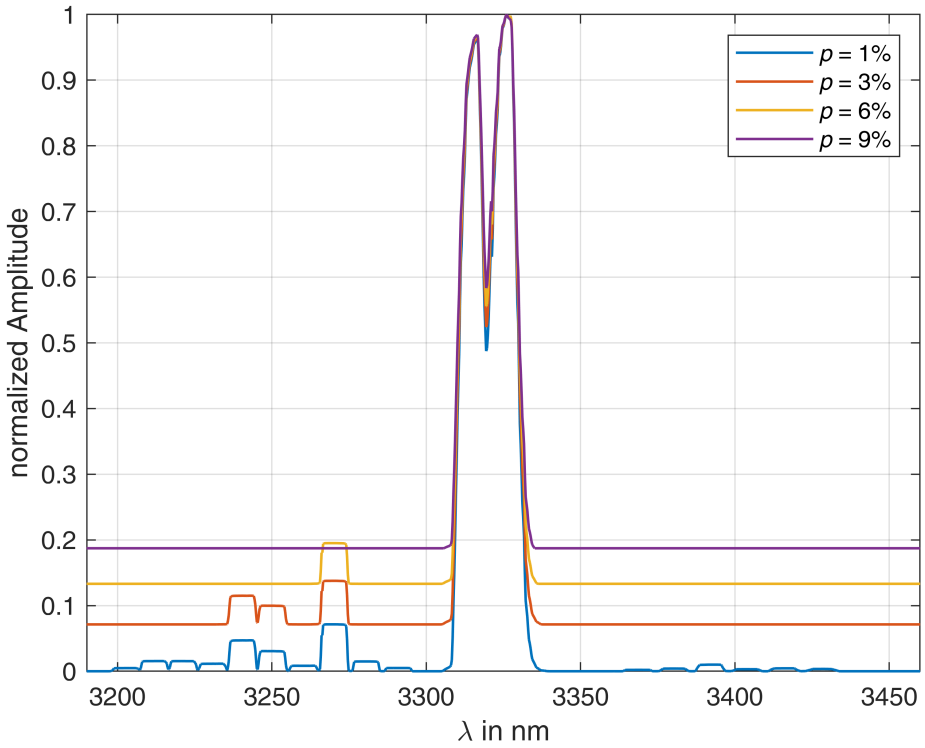

FIGURE 3.4: Normalized of the mixture $^{12}CH_4$ and $^{13}CH_4$ for different values of p. (Bahr et al., 2022).

3.2.2 Mixture of $^{12}CH_4$, $^{12}C_2H_6$ and $^{12}C_2H_4$

The second test of the algorithm was performed on a (simulative) mixture of methane, ethane and ethylene (all carbon atoms with the mass number 12). Figure 3.5 displays the three absorption spectra normalized to one. This combination was chosen, because it is apparently not possible to visually identify the most suited wavelength range for a spectroscopic analysis with a single laser (tunability 10 nm).
Figure 3.6 displays the evaluation results. Its shows:

- The $\Delta S_{ij,Q}(\lambda)$ according to Equation (3.7) for the three possible gas dyads $^{12}CH_4$ - $^{12}C_2H_6$, $^{12}CH_4$ - $^{12}C_2H_4$, $^{12}C_2H_6$ - $^{12}C_2H_4$.
- $P(\lambda)$ (the product of all filtered differences according to Equation (3.8)) and
- $P_{int}(\lambda)$ (the integral of $P(\lambda)$ over the 10 nm laser tuning range according to Equation (3.9)).

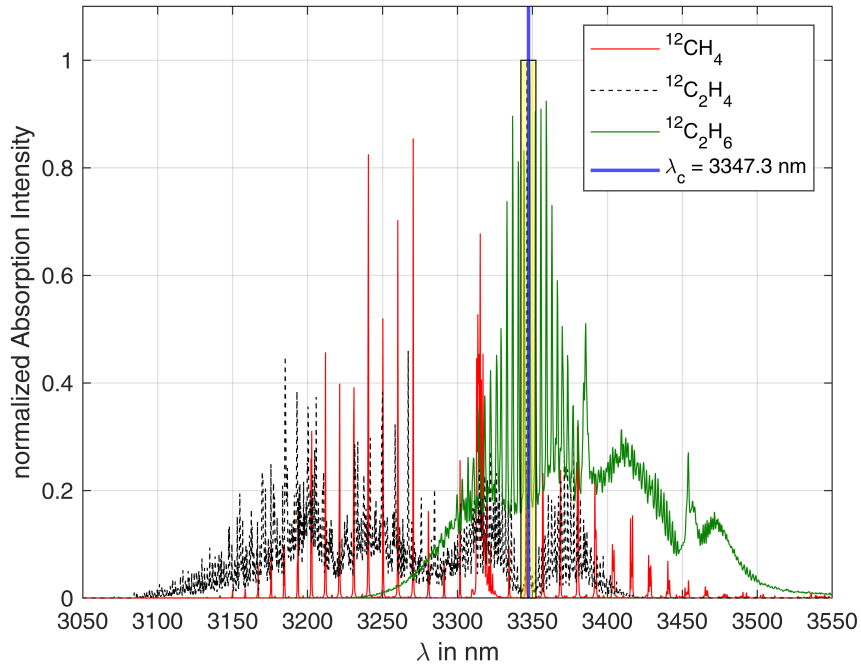

FIGURE 3.5: Absorption spectra of $^{12}CH_4$, $^{12}C_2H_6$ and $^{12}C_2H_4$, based on Loh and Wolff, 2017, Loh and Wolff, 2019a, HITRAN, 2022 (Bahr et al., 2022).

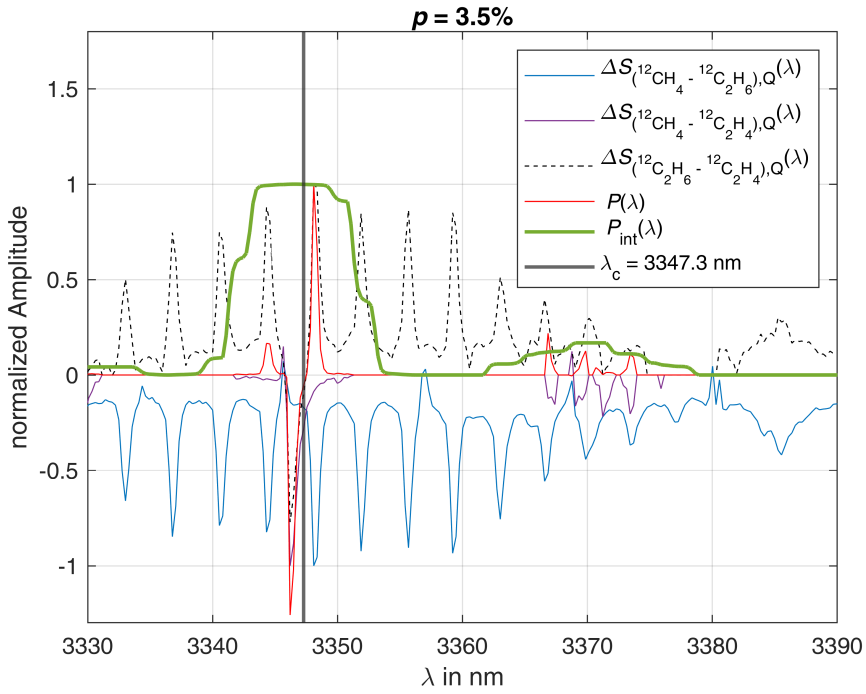

FIGURE 3.6: Evaluation of the mixture $^{12}CH_4$, $^{12}C_2H_6$ and $^{12}C_2H_4$, all quantities are normalized to "one" (Bahr et al., 2022).

The resulting optimal center wavelength of the laser according to Equation (3.11) equals 3347.3 nm. It is marked in Figure 3.6 with a dark grey vertical line. The laser allows spectral tuning from 3342.3 to 3352.3 nm. It covers the characteristically high $^{12}C_2H_4$ line at ca. 3346 nm as well as the two strongest rotational lines of $^{12}C_2H_6$ and one relatively strong and discrete line of $^{12}CH_4$. The range is marked in Figure 3.5 (yellow box). The result of this evaluation is very plausible and represents another confirmation for the applicability of the mathematical procedure.

3.3 Conclusion

The method is particularly suitable for spectrometers based on tunable diode lasers. A prerequisite for its application is that absorption spectra of all gases in the mixture are known. The mathematical procedure identifies wavelength regions, in which the spectra of the single gases significantly differ and, at the same time, the absorption is strong. The definition of a threshold ensures that the best suited spectral region is found. The median of the optimal spectral range is selected as the laser's center wavelength.

The procedure was tried on two simulative gas mixtures. A first test was carried out on a mixture that allowed it to identify the perfect region through educated guessing. That the algorithm yielded the expected region is a convincing confirmation of the method. The second test of the algorithm was performed on a mixture where it was obviously not possible to visually identify the most suited wavelength range. The result of this evaluation is very plausible and represents another confirmation for the method. Finally, it should be mentioned that the applicability depends primarily on the available spectra and that the number of components in the mixture is theoretically limited only by the available computing power. In practice, a spectrometer based on a single diode laser will probably never be applied to mixtures of more than 10 gases.
A limitation of the practical applicability is the fact that the algorithm is based on perfect spectra. Noise and other aspects of metrological reality are not taken into account. Only under these conditions are the results independent of the concentration of the individual components and their ratios.

Note: Parts of this Chapter 3 were published in *Bahr et al., 2022* and are partially edited.

Chapter 4

Interferometric Technique for the Spectral Characterization of ICLs

The exact knowledge of the emission wavelength is one of the fundamental parameters in laser spectroscopy. Several spectroscopic techniques such as photoacoustics require a modulation of the radiation as a matter of principle (Besson et al., 2004).
Semiconductor lasers can easily be modulated by variation of the operating current. In doing so amplitude as well as wavelength modulation are possible. However, assuming a simple, frequency-independent proportionality between wavelength and current, as it is observable in continuous wave (cw) operation, can lead to significant measurement errors (Demtröder, 2014a). The determination of the momentary wavelength becomes extraordinarily difficult if the semiconductor laser emitting in the mid-infrared (e.g., an interband cascade laser or ICL) is modulated with a higher frequency.
At present, different methods and measuring devices exist that enable the spectral characterization of semiconductor lasers such as ICLs (Meyer et al., 2020). However, all of them are primarily applicable for cw radiation. Often, prism or grating spectrometers are used as measuring instruments, which are based on diffraction and interference phenomena, respectively. A further method is the Fourier transform interferometer (FTIR), which is based on a Michelson interferometer and determines the emission spectrum by Fourier transform of the interferogram (Smith, 2011).
Another possibility is the "wavemeter" of BRISTOL Instruments, Inc. (Victor, New York, NY, USA). It measures the wavelength of a laser on the basis of a Michelson interferometer, provides accuracy in the ppm range and represents the state of the art for wavelength measurements in continuous wave operation (Bristol, 2020, Bristol, 2023, Veracious Statistics Research, 2021).
If the laser is operated in current-modulation mode, there are only few possibilities. One approach determines the wavelength change as a function of

the laser operating current ($d\lambda/dI$) (Du et al., 2016). The experimental setup is based on a Mach-Zehnder interferometer and the change in wavelength is calculated using a mathematical algorithm which is not further described. This method does not allow a determination of the absolute wavelength as a function of the current. Another possibility for a fast wavelength measurement is a heterodyne (or super-heterodyne) Michelson interferometer. It differs from the homodyne interferometer in that a beat signal is analyzed that results from the superposition of the radiation to be analyzed and that of a second laser. This technique is particularly well suited if the phase of the beat signal is required (Schuldt et al., 2017, Yoon et al., 2009, Dändliker et al., 1988).

A US patent from 2019 represents the latest research progress regarding the determination of the absolute wavelength of current-modulated semiconductor lasers. It is pointed out that, on the basis of an interferometer, the absolute wavelength of tunable lasers can be determined very precisely. The rudimentarily described method mentions the need for a reference wavelength, e.g., a gas absorption line (R. Seeley, 2019).

To the best of our knowledge there is only one commercially available device for the determination of mid-infrared wavelengths in modulation mode. The "NLIR 2.0–5.0 µm spectrometer" of NLIR ApS (Farum, Denmark) is based on non-linear optics and transforms the laser radiation into the near-infrared range, which is subsequent analyzed using a diffraction grating and a CMOS sensor (NLIR, 2022). According to the manufacturer the maximum sampling rate of the instrument is 130 kHz. The spectral resolution of the NLIR is around 1.5 nm.

Due to the fact that the currently available methods for the spectral characterization of current-modulated semiconductor lasers, especially DFB interband cascade lasers, are not sufficient to achieve a high spectral resolution, new techniques are required.

4.1 Materials and Methods

In the following, two methods for determining the absolute wavelength of modulated semiconductor lasers, in this case interband cascade lasers, are described. Both are based on the same experimental setup and exhibit advantages and disadvantages due to the different signal processing.

4.1.1 Experimental Setup

Figure 4.1 shows the schematic experimental setup for measuring the laser wavelength as function of the current during modulation. It is based on a homodyne Michelson interferometer with silver mirrors and a CaF_2 beam splitter (Steel, 1983). The difference between the two distances a and b is of great importance, because it determines the quality of the results. If a and b approach each other, the number of maxima and minima in the interference signal decreases, which is disadvantageous for the spectral characterization. Simultaneously, the signal-to-noise ratio (SNR) increases due to the decreasing distance to the detector. This has a positive effect on the evaluation. If one of the two paths becomes significantly larger than the other, the number of maxima and minima increases, however, the SNR decreases due to the longer distance to the detector. In order to achieve a good compromise between spectral resolution and SNR, the distances have to be empirically optimized.

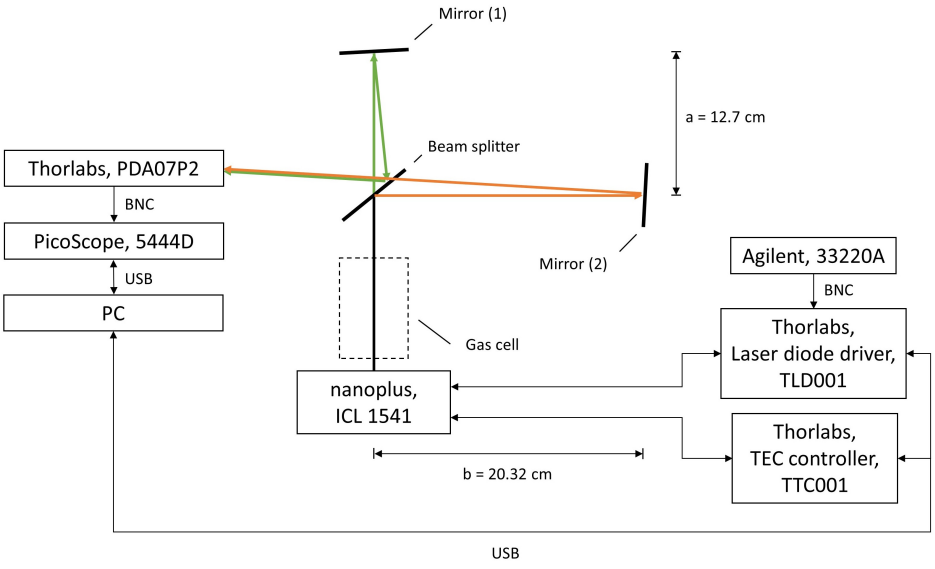

FIGURE 4.1: Experimental setup based on a Michelson interferometer (Bahr and Wolff, 2021).

The Thorlabs PDA07P2 employs an InAsSb detector and provides a bandwidth of 9 MHz. The ICL 1541, manufactured by nanoplus GmbH (Gerbrunn, Germany), was characterized with an average wavelength λ_0 of 3333 nm and a spectral linewidth of less than 20 MHz. The laser can be operated at temperatures between 15 and 27 degrees Celsius. Stimulated emission occurs with operating currents between 25 and 45 mA. The average optical output power is 5.5 mW. During cw operation it can be assumed that the wavelength

is proportional to the current with $d\lambda/dI$ = 0.16 nm/mA. The ICL is driven by the Thorlabs TLD001 diode driver and its temperature is controlled by the Thorlabs temperature controller TTC001. The laser diode current can be accurately set to 10 µA with a noise level < 3 µA rms. The ICL chip is installed in a TO66 housing including a Peltier element for temperature regulation and the temperature sensor. Within the scope of the technical possibilities, the laser wavelength is optimally stabilized. A 33220A function generator (Agilent, Santa Clara, CA, USA) is used to modulate the operating current of the diode driver.
The intensity detected by the detector is converted into a voltage signal which is sampled by a PicoScope 5444D (Pico Technology, Cambridgeshire, UK) with 16 bit resolution. The sampling rate is 62.5 MS/s. The sampled signal is then subjected to processing by means of MATLAB. After the signal is time sliced, Savitzky-Golay based filtering of the signal is performed to eliminate high frequency noise (Press and Teukolsky, 1990). This optimizes the precision of the subsequent detection of the local maxima and minima in the interference signal. Subsequently, different mathematical equations and methods are applied according to the procedures described in Section 2.2 and Section 2.3, respectively.

4.1.2 Non-Linear Regression

Spectral Characterization

The electric field (E-field) component of the ICL radiation at the location of the detector can be described as (Peatross and Ware, 2015):

$$E(t) = \hat{E}(t) \cdot e^{j(\omega t + \varphi_0)} \tag{4.1}$$

where ω is the instantaneous angular frequency of the E-field and φ_0 is the initial phase of the laser radiation. The stochastic phase noise of the laser radiation is neglected here, since it would only increase the complexity of the equation and does not add any value to the following calculations. $\hat{E}(t)$ corresponds to the amplitude and is time-dependent because the ICL is modulated.
One part of the laser beam is transmitted through the beam splitter and reflected by mirror (1). When it hits the detector, its E-Field equals:

$$E_1(t) = \hat{E}(t) \cdot e^{j(\omega t + \varphi_0)}. \tag{4.2}$$

The second part of the laser beam is reflected at the beam splitter, then reflected at mirror (2) and subsequently transmitted through the beam splitter. Due to the path difference $s_d = 2(b-a)$, it hits the detector delayed by a time t_d compared to $E_1(t)$:

$$t_d = \frac{2 \cdot (b-a)}{c} = \frac{s_d}{c}, \tag{4.3}$$

where c corresponds to the speed of light. If this part of the laser beam hits the detector, the E-field component can be described with:

$$E_2(t) = E_1(t-t_d) = \hat{E}(t-t_d) \cdot e^{\omega(t-t_d)+\varphi_0}. \tag{4.4}$$

If the laser current is modulated, the wavelength (angular frequency ω) changes continuously as a function of time. This results in the following relationships for the E-field components hitting the detector:

$$E_1(t) = \hat{E}(t) \cdot e^{j\left(\int_0^t \omega(\tau)\, d\tau + \varphi_0\right)}, \tag{4.5}$$

$$E_2(t) = \hat{E}(t-t_d) \cdot e^{j\left(\int_0^{t-t_d} \omega(\tau)\, d\tau + \varphi_0\right)}. \tag{4.6}$$

The integration of the angular frequency becomes necessary because it is not constant over time anymore.

If both partial beams hit the detector, the sum of both components equals:

$$E_s(t) = E_1(t) + E_2(t). \tag{4.7}$$

Since the detector only detects intensities, the relationship between the E-field components and the intensity must be applied (Kull, 2010):

$$I(t) \propto |E_s(t)|^2. \tag{4.8}$$

Since the absolute value of the intensity is of no importance for the further considerations, the following results for the detector signal:

$$I(t) \propto \hat{E}^2(t) + \hat{E}^2(t-t_d) + 2\hat{E}(t) \cdot \hat{E}(t-t_d) \cdot \cos\left(\int_{t-t_d}^{t} \omega(\tau)\, d\tau\right) \tag{4.9}$$

Due to the extremely short interferometer delay time ($t_d < 1\,ns$), it can be assumed that $E(t) \approx E(t - t_d)$, which simplifies Equation (4.9) to:

$$I(t) \propto 2\hat{E}^2(t) + 2\hat{E}^2(t) \cdot \cos\left(\int_{t-t_d}^{t} \omega(\tau)\, d\tau\right) \tag{4.10}$$

Therefore, the detector signal depends particularly on the interferometer delay time and corresponds theoretically to an oscillation between $4\hat{E}^2(t)$ and zero. The instantaneous angular frequency of the laser $\omega(t)$ can be derived from the phase $\varphi(t)$ of the detector signal. This is possible due to the elementary relationship between the angular frequency and the phase $\omega(t) = \frac{d\varphi(t)}{dt}$ (Giancoli, 2023):

$$\omega_{If}(t) = \dot{\varphi}(t) = \frac{d}{dt}\left(\int_{t-t_d}^{t} \omega(\tau)\, d\tau\right), \tag{4.11}$$

where $\omega_{If}(t)$ corresponds to the angular frequency of the interferometer signal. Since the integration interval in Equation (4.11) corresponds to the delay time t_d, the infinitesimal value $\omega(\tau)$ can be considered approximately constant in the interval. Thus Equation (4.11) results in:

$$\omega_{If}(t) = \frac{d}{dt}\omega(t) \cdot t_d = 2\pi \cdot c \cdot t_d \cdot \frac{d}{dt}\frac{1}{\lambda(t)} = -\frac{2\pi \cdot c \cdot t_d}{\lambda^2(t)} \cdot \frac{d\lambda(t)}{dt}. \tag{4.12}$$

The square of the wavelength $\lambda^2(t)$ can be approximated by the square of the average wavelength λ_0^2 given in the data sheet of the respective semiconductor laser. Understandably, this does not apply to $\lambda(t)$ in the derivative. Resolved according to the wavelength change as function of time and with the relationship $s_d = c \cdot t_d$ according to Equation (4.3), it follows that:

$$\frac{d\lambda(t)}{dt} = -\frac{f_{If}(t) \cdot \lambda_0^2}{c \cdot t_d} = -\frac{f_{If}(t) \cdot \lambda_0^2}{s_d}, \tag{4.13}$$

with the momentary frequency of the interference $f_{If}(t)$. The negative sign on the right side has no meaning for further calculations. Due to the symmetry of the cosine function, it is not possible to distinguish between positive and negative phases of the interferometer signal. The negative sign can therefore be omitted.

However, the wavelength change as function of the change in current is sought. The modulation of the current is, in this case, sawtooth-shaped with

the rate of change k (units: $\frac{mA}{s}$):

$$\frac{dI(t)}{dt} = k \tag{4.14}$$

Equation (4.14) solved for dt and inserted into Equation (4.13) delivers (if the sign is omitted):

$$\frac{d\lambda(I)}{dI} = \frac{f_{If}(I) \cdot \lambda_0^2}{s_d \cdot k}. \tag{4.15}$$

The wavelength as a function of the operating current can be determined from the differential quotient by means of integration if an absolute wavelength is known as reference point:

$$\lambda(I_1) = \int_{I_0}^{I_1} \frac{d\lambda(I)}{dI}\, dI + \lambda(I_0). \tag{4.16}$$

The reference wavelength $\lambda(I_0)$ can, for instance, be determined experimentally. If the modulated laser beam passes a cell filled with a gas that shows a strong and distinct absorption line in the expected wavelength range, the transmission of the interference signal provides the reference wavelength (Stewart, 2021).

Error Estimation

The wavelength as function of current calculated according to Equation (4.16) is subject to deviations due to measurement errors and approximations.

Equation (4.15) inserted into Equation (4.16) results in:

$$\lambda(I_1) = \frac{\lambda_0^2}{s_d \cdot k} \int_{I_0}^{I_1} f(I)\, dI + \lambda(I_0). \tag{4.17}$$

The coefficients of the regression function $f(I)$ can be determined applying a polynomial regression of second (or larger) degree using the evaluated frequency values of the interference signal. After integration, a closed analytical expression is obtained, depending on metrologically determined quantities, which are subject to error tolerances. The maximum possible error can then

be calculated by the sum of the following components:

$$\Delta\lambda(I_1)_{\lambda_0} = \frac{2\lambda_0}{s_d \cdot k}\left(\frac{a_1}{3}I_1^3 + \frac{a_2}{2}\cdot I_1^2 + a_3 I_1 - \frac{a_1}{3}I_0^3 - \frac{a_2}{2}\cdot I_0^2 - a_3 I_0\right)\cdot \Delta\lambda_0, \tag{4.18}$$

$$\Delta\lambda(I_1)_{s_d} = \frac{\lambda_0^2}{s_d^2 \cdot k}\left(\frac{a_1}{3}I_1^3 + \frac{a_2}{2}\cdot I_1^2 + a_3 I_1 - \frac{a_1}{3}I_0^3 - \frac{a_2}{2}\cdot I_0^2 - a_3 I_0\right)\cdot \Delta s_d \text{ and} \tag{4.19}$$

$$\Delta\lambda(I_1)_{\lambda(I_0)} = \Delta\lambda(I_0), \tag{4.20}$$

where $a_{1\ldots3}$ stand for the coefficients of the regression function and $\Delta\lambda_0$, Δs_d and $\Delta\lambda(I_0)$ for the absolute errors of the individual variables. The influence of the integration according to Equation (4.17) on the maximum error can be estimated by the Riemann sum (McGregor et al., 2011) .It includes the standard deviation of the instantaneous frequency $f(I)$, which results from the non-linear regression.

An additional error is caused by approximations. One of the effects is the standard deviation σ_{If} of the interference signal which describes the distribution of the instantaneous frequencies around the regression function. For its share of the maximum wavelength error $\Delta\lambda_{\sigma_{If}}$ applies:

$$\Delta\lambda_{\sigma_{If}} = \frac{\lambda_0^2}{s_d \cdot k}\cdot \pm\sigma_{If}\cdot(I_1 - I_0). \tag{4.21}$$

The result must be added to that from Equations (4.18) to (4.20).

4.1.3 Direct Evaluation of Fringes

Spectral Characterization

The equations presented in Section 4.1.2 are also valid for the method labeled "direct evaluation of fringes". The cosine occurring in the interference signal, according to Equation (4.10), corresponds to local maxima and minima, hereafter referred to as fringes, due to constructive and destructive interference. The conditions for constructive and destructive interference depend mainly on the path difference of the Michelson interferometer whereas:

$$s_d = n \cdot \lambda, \tag{4.22}$$

$$s_d = (2n+1)\cdot\frac{\lambda}{2}, \tag{4.23}$$

respectively, with $n \in \mathbb{Z}$ (Brodie and Booth, 2010). By means of a reference wavelength based on an absorption line in the transmission spectrum, the absolute wavelengths of the individual fringes according to Equations (4.22) and (4.23) can be calculated: After n of the local extremum nearest to the reference wavelength has been determined, all other extrema can be assigned by iterating n. Subsequently, the wavelengths in between the individual extreme points are calculated by non-linear regression.

Error Estimation

The accuracy of the results of this method depends, besides the exactness of the reference wavelength, mainly on the accuracy of the path difference s_d. Its influence on the maximum error of the frequency of fringes f_f results in:

$$\Delta f_f = n \cdot \frac{c}{s_d^2} \cdot \Delta s_d, \tag{4.24}$$

$$\Delta f_f = \frac{2n+1}{2} \cdot \frac{c}{s_d^2} \cdot \Delta s_d, \tag{4.25}$$

for constructive and destructive interference, respectively, where Δs_d corresponds to the maximum error of s_d and the natural number n to the number of fringes which lie to the left or right of the reference wavelength. Due to the linear relationship between Δf_f and n, it is advantageous to base the calculation on the frequency and convert it subsequently to wavelength.

4.2 Results

The two methods were tested using the nanoplus ICL 1541. For the test a sawtooth modulation between 25 and 45 mA was applied. Measurements were conducted at 15, 21 and 27 °C in order to cover the entire dynamic range. The gas used for the determination of the reference wavelength is ethane with a purity of 99.999% and 99% nitrogen content. Measurements were taken at a gas temperature of approximately 22 °C and a pressure of 1000 mbar.

Figures 4.2 to 4.6 show exemplary results obtained by the two methods.

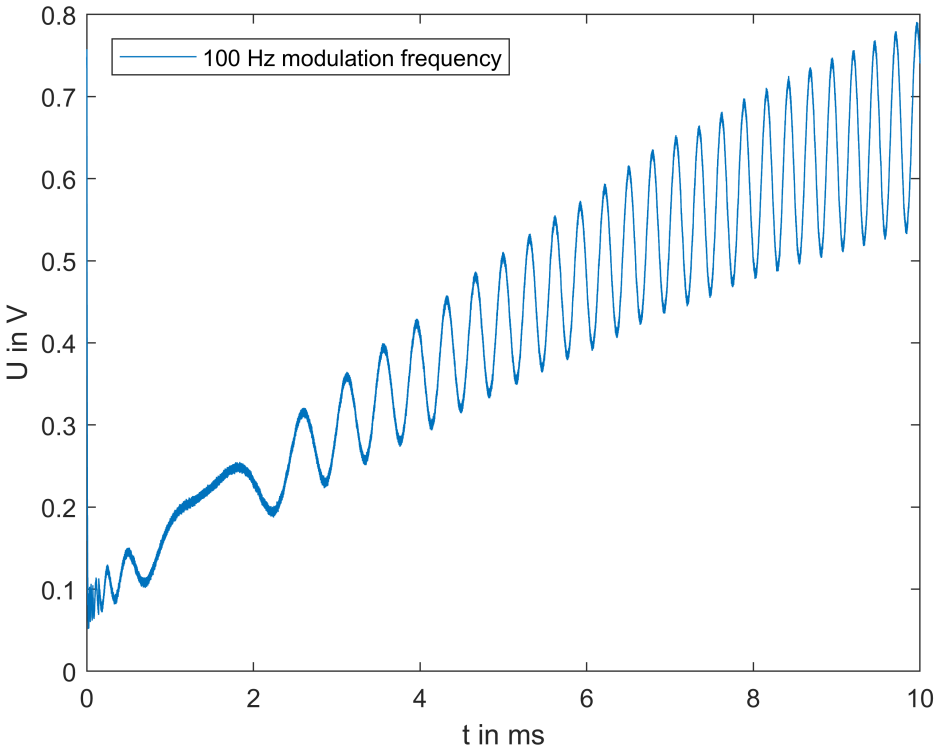

FIGURE 4.2: Exemplary interference signal at 100 Hz modulation frequency and 15 °C laser temperature (Bahr and Wolff, 2021).

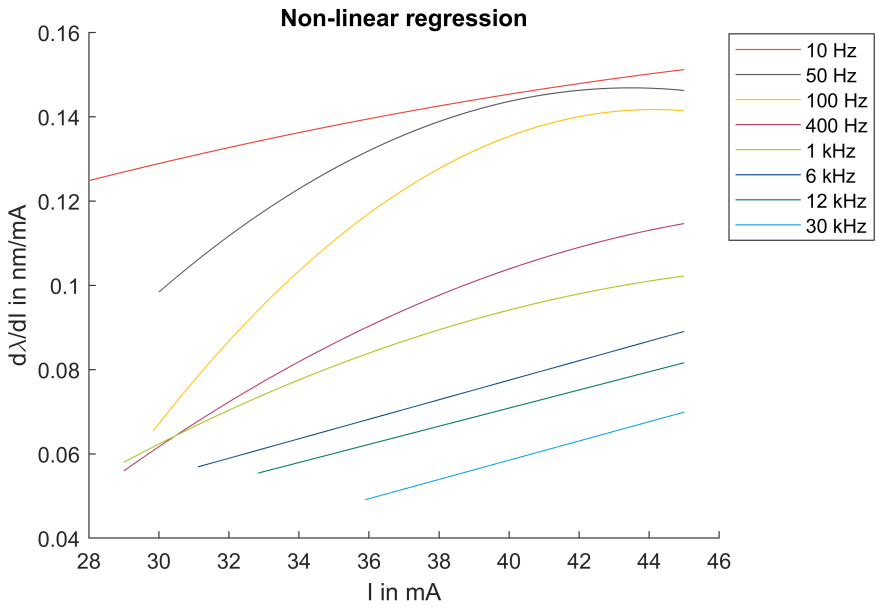

FIGURE 4.3: Change of wavelength as function of operating current for different modulation frequencies based on the non-linear regression method at 15 °C laser temperature (Bahr and Wolff, 2021).

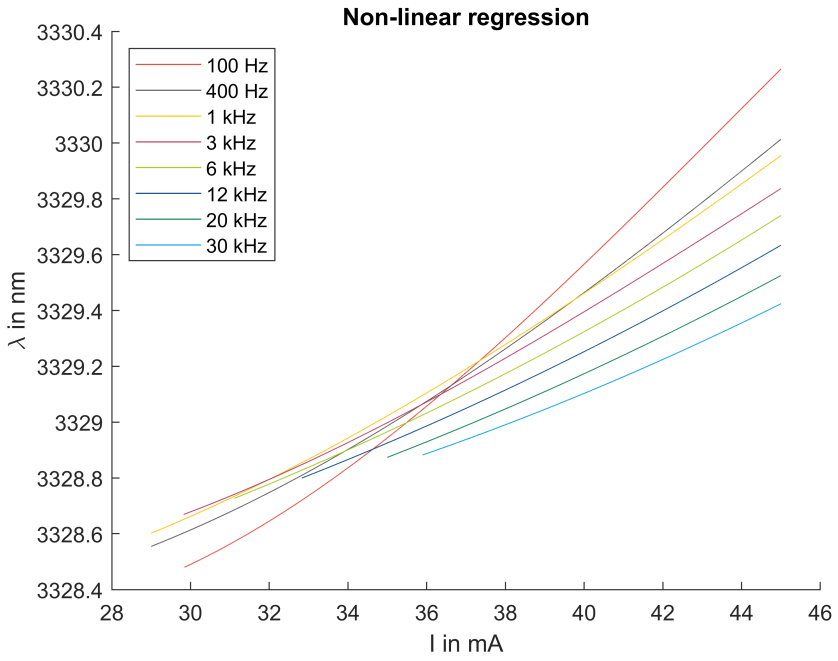

FIGURE 4.4: Absolute wavelength as function of operating current for different modulation frequencies based on the non-linear regression method at 15 °C laser temperature (Bahr and Wolff, 2021).

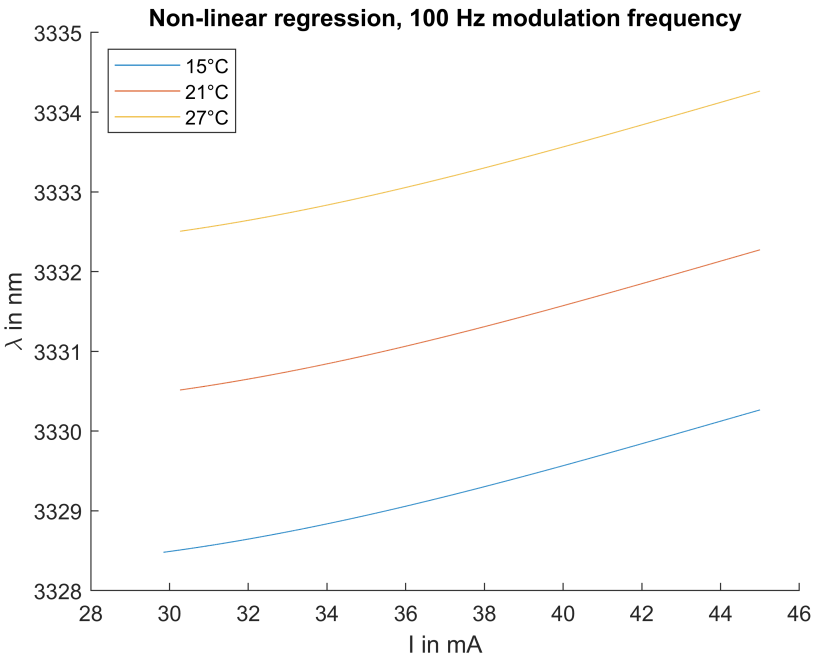

FIGURE 4.5: Absolute wavelength as function of the operating current for three different laser temperatures based on the non-linear regression method at 100 Hz modulation frequency (Bahr and Wolff, 2021).

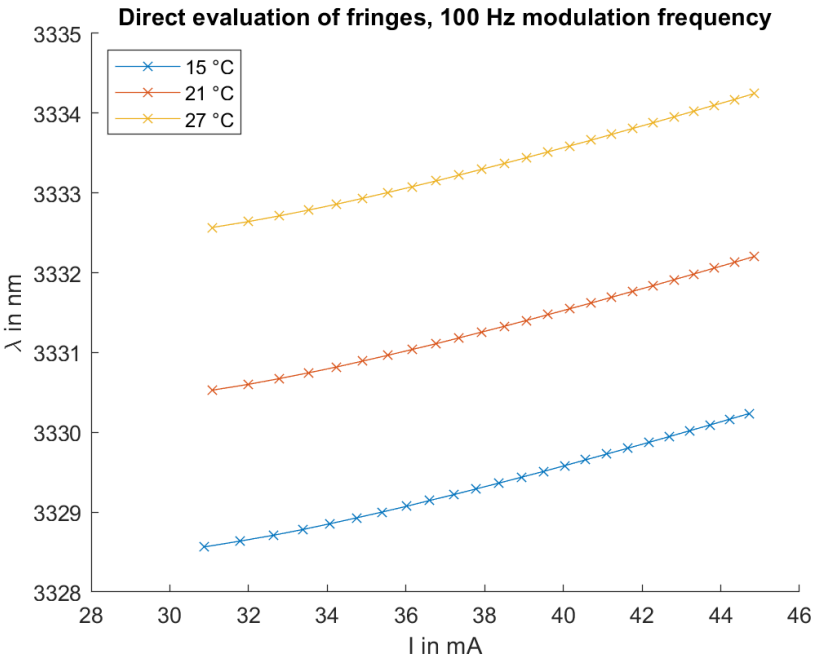

FIGURE 4.6: Absolute wavelength as function of the operating current for three different laser temperatures based on the direct evaluation of fringes at 100 Hz modulation frequency; the crosses mark the calculation points. (Bahr and Wolff, 2021).

The measuring ranges of the two methods differ, because discontinuities in the interference signal are bridged in the non-linear regression method. They can be extracted directly from Figures 4.5 and 4.6, respectively. Table 4.1 lists the measuring ranges as well as the wavelength errors according to Equation (4.18) - Equation (4.21).

TABLE 4.1: Natural gas methane share in dependence of its origin (Bahr and Wolff, 2021).

Method	Measuring Range	Wavelength Error
Non-linear Regression method	30-45 mA	$\Delta\lambda = \pm 0.12\,\text{nm}$
Direct evaluation of fringes	31–45 mA	$\Delta\lambda = \pm 0.030\,\text{nm}$

Table 4.2 presents the spectral range of the ICL as function of the modulation frequency.

TABLE 4.2: Spectral range of nanoplus ICL 1541 (Bahr and Wolff, 2021).

Modulation Frequency (kHz)	Wavelength Range (nm)	$\Delta\lambda$ (nm)	$\Delta\lambda$ (Relative to cw)
cw	3327.52–3330.57	3.05	1.00
0.1	3328.48–3330.27	1.79	0.59
0.4	3328.55–3330.01	1.46	0.48
1	3328.60–3329.95	1.35	0.44
3	3328.67–3329.84	1.17	0.38
6	3328.73–3329.74	1.01	0.33
12	3328.80–3329.63	0.83	0.27
20	3328.87–3329.53	0.66	0.22
30	3328.88–3329.42	0.54	0.18

Figure 4.7 shows the spectral dynamic range $\Delta\lambda$ (relative to cw) as a function of frequency on the basis of the values in Table 4.2. According to the shape of the graph in Figure 4.7, it is reasonable to assume that the relationship shown corresponds to the natural logarithm.

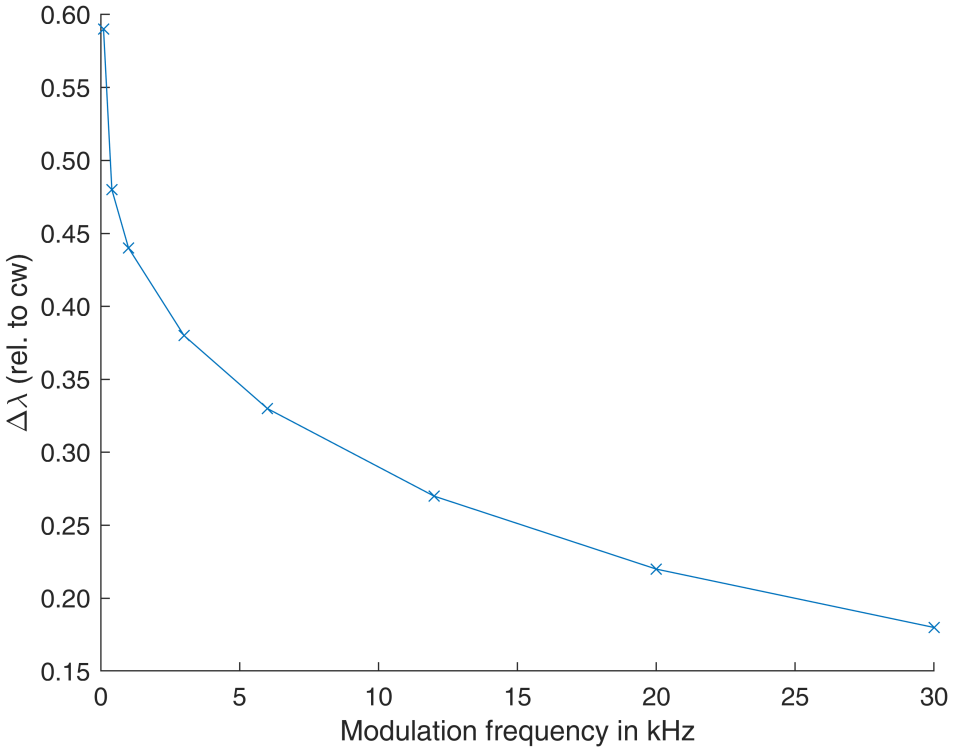

FIGURE 4.7: Spectral dynamic range $\Delta\lambda$ (relative to cw) as function of modulation frequency. (Bahr and Wolff, 2021).

4.3 Discussion

4.3.1 Advantages and Disadvantages of Both Methods

A direct comparison of the methods in Section 4.1 shows that the direct evaluation of fringes requires fewer physical quantities for the calculation of the absolute wavelength and less computational effort compared to the non-linear regression method. This results in an overall higher precision.

The "non-linear regression method" on the other hand enables a compensation of discontinuities in the interference signal and, therefore, a larger measuring range compared to the direct evaluation of the fringes.

4.3.2 Explanatory Approach

Due to the lack of spectrometric tools, the spectral performance of mid-infrared semiconductor lasers under modulation has not yet been systematically investigated. The fact that the spectral dynamic range (i.e., the spectral modulation depth) decreases with increasing modulation frequency, as shown in Table 4.2 and Figure 4.7, was new even to the laser manufacturer. There is also no theoretical approach with which these measurement results could be compared.

However, the emission wavelength of a semiconductor laser is primarily determined by the geometric dimensions and the refractive index of the semiconductor material, and both parameters are significantly influenced by the laser temperature and thus indirectly by the injection current. A plausible explanation could therefore be a frequency-dependent temperature distribution of the semiconductor laser material. As the modulation frequency increases, there is less time available for establishing a thermal equilibrium. A changing frequency would therefore lead to a changing temperature distribution or the occurrence of (additional) inhomogeneities. Effects on the spectral emission are to be expected (Zeller et al., 2010).

4.4 Conclusions

Figure 4.2 does not perfectly correspond to the mathematical description given by Equation (4.10). From the equation it would be expected that mutual cancellation of the DC and AC components and adding occur alternately. However, this is not observable because on the one hand Equation (4.10) is based on several approximations and on the other hand the alignment of the individual partial beams in the Michelson interferometer is not perfect.

An analysis of the results presented in Figures 4.5 and 4.6 shows that the wavelength difference between the two methods is only of the order of a few hundredths of a nanometer. Figures 4.3 and 4.4 demonstrate that, with increasing modulation frequency, the wavelength change as function of operating current decreases. This limits the spectral range of the ICL which is particularly relevant for wavelength modulation.

The spectral tuning characteristics of the modulated laser $d\lambda/dI$ (Figure 4.3) and $\lambda(I)$ (Figures 4.4 to 4.6) can be approximated by quadratic polynomials and cubic polynomials, respectively. Compared to cw operation, the ICL thus shows a clearly nonlinear spectral behavior.

In cw operation, the tuning coefficient $d\lambda/dI$ for the nanoplus ICL 1541 equals approximately 0.16 nm/mA. Figure 4.3 shows that with decreasing modulation frequencies the individual curves approach this constant value.

The direct evaluation of fringes is a factor of four more precise than the nonlinear regression method, as fewer error-prone variables are included. However, the accuracy of both methods strongly depends on the precision of the reference wavelength derived from the transmission spectrum. An advantage of the non-linear regression method over the direct evaluation of fringes is a larger measurement range.

Compared to the state of art, both methods achieve a significantly higher resolution, which does additionally have the potential to be optimized by adjusting the path length difference of the Michelson interferometer.

A heterodyne (or super-heterodyne) interferometer would not provide advantages over the applied homodyne setup, especially with regard to spectral resolution. A significant disadvantage represents the need of a second often frequency-stabilized laser.

In conclusion, it should be mentioned that both methods can be adapted to other types of modulation (e.g., sinusoidal) and applied for the analysis of spectra recorded by wavelength modulation spectroscopy (D. Viveiros et al., 2014).

Note: Parts of this Chapter 4 were published in *Bahr and Wolff, 2021* and are partially edited.

Chapter 5

PAS-based isotopologic analysis of highly concentrated methane

5.1 Fundamentals of the Photoacoustic Effect and Photoacoustic Spectroscopy

Photoacoustic spectroscopy (PAS) is based on the photoacoustic effect discovered by Alexander Graham Bell in 1880 and is nowadays a significant optical method for the determination of trace gas concentrations (Bell, 1880). With the help of this method, one foreign molecule can be detected in a billion molecules (Palzer, 2020). This makes PAS-based identifications of analytes in the ppb range or even lower possible. The photoacoustic effect occurs in gases, as well as in liquids, and in solids. As can be deduced from the term photoacoustic, the effect is based on light (photo) and sound (acoustic). Accordingly, light energy is converted into sound energy. When laser light of a specific wavelength is absorbed by a gas molecule, it changes to the excited state. Based on complex relaxation processes, the change to a lower-energy state of the molecule occurs either by a radiative process, i.e. in the form of the emission of a photon, or by non-radiative processes. These non-radiative processes, which contribute to the formation of the photoacoustic signal, are based on the transfer of the internal energy (mainly vibrational energy, but also rotational energy) of the excited molecules into kinetic energy (translational energy) through inelastic collisions with neighboring molecules (Schilt et al., 2006). According to the kinetic theory of gases, the increase in kinetic energy causes an increase in the temperature of the gas (Giancoli, 2023). Since the volume in a measuring cell is constant, this temperature increase provides for a pressure change according to the ideal gas law.
The process of photoacoustic effect is schematically shown in Figure 5.1.

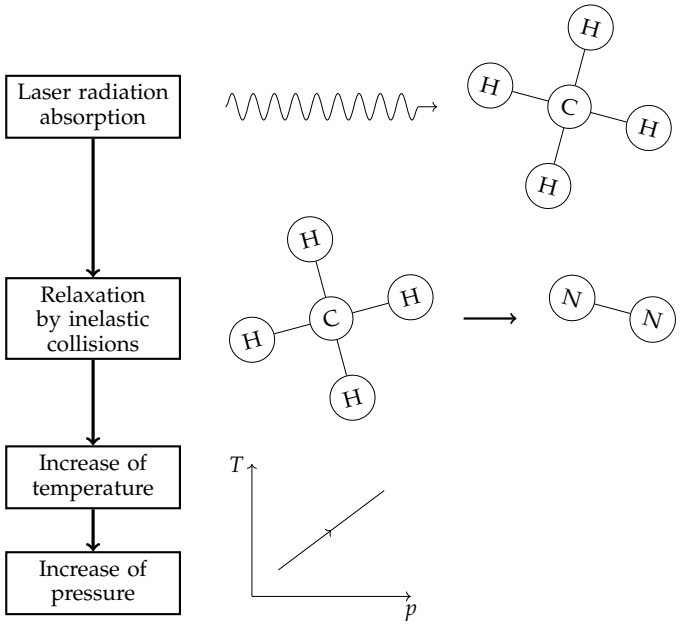

FIGURE 5.1: Flowchart of the photoacoustic effect.

In order to perform photoacoustic spectroscopy based on the photoacoustic effect, a modulation of the laser radiation used to excite the molecules is required. Modulation produces two positive and simultaneously necessary effects: On the one hand, measuring cells provide resonant geomtries, so that modulation of the laser radiation at the resonant frequency of the measuring cell amplifies the photoacoustic signal by a factor of 100-1,000. On the other hand, a standing sound wave is generated in the measurement cell corresponding to the modulation frequency, which, in conjunction with the amplification of the PAS signal caused by the measurement cell, produces a sufficiently high Signal-to-Noise Ratio (SNR) to be detected by an established sound transducer, such as a microphone (Miklós and Hess, 2000).

5.1.1 Modulation techniques

The established modulation method in PAS is indirect modulation using a mechanical chopper. This consists of a slotted, rotating disk, which is positioned between the laser and the measuring cell and causes an "on-off keying" modulation of the laser radiation. Based on this method, the photoacoustic spectrum of the analyte can be measured directly. However, the limited frequency stability associated with this causes non-reproducible deviations in the amplitude of the photoacoustic signal and thus reduces the accuracy in identifying the individual molecules present in the gas mixture (Germer and Wolff, 2010).

A much more precise and reproducible modulation method consists of direct modulation of the laser used with respect to its wavelength. In the case of the ICL, the emitted wavelength can be tuned by changing the operating current, among other things. If the operating current is modulated sinusoidally, for example, the result is wavelength modulation spectroscopy (WMS) (Wang et al., 2018). However, this modulation method is not trivial, as the investigations in Chapter 3 have shown. The non-linear behavior of the ICL in the operating current modulation mode results in the recorded photoacoustic signal not matching the theoretical spectra as calculated in HITRAN, for example. Insofar as the spectra measured by direct operating current modulation must be evaluated quantitatively, the use of artificial intelligence, or machine learning, is essential.

5.1.2 Demodulation of the PA Signal

The information contained in the PA signal is present in modulated form by the signal detected by the transducer. Demodulation is required to extract the useful signal from the PA signal. As an established method, a lock-in amplifier is used, which uses the modulation signal frequency for demodulation purpose (Burdett, 2005). The modulated PA signal $u_{PA}(t)$ is mixed down to the baseband in parallel by a cosine and a sine oscillator, both operating at modulation frequency. In this way, the in-phase ($I(t)$) and quadrature ($Q(t)$) signals are created in this series. Subsequently, a low-pass filter is used to suppress the high-frequency signal components, so that the PA signal emerges as a DC signal $u_{DC}(t)$ from the inphase and quadrature signal

branches after magnitude formation, which removes the phase deviation between $u_{PA}(t)$ and the oscillator's reference signals. The flowchart for lock-in amplifier based demodulation is shown in Figure 5.2.

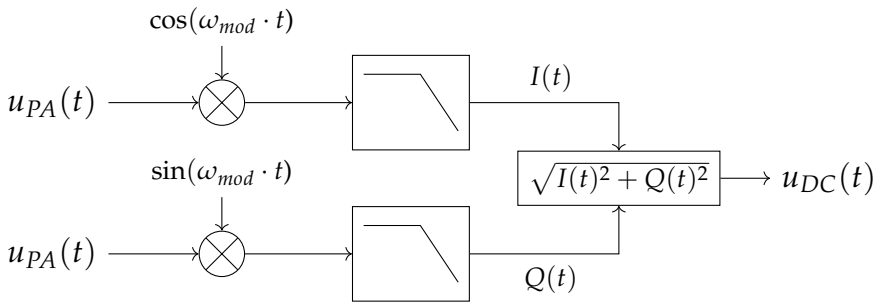

FIGURE 5.2: Flowchart lock-in amplifier based PA signal demodulation.

In the case of indirect modulation of the laser by "on-off keying", the demodulated DC signal corresponds to the theoretical spectrum amplitude of the gas mixture as a function of the emitted wavelength of the laser. If the direct sinusoidal modulation of the laser injection-current is used, in case of demodulation on the modulation frequency, a $1f$-spectrum is obtained, i. e. the derivative of the theoretical spectrum as a function of the wavelength.
Lock-in amplifiers exist as ready-to-use hardware components based on digital signal processing. In the context of this work the Model 7265 of the company Ametek was used.
Since the demodulation described by the lock-in amplifier corresponds to a Discrete Fourier Transform (DFT) in the case of finite, discrete-time signals, the demodulation can also be implemented highly efficiently in the form of a Goertzel algorithm. This calculates only the required spectral component and not the entire spectrum. Since the computation of the spectrum by the Goertzel algorithm is limited to a few computational operations, real-time implementations, e.g. on DSPs, are possible (Engelberg, 2008).

5.1.3 Quartz Enhanced Photoacoustic Spectroscopy - QEPAS

A further development of the microphone-based detection of the photoacoustic signal is quartz-enhanced photoacoustic spectroscopy (QEPAS). According to the name, the microphone is replaced by a quartz tuning fork (QTF). The first public demonstration of the new technology took place in 2002 (Kosterev et al., 2002). The QTF and thus QEPAS offer some advantages, but also disadvantages, as will be explained below.

Because the resonant frequency of the QTF is typically around 32.768 kHz, the associated acoustic resonator lengths can be kept very short. Their typical lengths are in the mm range. This allows a very compact measurement setup. Furthermore, QTFs have Quality-factors (Q-Factor) around 10,000 in standard atmosphere. Since the Q-Factor is determined as the quotient of center frequency and bandwidth, the QTF thus acts as a very narrowband bandpass filter, which means that the noise bandwidth is many times smaller compared to measurements with a microphone. This leads to a significantly higher SNR at the transducer (Ma, 2018).
However, the very narrowband filter effect of the QTF can also have a strongly detrimental effect depending on the application. If the modulation frequency of the laser used deviates only slightly from the actual resonance frequency of the QTF, the SNR is no longer sufficient to detect the smallest concentrations.
Furthermore, the dynamic range of a QEPAS sensor with respect to concentrations is significantly limited compared to the classical PAS sensor. Since the resonant frequency of the microresonator used depends on the speed of sound, which is determined by the composition of the analyte, especially in the high concentration range, e. g. for concentrations typical of natural gas, even small deviations from the reference value of the microresonator cause a shift in the resonant frequency, which significantly reduces the SNR.
Due to these conditions, only microphone-based PAS was used for the following measurements, since the resonant frequency of the resonator is significantly affected by the concentrations measured subsequently.

In the following, measurements of $^{12}CH_4$ and $^{13}CH_4$ mixtures in nitrogen with concentrations of 25–70% and 0.28–3.00%, respectively, under laboratory conditions, are presented. The measurement results are then evaluated using cross-validation in conjunction with Partial Least Squares Regression (PLSR). This process is also used for sensor calibration. Section 5.2 shows the relevant methane absorption spectra and describes the experimental setup and the measurement procedure. Section 5.3 presents the resulting measurements, which are subsequently discussed in Section 5.4.

5.2 Methods and Materials

5.2.1 $^{12}CH_4$ and $^{13}CH_4$ Absorption Spectra

The isotopologic analysis has been performed using a spectrally tunable interband cascade laser (ICL) emitting in the spectral range of the fundamental vibration of $^{12}CH_4$ and $^{13}CH_4$. Figure 2.5 shows the absorption spectra of the two isotopologues at room temperature (296 K) and atmospheric pressure (1,013.25 hPa) (HITRAN, 2022). The optimum center wavelength of the laser has been determined using the mathematical algorithm described in Chapter 3. Figure 5.3 displays the Q-branches of the fundamental vibrational absorption together with the tuning range of the laser, represented by the yellow box.

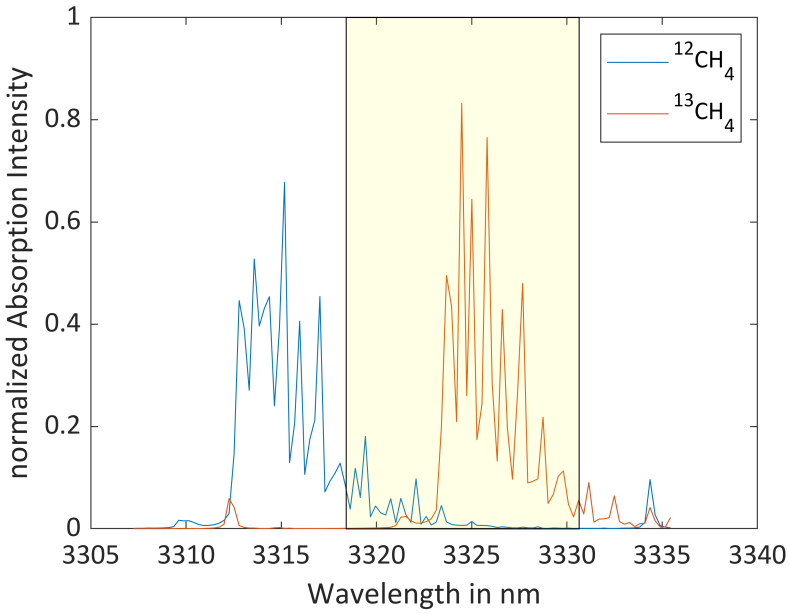

FIGURE 5.3: Q-branches of the fundamental vibrational absorption spectra of $^{12}CH_4$ and $^{13}CH_4$ (Gordon et al., 2022) together with the tuning range of the ICL (yellow box) (Bahr and Wolff, 2022).

5.2.2 Measurement setup

The measurement setup is schematically shown in Figure 5.4. The ICL 3272 used in this investigation was manufactured by nanoplus GmbH (Gerbrunn, Germany). It exhibits a center wavelength of 3,323 nm with a spectral linewidth below 20 MHz. The laser can be operated at temperatures between 20 and 30 °C. Stimulated emission occurs with electric currents between 19 and 120 mA.

The ICL is operated using the Thorlabs (Newton, MA/United States) laser diode driver TLD001 and its temperature is controlled by the Thorlabs controller TTC001. The laser current can be set with an accuracy of 10 µA. The noise level is below 3 µA rms. The ICL chip has been installed in a TO66 housing including a Peltier element and a temperature sensor for temperature regulation. The laser provides single-mode emission that is spectrally continuously tunable between 3,318.41 nm and 3,330.64 nm. The maximum output power is approximately 15 mW. The laser beam passes centrally through the cylindrically symmetrical photoacoustic cell. The custom-made cell is designed according to the established H geometry featuring a longitudinal resonance around 3 kHz (Nodov 1978). The resonance tube is 60 mm long with a diameter of 6 mm and the buffer volumes at both ends of the cell have each a length of 30 mm and a diameter of 24 mm, resulting in a total absorption length of 120 mm. The photoacoustics signal is detected by the analog microphone ROM-2235P-HD-R from PUI Audio (Fairborn, OH/United States) which is mounted in the center of the cell with the membrane flush with the inner wall. It exhibits a diameter of 5.8 mm and a detection sensitivity of -35 ± 3 dB at 1 kHz and 50 cm distance. The Ametek/Signal Recovery lock-in amplifier DSP LIA (Berwyn, IL/United States) performs the phase-sensitive detection of the microphone signal. The Owon (Zhangzhou, China) function generator AG 1022 provides the frequency reference for the ICL modulation and the lock-in detection. The entire experimental setup is controlled using a MATLAB script on a PC. The PLSR algorithm including the leave-one-out cross-validation is implemented in a MATLAB script and performed by the PC.

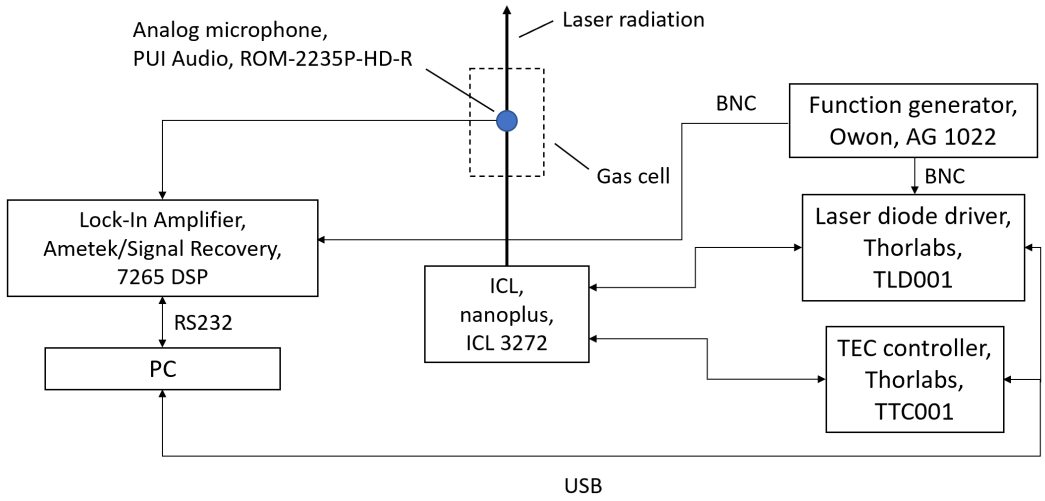

FIGURE 5.4: Experimental setup (Bahr and Wolff, 2022).

The gas flow system is schematically shown in Figure 5.5. Gas is provided in three containers:

1. CH_4 of natural isotopologue abundance (1 L geometric volume, 12 bar filling pressure, purity: 4.5, distributor: Westfalen AG),
2. $^{13}CH_4$ (416 ml geometric volume, 2.3 bar filling pressure, purity: 99%, distributor: Merck/Sigma Aldrich),
3. N_2 (10 L geometric volume, 200 bar filling pressure, purity: 5.0, distributor: Westfalen AG).

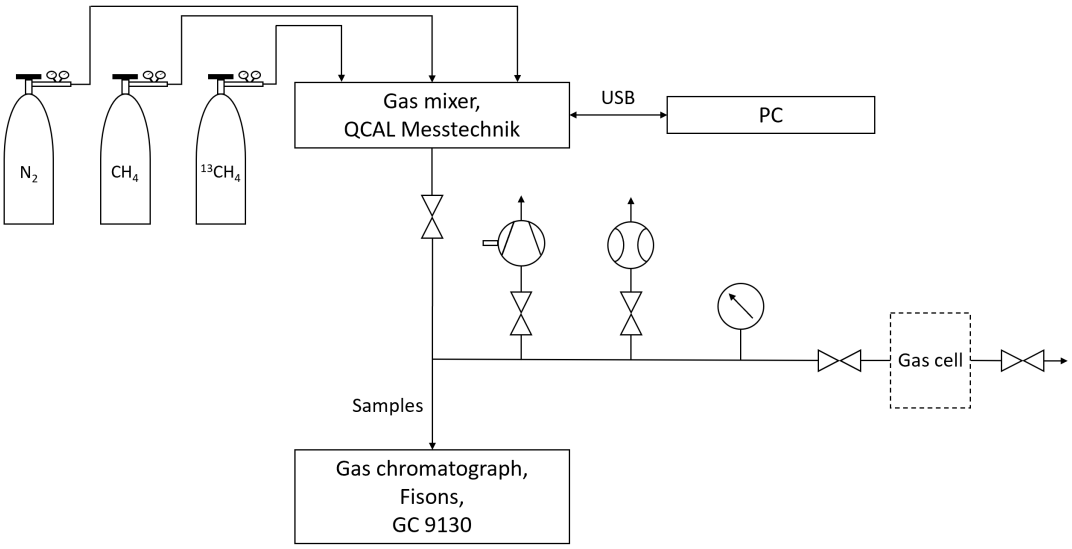

FIGURE 5.5: Gas flow system (Bahr and Wolff, 2022).

Mixtures are generated using the 6 Channel Gas mixer from QCAL (Munich, Germany) which is controlled by a PC. The maximum relative error of the mixture concentrations, specified by the manufacturer, is up to 2%. To ensure the correctness of the mixer performance, all compositions are analyzed by the gas chromatograph 9130 from Fisons (Ipswich, United Kindgom). The photoacoustic measurements were performed under static conditions after the gas mixtures were injected into the gas cell.

5.2.3 Measurement procedure

Photoacoustic spectroscopy is based on the absorption of modulated radiation and the subsequent conversion of the absorbed energy by collisions into a thermal wave and consequently into a pressure wave. This sound wave can be amplified taking advantage of an acoustic resonance of the sample

cell and is usually detected by a microphone (Demtröder, 2014a; Demtröder, 2014b).

The ICL applied in this investigation is directly injection-current modulated at a constant operation temperature of 20 °C. The current consists of one part that is continuously tuned between 75 and 120 mA covering a spectral range of approximately 12 nm and a second, sinusoidally modulated part that is responsible for the generation of the PA signal. The latter exhibits a modulation amplitude of 1.24 mA which corresponds to a spectral range of approximately 0.1 nm.

The frequency of the reference signal fed into the lock-in amplifier equals the resonance frequency of the measurement cell. This leads to a 1f wavelength modulation, as a result of which the recorded spectra correspond to the derivative of the absorption spectra. The advantage of this modulation method is that changes in the spectra are emphasized. This makes it easier to distinguish different gas components.

The acoustic resonance of a sample cell depends sensitively on the speed of sound. Due to the significant mass difference, doubling or tripling a methane concentration of 25% in an N_2 matrix considerably changes the speed of sound resulting in a large shift of the cell's resonance frequency (Selvaraj et al., 2019). Figure 5.6 illustrates this phenomenon. It shows the PA signal as function of the modulation frequency for (total) methane concentrations of 26.25%, 52.25%, 73.00% and 100.00%. Shifts in the resonant frequency due to temperature fluctuations of a few degrees Celsius are comparatively negligible. The subsequent analytical measurements were all performed at a modulation frequency of 3,187 Hz.

Over a large range, the PA signal is proportional to the concentration of the absorbing molecules. However, if the absorption is extremely strong, as in the case of the fundamental asymmetric stretching ν_3 of methane, and/or the concentration of the absorbing species is very high, saturation occurs and deviations from this linear relationship arise (Menduni et al., 2022). In Figure 5.6 it can be observed that the PA signal at the respective resonance frequency decreases as the methane concentration increases from 26.25% to 100.00%. The reason for this is twofold. Firstly, the majority of the absorption takes place in an increasingly shorter path length behind the entrance

window. As a consequence, the overlap between the longitudinal mode and the intensity distribution of the laser will be weaker and the cell resonance is stimulated less effectively (Baumann et al., 2006, Baumann et al., 2007). The linear dependency between concentration and photoacoustic signal that applies in the ppm and ppb range is then no longer observable. For methane concentrations in the single digit percentage level the photoacoustic signal still increases with increasing concentration, however the dependence is non-linear (Zeninari et al., 2016). If concentrations are in the high percentage range, as shown in Figure 5.6, there is a reduction in amplitude with further increasing concentration.

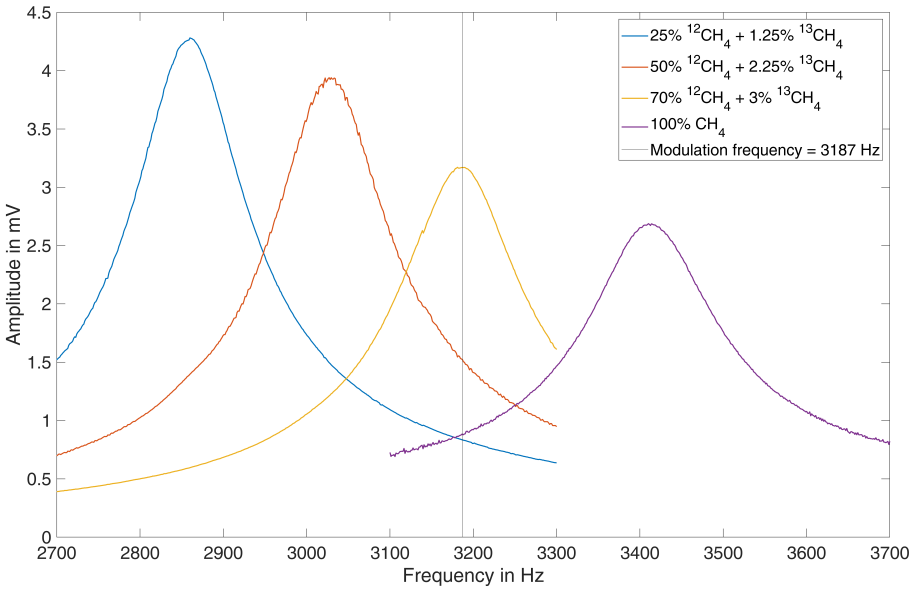

FIGURE 5.6: Photoacoustics signal as function of the modulation frequency for different mixtures (Bahr and Wolff, 2022).

This phenomenon is superimposed by a second effect. The photoacoustic signal generation is based on the transfer of internal energy of excited molecules (mainly vibration but also rotation) into kinetic energy of neighboring molecules (translation) via inelastic collisions. Therefore, the composition of the gas matrix significantly affects the relaxation dynamics and thus the photoacoustic response. Due to the high purity of the gas samples, the controlled laboratory environment and the evacuable gas flow system it is not expected that water vapor or other impurities play a major role in the relaxation process. Since there are no significant differences between the relaxation times of the two

methane isotopologues, the $^{12}CH_4/^{13}CH_4$ ratio should also not have a substantial influence on the photoacoustic signal (Giglio et al., 2022). As no efficient vibro-vibrational (V-V) transition between the ν_3 state of CH_4 (CH_4^*) and N_2 exists, only three non-radiative relaxation channels are possible (Schilt et al., 2006):

1. CH_4^*-N_2 collision followed by a vibro-translational (V-T) transition. This relaxation channel represents the main source of the PA signal if N_2 is present in the mixture.

2. CH_4^*-CH_4 collision followed by V-V transitions. This relaxation channel does not contribute to the PA signal.

3. CH_4^*-CH_4 collisions followed by a V-T transition. This relaxation channel represents an additional source of the PA signal. The respective signal is phase-shifted in relation to the CH_4^*-N_2 signal. If no N_2 is present in the mixture, it is the only source of the PA signal.

In the analytical measurements the (total) methane concentration are varied between 25 and 73%. This changes the number of nitrogen molecules available for the according V-T collisions considerably and thus determines the efficiency of the photoacoustic signal generation.

The evaluation algorithm responsible for the sensor calibration has to be able to compensate the changing dependencies originating from the effectivity of the acoustic resonance stimulation as well as the matrix effects arising from changes in the gas composition.

5.3 Results

Table 1 lists the nine isotopologue mixtures that were investigated. The residual gas to 100% was always N_2. The $^{12}CH_4$ concentrations were chosen to cover the two-digit percentage range as complete as possible. The choice of $^{13}CH_4$ concentrations was severely restricted due to the flow limitations of the gas mixer. Figure 5.7 to Figure 5.9 show the respective photoacoustic spectra, i.e. the PA signal as function of the average laser current. All measurements were taken at a sample temperature of 26 °C and a pressure of 1,016 hPa.

TABLE 5.1: $^{12}CH_4$ and $^{13}CH_4$ concentrations of the nine investigated mixtures (rest: N_2) (Bahr and Wolff, 2022).

Figure No.	$^{12}CH_4$ **concentration**	$^{13}CH_4$ **concentration**
Figure 5.7	25%	- 0.28% - 0.75% - 1.25%
Figure 5.8	50%	- 0.56% - 1.75% - 2.25%
Figure 5.9	70%	- 0.78% - 2.25% - 3.00%

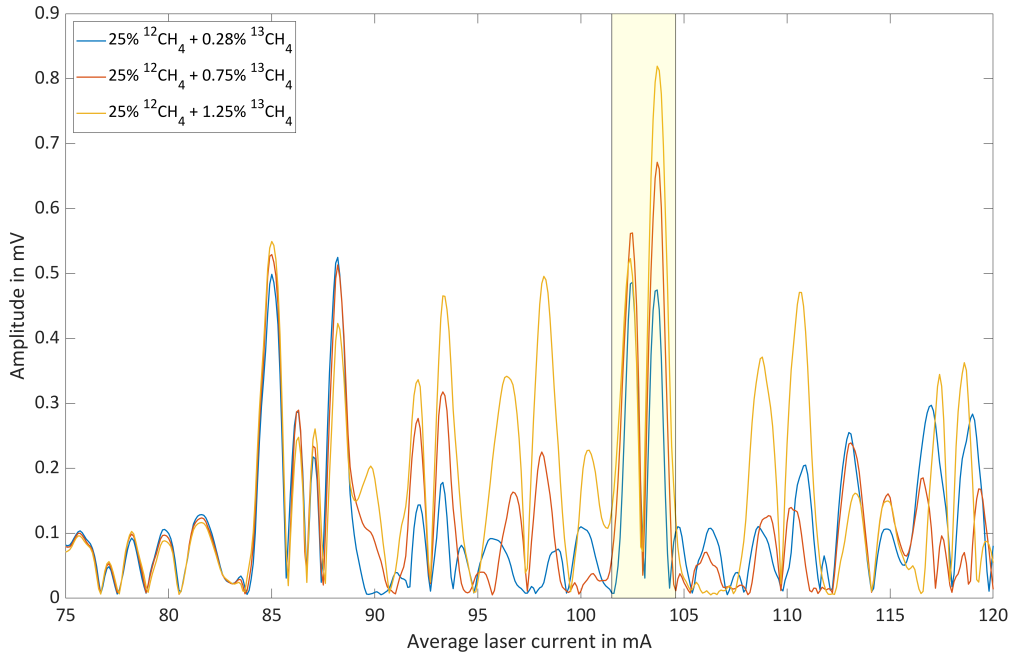

FIGURE 5.7: Photoacoustic signal as function of the average laser current for 25% $^{12}CH_4$ with three different $^{13}CH_4$ shares in nitrogen (Bahr and Wolff, 2022).

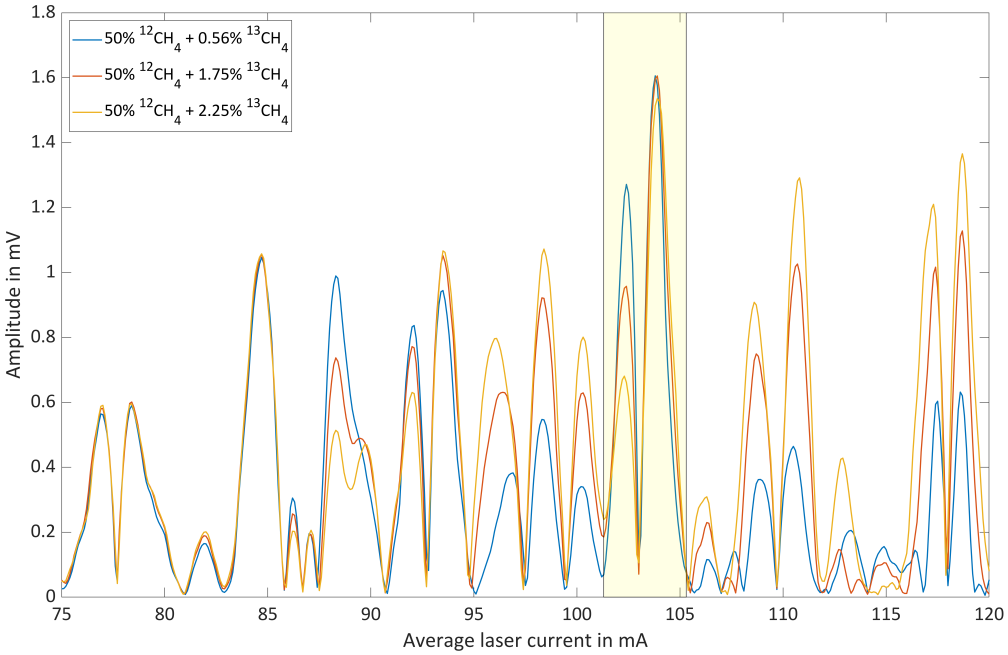

FIGURE 5.8: Photoacoustic signal as function of the average laser current for 50% $^{12}CH_4$ with three different $^{13}CH_4$ shares in nitrogen (Bahr and Wolff, 2022).

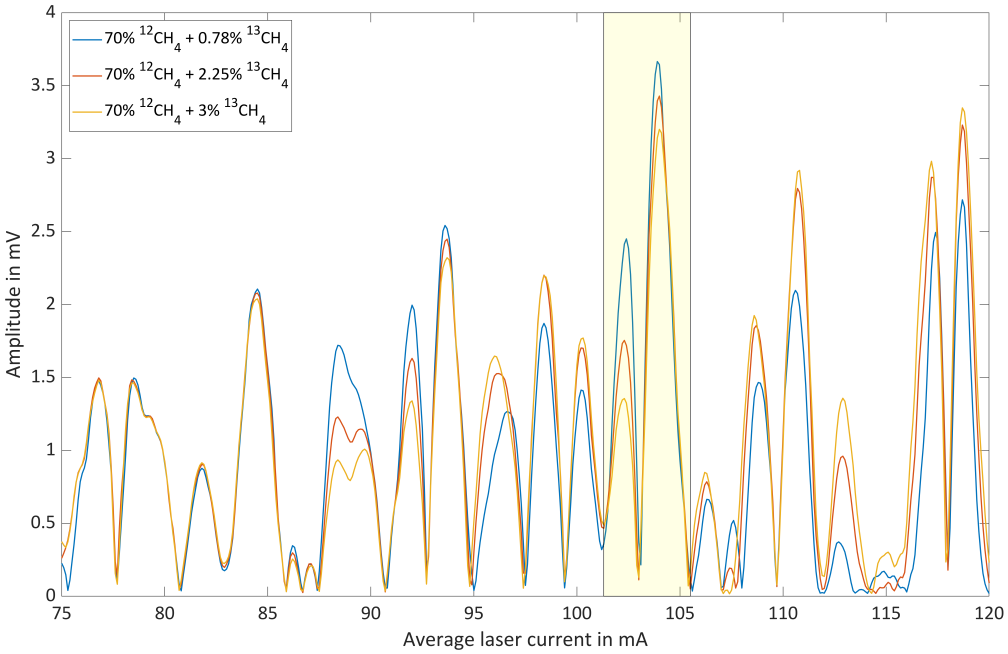

FIGURE 5.9: Photoacoustic signal as function of the average laser current for 70% $^{12}CH_4$ with three different $^{13}CH_4$ shares in nitrogen (Bahr and Wolff, 2022).

Considering the complexity of the collected spectra a sensor calibration in the form of a quantitative multivariate approach is implemented to validate the methane isotopologue concentrations and to test the suitability of the method. In particular, Partial Least Squares Regression (PLSR) proved to be applicable for determining the concentrations of mixture components from photoacoustic spectra (Loh and Wolff, 2020; Saalberg and Wolff, 2018). Figure 5.10 shows the true and the predicted methane isotopologue concentrations, after a leave-one-out cross-validation based on PLSR was applied to all nine investigated mixtures. The mixture numbers in Figure 5.10 correspond to the order given in Table 5.1. The absolute root-mean-square-errors for the predicted $^{12}CH_4$ and $^{13}CH_4$ concentrations were calculated to 3.08% and 0.29%, respectively.

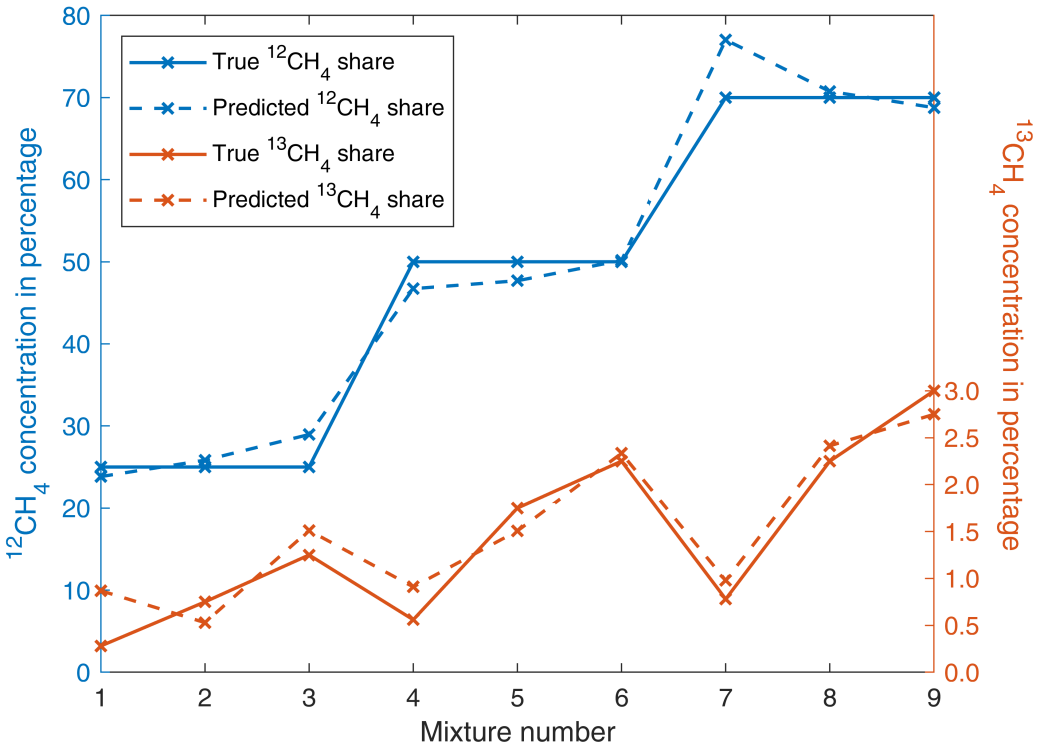

FIGURE 5.10: Evaluation of the investigated methane isotopologue mixtures by leave-one-out cross-validation based on PLSR (Bahr and Wolff, 2022).

5.4 Discussion

Figures 5.7 to 5.9 show wavelength-modulated photoacoustic spectra that were measured using the single modulation frequency ($1f$) as reference for

the lock-in amplification. Therefore, they represent approximately the derivative of the absorption spectrum (Demtröder, 2014a; Demtröder, 2014b). However, due to the nonlinear spectral behavior of injection current modulated semiconductor lasers, the agreement is not perfect (Bahr and Wolff, 2021). In addition, the spectra are not normalized with respect to the emission power of the laser and the output depends considerably on the modulation amplitude.

The spectral tuning range of the laser was selected using an optimization algorithm in such a way that not only characteristic absorption lines of both isotopologues are accessible, but that these lines also have absorption strengths of the same order of magnitude around the isotopologue ratio of interest (natural abundance). The latter is important as it ensures that the signal levels are comparable.

The spectral region associated with average laser currents between 75 mA and 85 mA is clearly dominated by $^{12}CH_4$ lines. This is illustrated by the fact that the according peaks are only weakly dependent on the 13CH4 concentration. However, the dependence of the photoacoustic signal on the $^{12}CH_4$ concentration is significant. The spectral region associated with average laser currents between 85 mA and 120 mA, on the other hand, is obviously characterized by $^{13}CH_4$ absorption. However, $^{12}CH_4$ exhibits a considerable contribution in this range leading to a base-signal that increases with increasing $^{12}CH_4$ concentration. The $^{13}CH_4$ concentration dependent signal inversion, which is for instance observable between 25% and 50% $^{12}CH_4$ around 103 mA, marked by yellow boxes, can be explained as a result of two opposing effects:

1. Increasing signal with increasing concentration due to higher absorption.

2. Decreasing signal with increasing concentration due to less effective stimulation of cell resonance (see Section 5.2.3).

The inversion can only be observed at selected average laser currents because the phenomenon requires a specific combination of absorption path length, absorption coefficient and concentration, in which the contributions of the two isotopologues add up.

In conclusion it can be stated that, even though the number of investigated mixtures of the two main methane isotopologues $^{12}CH_4$ and $^{13}CH_4$ is, with nine samples, quite limited and the error of the gas mixer used is significant, the measurements displayed in Figures 5.7 to 5.9 and the evaluation based on PLSR displayed in Figure 5.10 prove to a satisfactory extent that photoacoustic spectroscopy is a suitable method for the isotopologic analysis of highly concentrated methane. The accuracy of the sensor can be considerably improved by adding more measurements to the training data of the PLSR algorithm. The presented results with samples in the high double-digit percentage range make it appear possible to analyze undiluted natural gas samples. However, the presence of other hydrocarbons would make this task significantly more challenging. In any case, it is important to consider the resonance frequency shift associated with concentration changes.

Chapter 6

PAS-based analysis of natural gas samples

While in Chapter 5 only artificial mixtures of methane main isotopologues were measured PAS-based, in this chapter real natural gas samples are investigated. In the following, a photoacoustic analyzer that can determine the concentrations of methane, ethane and propane of real natural gas samples is described. The sensor is a further development of the setup described in Chapter 5. The investigated natural gas originates from the house supply of Hamburg University of Applied Sciences (Hamburg, Germany). Furthermore, gas samples originating from a German natural gas storage are investigated. In this regard, a method for preparing gas samples of atmospheric pressure for the photoacoustic measurement is presented.

6.1 Methods and Material

6.1.1 Methane, Ethane and Propane absorption spectra

The analyzer is based on an interband cascade laser (ICL) emitting in the mid-infrared range. Figure 6.1 shows the normalized absorption spectra of methane, ethane and propane at room temperature (296 K) and atmospheric pressure (1013.25 hPa). The center wavelength of the laser has been empirically selected to be 3324.15 nm and is displayed by the vertical dark line in the yellow box in Figure 6.2. To clearly identify several components of a gas mixture, it is necessary to analyze the spectrum in a specific range. For this purpose, the laser is spectrally tuned. The yellow box represents the laser tuning range whose spectral bandwidth is approximately 5.3 nm.

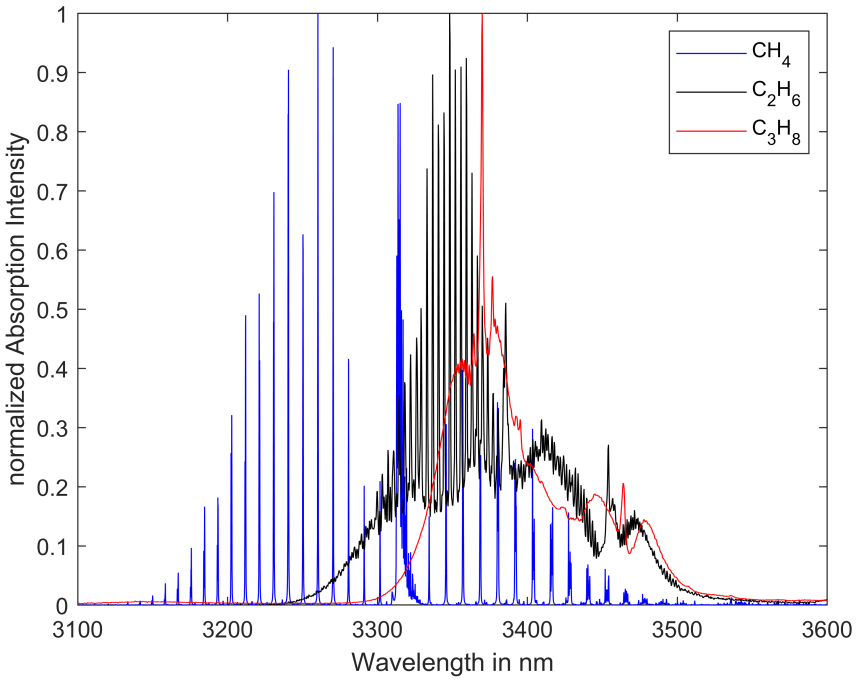

FIGURE 6.1: Absorption spectra of methane, ethane and propane (GEISA, 2022; Gordon et al., 2022).

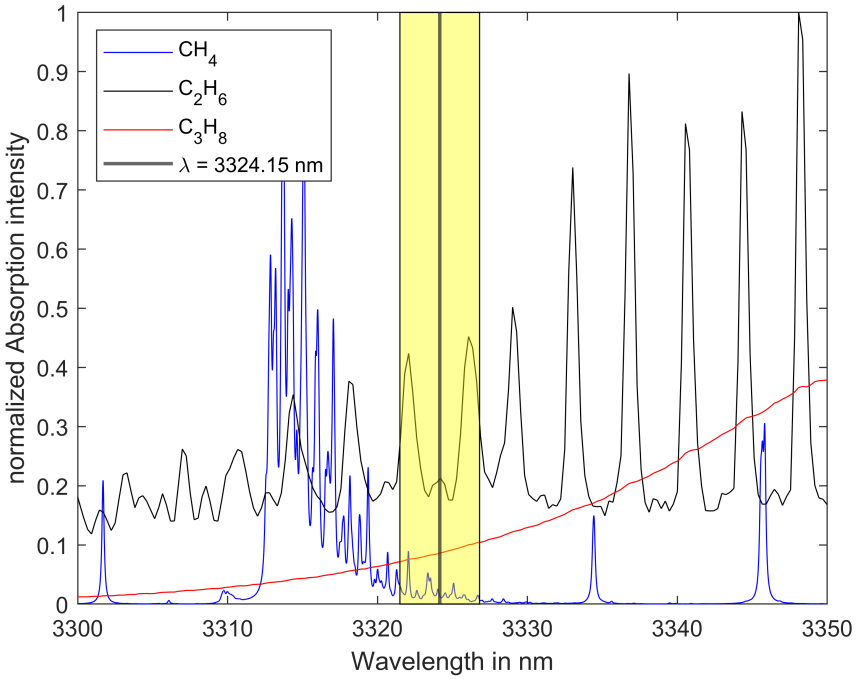

FIGURE 6.2: Absorption spectra of methane, ethane and propane together with the laser tuning range (yellow box) and the laser center wavelength (GEISA, 2022; Gordon et al., 2022).

6.1.2 Measurement setup

The measurement setup is schematically shown in Figure 6.3. The ICL 3272 manufactured by nanoplus GmbH (Gerbrunn, Germany) emits radiation around 3323 nm with a spectral linewidth smaller than 20 MHz. The laser chip temperature can be varied between 20 and 30 degrees Celsius. Laser operating currents between 19 and 120 mA allow stimulated emission. For the operation of the ICL the Thorlabs (Newton, MA/USA) laser diode driver TLD001 and the temperature controller TTC001 are used. The TLD001 allows to set the laser current with an accuracy of 10 µA with a noise level below 3 µA rms. Installed in a TO66 housing, the ICL chip temperature is controlled using a temperature sensor and a Peltier element. The single-mode emission can be continuously tuned between 3318.41 nm and 3330.64 nm. Approximately 25 mW output power can be reached at maximum. The cylindrically symmetrical photoacoustic measurement cell, that the laser beam centrally passes, is designed according to the established H geometry boasting a longitudinal resonance around 3 kHz (Nodov, 1978). The photoacoustic signal is detected with the analog microphone ROM-2235P-HD-R from PUI Audio (Fairborn, OH/USA) which is mounted in the center of the cell, membrane flush with the wall. The microphone exhibits a diameter of 5.8 mm and a detection sensitivity of -35±3 dB at 1 kHz and 50 cm distance. The temperature of the measurement cell is controlled by the A-senco (Aalen, Germany) temperature controller, which heats the cell to a constant temperature above the ambient temperature by means of two heating mats. The maximum heating power is 30 W. The demodulation is performed on a Texas Instruments (Dallas, TX/USA) TMS320C6713 digital signal processor (DSP) which is mounted on the Texas Instruments TMDSDSK6713 evaluation board. The laser current modulation is controlled by the digital signal processor as well. A PC is used to control laser diode driver, TEC controller and DSP. The photoacoustic signals calculated by the DSP are recorded by the PC as function of the average current. These spectra of known mixtures serve as basis for a PLSR model based on a MATLAB script, which can subsequently be used to calculate the concentrations of the single components of unknown mixtures.

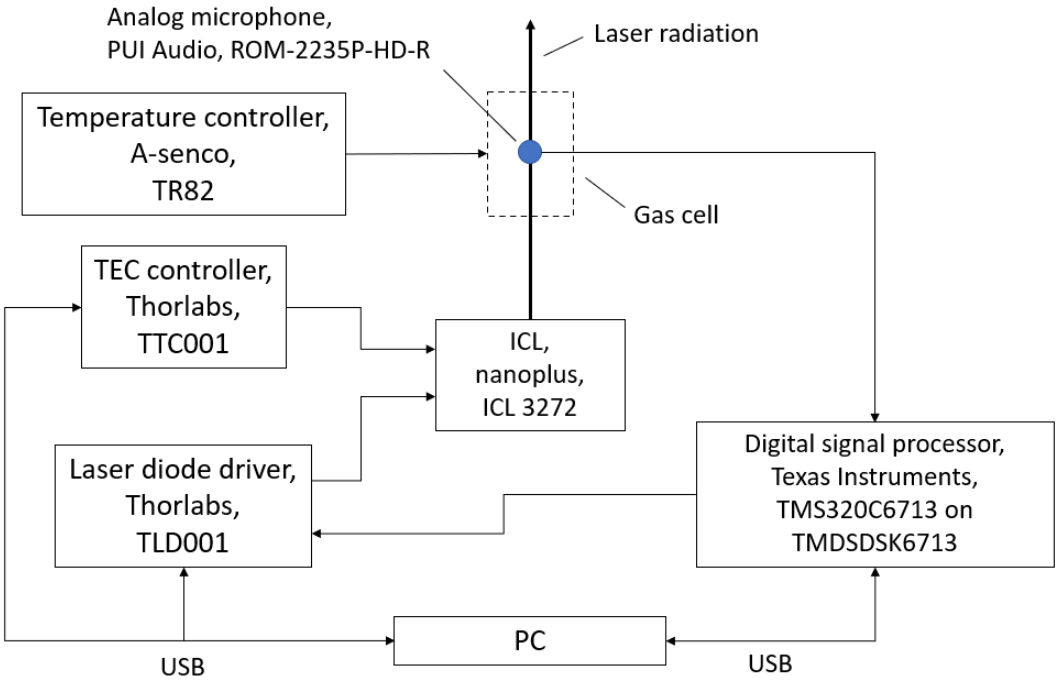

FIGURE 6.3: Experimental setup.

The gas flow system for the generation of the calibration mixtures is schematically shown in Figure 6.4. The gas is provided in four containers:

- CH4: 10 L geometric volume, 200 bar filling pressure, purity: 2.5, distributor: Westfalen AG,
- C2H6: 1 L geometric volume, 12 bar filling pressure, purity: 2.0, distributor: Westfalen AG,
- C3H8: 1 L geometric volume, 7.3 bar filling pressure, purity: 2.5, distributor: Westfalen AG,
- N2: 10 L geometric volume, 200 bar filling pressure, purity: 5.0, distributor: Westfalen AG.

All gas mixtures for calibration are generated using the 4-channel gas mixer based on Vögtlin Instruments GmbH (Muttenz, Swiss) mass flow controllers (MFC), which are distributed by HTK Hamburg GmbH (Hamburg, Germany). The maximum relative error of a single MFC is specified to be up to 1%.

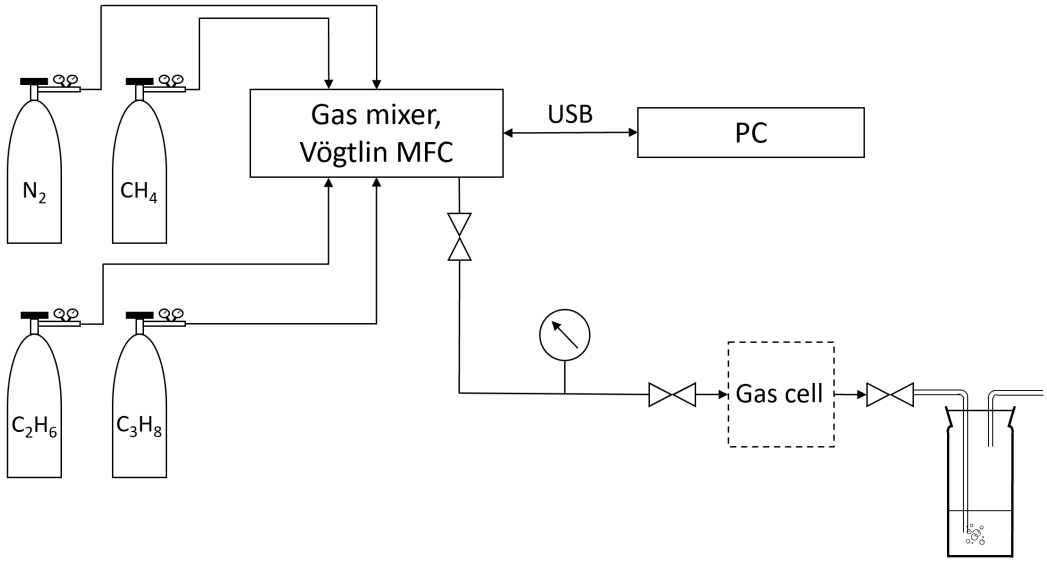

FIGURE 6.4: Gas flow system.

The validation measurements of the natural gas samples were carried out using the Shimadzu (Kyōto, Japan) GC 2014, which is equipped with an FID and a thermal conductivity detector (TCD). The relative measurement error is specified to be up to 2%.

The storage gas sample was provided by GEO-data (Garbsen, Germany) in a gas collection tube with a geometric volume of about 350 ml. The storage gas originates from a natural gas storage facility within Germany. Its preparation has been performed using the setup shown in Figure 6.5. A lecture bottle (geometric volume approximately 400 ml) was evacuated by the VACUUBRAND GmbH & Co. KG (Wertheim, Germany) Chemistry-HYBRID pump down to 0.1 mbar absolute pressure.

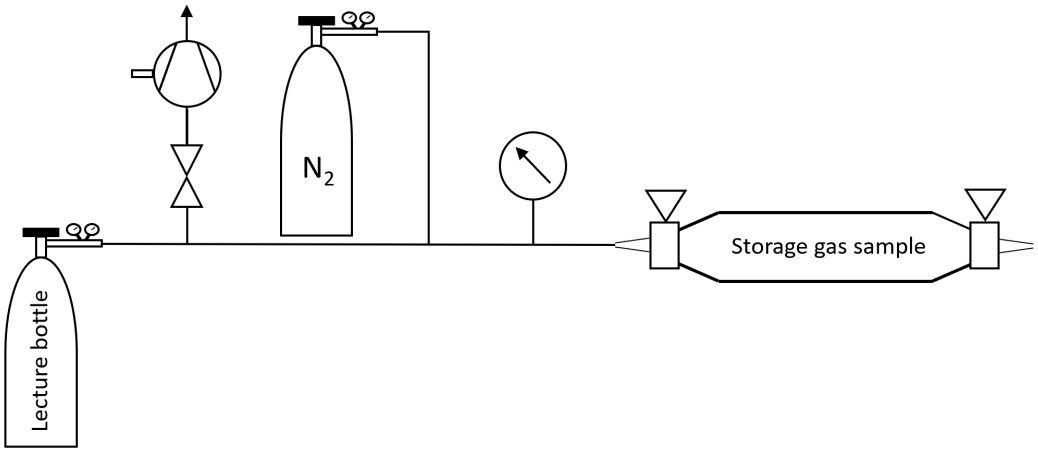

FIGURE 6.5: Storage gas preparation system.

The natural gas samples used are from Hamburger Energiewerke GmbH (Hamburg, Germany) and were obtained from the house gas connection of the Hamburg University of Applied Sciences.

6.1.3 Measurement procedure

At a constant temperature of 20 degrees Celsius, the ICL applied in this investigation is operated in the injection-current modulation mode. The injection-current consists of two parts. One part is continuously tuned between 66.00 and 120.12 mA covering a spectral range of approximately 5.3 nm. The other part is sinusoidally modulated with an amplitude of 1.18 mA which corresponds to a spectral range of approximately 0.1 nm.
The temperature of the measurement cell is set and controlled to constant 30 degrees C by the temperature controller.
The microphone signal is sampled at a sampling rate of 44.1 kHz. The recorded spectra consist of 315 points, with each spectral component calculated from 1,500 samples. The demodulation of the microphone signal on the DSP, based on the Goertzel algorithm, is performed at the injection-current modulation frequency at 3,528 Hz (Engelberg, 2008). The resulting spectra correspond approximately to the first derivative of the absorption spectra, which emphasizes the changes in the absorption coefficient, induced by changes in the single gas concentrations.
Figure 6.6 shows exemplary photoacoustic spectra, i.e. the PA signals as function of the average laser current after the Goertzel algorithm based demodulation on the DSP. All measurements were taken at a sample (cell) temperature of 30 degrees C and a pressure of 1,013 hPa.

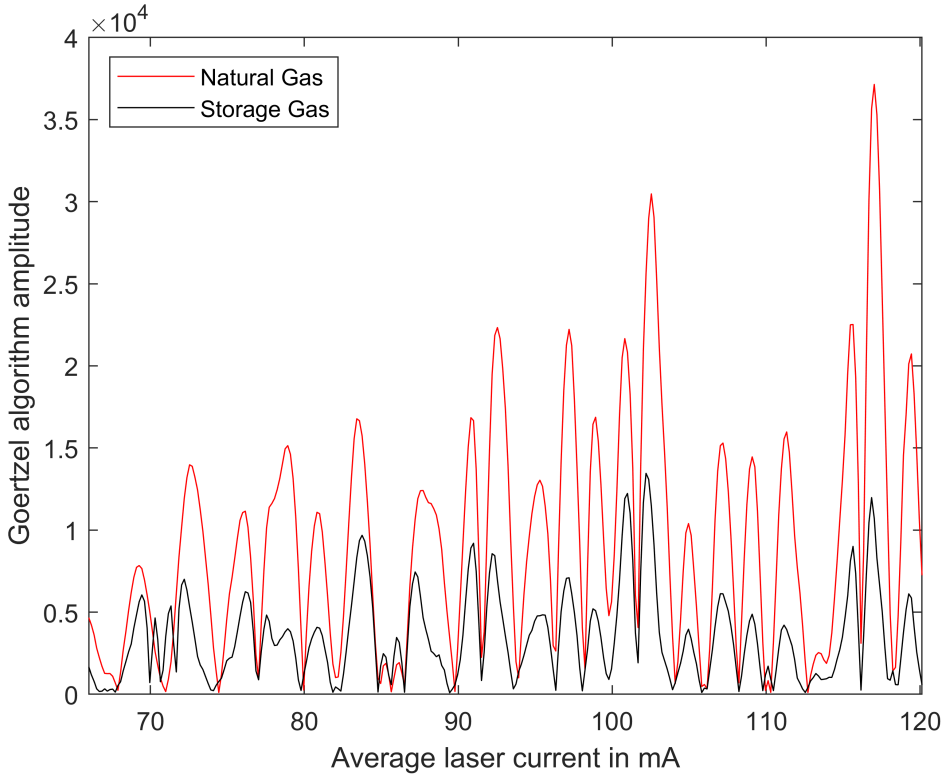

FIGURE 6.6: Exemplary photoacoustic spectra of natural gas and storage gas measured on 28th June 2023 and 29th June 2023, respectively.

The investigation of complex gas mixtures such as natural gas requires a multivariate approach to determine the methane, ethane and propane shares. As shown in previous investigations, Partial Least Squares Regression (PLSR) proved to be suitable for this task (Menduni et al., 2022). Reference calibration measurements of the photoacoustic sensor are required to predict the individual shares of the natural gas samples with a high precision and reliability. A training data set of 20 different mixtures has been used, all concentrations are uniform distributed. All calibration gas mixtures consist of methane, ethane and propane. The calculation of the PLSR model is performed on the PC. The magnitudes of the spectrum represent the predictor scores and the corresponding known concentrations provide the response scores. The beta-parameters are the result of the PLSR model calculation, which are the basis for the prediction of gas mixture compositions. By multiplication and summation operations of the beta-parameters with the spectra of unknown mixtures, the concentrations of its hydrocarbon components are calculated (Rosipal and Krämer, 2006).

A complete measurement run including calculation of the unknown hydrocarbon concentrations of a gas mixture requires approximately 12 seconds.

The filling and purging of the measuring cell are carried out as shown in Figure 6.4 using gas samples with overpressure relative to the atmosphere. If the gas samples do not have an overpressure, they must be prepared according to Figure 6.5. In this case, a lecture bottle is evacuated. The pressure in the system is less than 0.5 mbar when evacuated. The valve of the gas collection tube is subsequently opened and a constant pressure lower than the ambient pressure is established in the system. To generate the necessary overpressure relative to the atmosphere, the lecture bottle is then filled with nitrogen up to 4 bar above atmospheric pressure. This procedure allows a sample preparation adequate for the measurement cell. The concentration ratios of the single hydrocarbons, except for nitrogen, remain unchanged.
For GC analysis, the samples are injected into the GC by means of a dosing loop which, in conjunction with a valve circuit, dispenses the analyte onto the packed column. After 12 minutes retention time the measuring results of the TCD and the FID are available. The evaluation of the chromatograms is based on calibration curves, which were measured using the following calibration gases:

- Methane: 2.5%, 50%, 100%
- Ethane: 0.85%, 1%, 100%
- Propane: 0.85%, 100%
- Nitrogen: 100%

The residual gases are in all cases nitrogen.

6.2 Results

Table 6.1 lists all gas samples that were investigated. The natural gas samples of the supplier Hamburger Energiewerke GmbH have been investigated at three different times. Due to the ambient pressure of the storage gas sample, it had to be prepared and diluted as described in 6.1.2 using the setup shown in Figure 6.5. PAS did not detect any propane in this sample and the GC result was “less than 1‰”.

TABLE 6.1: Analysis results.

Sample type	Date	PAS			GC		
		Methane	Ethane	Propane	Methane	Ethane	Propane
Natural gas	26th May 2023	86.11%	4.98%	0.92%	85.23%	4.70%	0.96%
	28th June 2023	85.03%	4.95%	0.67%	85.10%	4.96%	0.87%
	2nd August 2023	82.35%	4.60%	0.62%	84.33%	4.41%	0.77%
Storage gas	29th June 2023	6.79%	0.41%	-	6.78%	0.48%	< 0.1%

Figures 6.7 and 6.8 show the true and the predicted shares for methane and ethane exemplarily. The absolute root mean square errors (RMSE) for the methane, ethane and propane concentrations in Fig. 7a are 1.34%, 0.19% and 0.13%, respectively. The absolute RMSE for methane and ethane concentrations in Fig. 7b are 0.29% and 0.03%, respectively.

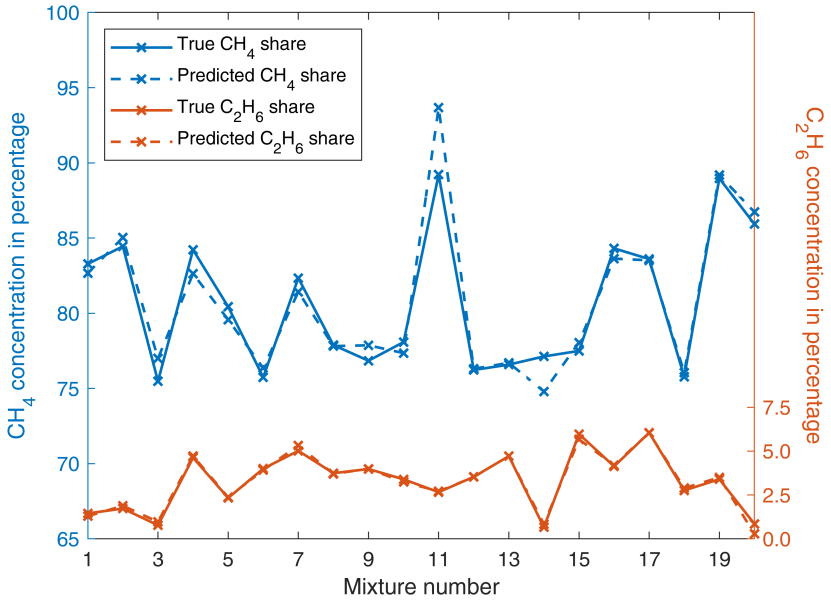

FIGURE 6.7: Results of the leave-one-out cross-validation of natural gas (propane is hidden for clarity).

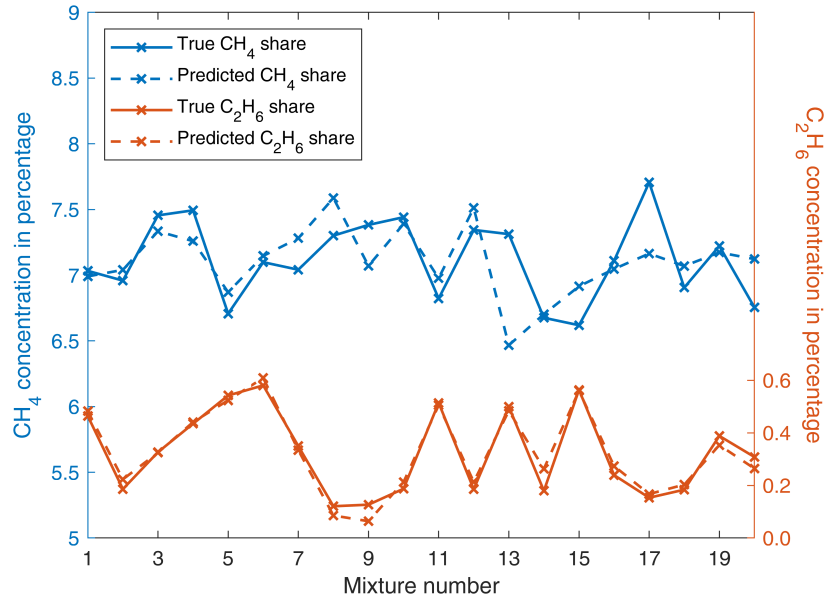

FIGURE 6.8: Results of the leave-one-out cross-validation of storage gas.

The number of training data sets significantly influences the absolute RMSE. Figure 8 illustrates this relationship.

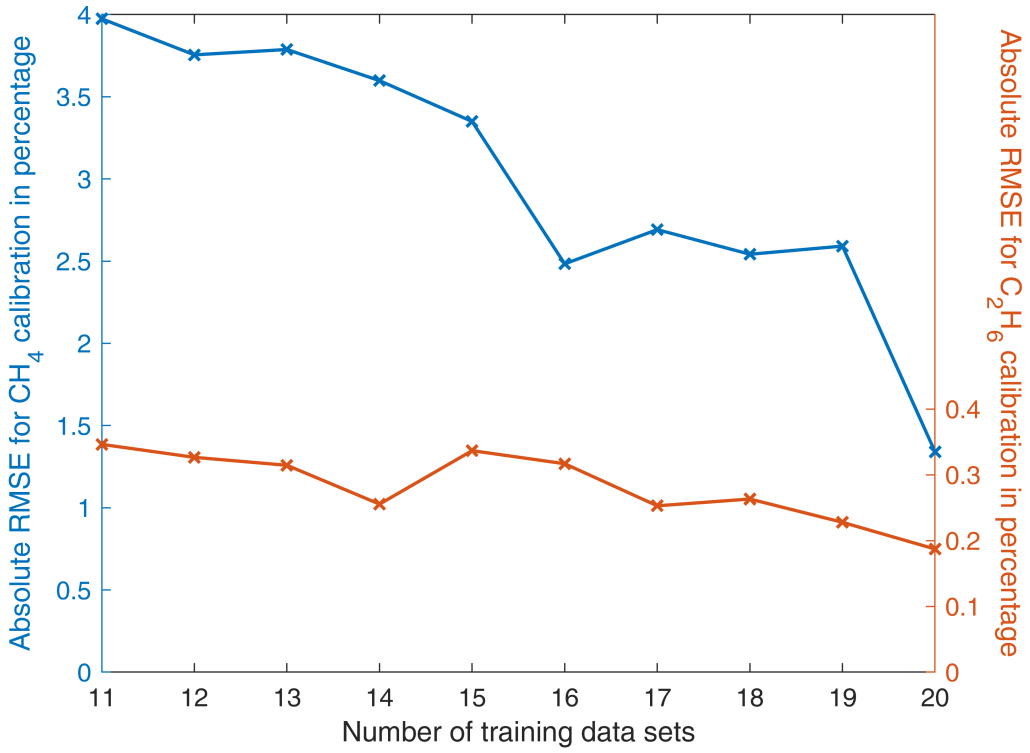

FIGURE 6.9: Absolute RMSE as function of the number of training data sets.

6.3 Discussion

Figure 6.6 shows an examplary photoacoustic spectrum. It does not perfectly correspond to the derivative of the absorption spectrum, due to the nonlinear spectral behavior of the injection-current modulation and the missing normalization regarding the laser output power.

As shown in Table 6.1, the PAS results are in good agreement with the GC results. If we consider that the GC exhibits a relative error of up to 2%, the agreement can be described as excellent.

As displayed in Figure 6.8, an increase of the number of training data sets leads to a significantly decreasing absolute RMSE. Notwithstanding only a relatively low number of 20 training data sets were used for this investigation, accurate results could be achieved. A further increase of the number of training data sets would further decrease the error.

The natural gas analysis on 28th June 2023 delivered a methane concentration of 85.03% (PAS) and 85.10% (GC), respectively (see Table 6.1). Both values do not agree with the 91.95% officially published by Gasnetz Hamburg GmbH (Hamburg, Germany) for this month (Gasnetz Hamburg GmbH, 2023). The true value is almost 7% smaller than the value used for invoicing.
In conclusion it can be stated that, photoacoustic spectroscopy in combination with PLSR is a suitable method for analyzing natural gas samples as well as storage gas samples in a wide dynamic range. Due to the short analysis time of approximately 12 seconds and the absence of any operating gases, the presented PAS-based sensor could be further developed into an alternative to GC that is attractive in terms of price and performance.

Chapter 7

Summary and Outlook

The overall goal of this research is the development of a measurement setup and procedure based on photoacoustic spectroscopy which is used to quantitatively analyze the composition of natural gas and the main methane isotopologues $^{13}CH_4$ and $^{12}CH_4$ of natural gas-like mixtures.

Natural gas is one of the most important energy sources of our time, and its composition provides information about its energy content and origin. The composition of the main methane isotopologues can be used to derive further information regarding the degree of maturity of the natural gas as well as to optimize the extraction technology.

There are a variety of methods for analyzing natural gas. Gas chromatography is considered the gold standard in natural gas analysis. This enables analyses from ppb to the percentage range per component of the natural gas, with deviations of less than 2%. The extension of a gas chromatograph by isotope ratio mass spectroscopy enables the detection of the $^{13}CH_4/^{12}CH_4$ isotopologue ratio. The main disadvantages are the need for at least 2 operating gases, laboratory conditions to produce reproducible results, continuous calibrations to compensate for detector drift and the lack of compactness of the gas chromatograph. In-situ measurements are therefore hardly possible. Furthermore, there are a number of spectroscopic methods, which are, however, also rarely suitable for field measurements due to construction-related reasons.

The choice of the optimum wavelength range in which the laser used should emit laser radiation is crucial for the success of spectroscopic measurements. Since the main alkanes of natural gas overlap spectrally at a large number of wavelength, it is hardly possible to determine the optimum wavelength range empirically. Therefore, a mathematical algorithm is presented in this

thesis, which enables the calculation of the optimal wavelength, based on the theoretical absorption spectra, for the detection of the main alkanes and the main methane isotopologues. For the latter, an average wavelength of 3320.7 nm is obtained.

Photoacoustic spectroscopy requires the modulation of laser radiation. To achieve precise results, the exact knowledge of the spectral behavior of the laser used is prerequisite. The modulation can be performed indirectly, e. g. with the aid of a "chopper", or directly by modulating the laser injection-current or the laser temperature. The direct modulation of the laser leads to maximum reproducibility of the measurements and at the same time poses a challenge, as there is still no commercially available measuring device to analyze the spectral behavior of an interband cascade laser modulated in the kHz range with high wavelength resolution.
For this reason, a Michelson interferometer-based method is presented in this thesis, which uses a reference wavelength, determined by transmission spectroscopy, to determine the absolute emitted wavelength as a function of the laser operating current with sawtooth modulation in the frequency range from 10 Hz to 30 kHz. It can be seen that the dynamic range with respect to the wavelength of the interband cascade laser used decreases with increasing modulation frequency.
The analysis of the spectral behavior of the analyzed interband cascade laser showed that it can be used directly modulated in photoacoustic spectroscopy and is therefore suitable for natural gas and methane main isotopologue analysis.

The analysis of the main methane isotopologues $^{13}CH_4$ and $^{12}CH_4$ poses a major challenge due to their strongly overlapping absorption spectra. Thus, an interband cascade laser is used to differentiate the two molecules. This laser emits single-mode with a spectral bandwidth of less than 3 MHz, which enables high-resolution spectroscopy and identification of the main methane isotopologue concentrations.
The main isotopologue mixture to be analyzed is located in a measuring cell in which an analog electret microphone is also integrated. The methane molecules are excited by the injection-current modulated interband cascade laser and the resulting photoacoustic signal is converted into an electrical signal by the microphone. A lock-in amplifier is used to demodulate the photoacoustic signal, resulting in a spectrum dependent on the laser operating

current. Spectra are measured for various main methane isotopologic mixtures, resulting in training data sets for the partial least squares regression model. With the help of this machine-learning-based model, spectra of unknown methane main isotopologue mixtures can be analyzed quantitatively with regard to the concentrations of the individual methane main isotopologues.
Artificial $^{13}CH_4/^{12}CH_4$ mixtures in nitrogen with concentrations of 25–70% and 0.28–3.00%, respectively, under laboratory conditions, are investigated. The absolute root-mean-square-errors for the predicted $^{12}CH_4$ and $^{13}CH_4$ concentrations are calculated to 3.08% and 0.29%, respectively.
The sensor thus appears to be suitable for analyzing natural gas-like methane main isotopologue concentrations.

Finally, the photoacoustic sensor is evaluated in natural gas analysis with the aim of analyzing real natural gas samples with regard to the main alkanes methane, ethane and propane. To this end, the sensor is calibrated using artificial mixtures similar to natural gas, which simulate various main alkane compositions.
The analysis of 3 natural gas samples from the Hamburg gas network shows that the sensor exhibits only minor deviations compared to the gas chromatography analysis carried out in parallel and is therefore able to analyze real natural gas samples in real time with a measurement time of approximately 12 seconds.
In addition, a method is presented that allows the preparation of natural gas samples under atmospheric pressure so that they are subsequently pressurized and can thus be analyzed with the photoacoustic sensor. This method is applied to a storage gas sample, which is then analyzed with the photoacoustic sensor described. It is shown that even in the single-digit percentage range of the main alkane concentrations, very good results are achieved in comparison to the gas chromatography analysis.

It has been shown that the sensor is able to analyze both methane main isotopologues and real natural gas samples with regard to the individual concentrations of their components with sufficient accuracy. One of the next steps would be to mobilize the sensor so that the extent to which it can be used for field measurements can be investigated.
Furthermore, a performance comparison using an equivalent quartz enhanced photoacoustic spectroscopy sensor would be useful to investigate whether

the use of a quartz tuning fork instead of an analog microphone would provide an advantage.

Chapter 8

Appendices

The published content used in this thesis is listed in the following.

photonics

MDPI

Communication

Interferometric Technique for the Spectral Characterization of High Frequency Current-Modulated Mid-Infrared Semiconductor Lasers

Marc-Simon Bahr [1,2,*] and Marcus Wolff [1]

[1] Heinrich Blasius Institute of Physical Technologies, Hamburg University of Applied Sciences, Berliner Tor 21, 20099 Hamburg, Germany; marcus.wolff@haw-hamburg.de
[2] School of Computing, Engineering and Physical Sciences, University of the West of Scotland, High Street, Paisley PA1 2BE, UK
* Correspondence: marc-simon.bahr@haw-hamburg.de

Abstract: We describe two methods, based on Michelson interferometery, that enable the determination of the absolute wavelength of current-modulated semiconductor lasers. By non-linear regression of the instantaneous frequency of the interference signal, the rate of change of the wavelength of the radiation can be inferred. Alternatively, the absolute wavelength can be directly calculated from the maxima and minima of the interference signal. In both cases a reference absorption line enables the determination of the absolute wavelength. Both methods offer respective advantages. The methods allow a highly resolved wavelength measurement under lower kilohertz range current-modulation with relatively little effort. As a result, we present the rates of wavelength change and absolute wavelengths exemplarily for a specific interband cascade laser. It is furthermore shown that the spectral dynamic range of the laser decreases with increasing modulation frequency.

Keywords: current modulation; interband cascade laser; michelson interferometer; high-resolution spectroscopy

Citation: Bahr, M.-S.; Wolff, M. Interferometric Technique for the Spectral Characterization of High Frequency Current-Modulated Mid-Infrared Semiconductor Lasers. *Photonics* **2021**, *8*, 443. https://doi.org/10.3390/photonics8100443

Received: 19 August 2021
Accepted: 9 October 2021
Published: 14 October 2021

1. Introduction

The exact knowledge of the emission wavelength is one of the fundamental parameters in laser spectroscopy. Several spectroscopic techniques such as photoacoustics require a modulation of the radiation as a matter of principle [1].

Semiconductor lasers can easily be modulated by variation of the operating current. In doing so amplitude as well as wavelength modulation are possible. However, assuming a simple, frequency-independent proportionality between wavelength and current, as it is observable in continuous wave (cw) operation, can lead to significant measurement errors [2]. The determination of the momentary wavelength becomes extraordinarily difficult if the semiconductor laser emitting in the mid-infrared (e.g., an interband cascade laser or ICL) is modulated with a higher frequency.

At present, different methods and measuring devices exist that enable the spectral characterization of semiconductor lasers such as ICLs [3]. However, all of them are primarily applicable for cw radiation. Often, prism or grating spectrometers are used as measuring instruments, which are based on diffraction and interference phenomena, respectively. A further method is the Fourier transform interferometer (FTIR), which is based on a Michelson interferometer and determines the emission spectrum by Fourier transform of the interferogram [4].

Another possibility is the "wavemeter" of BRISTOL Instruments, Inc. (Victor, New York, NY, USA). It measures the wavelength of a laser on the basis of a Michelson interferometer, provides accuracy in the ppm range and represents the state of the art for wavelength measurements in continuous wave operation [5–7].

If the laser is operated in current-modulation mode, there are only few possibilities. One approach determines the wavelength change as a function of the laser operating current ($d\lambda/dI$) [8]. The experimental setup is based on a Mach-Zehnder interferometer and the change in wavelength is calculated using a mathematical algorithm which is not further described. This method does not allow a determination of the absolute wavelength as a function of the current.

Another possibility for a fast wavelength measurement is a heterodyne (or super-heterodyne) Michelson interferometer. It differs from the homodyne interferometer in that a beat signal is analyzed that results from the superposition of the radiation to be analyzed and that of a second laser. This technique is particularly well suited if the phase of the beat signal is required [9–11].

A US patent from 2019 represents the latest research progress regarding the determination of the absolute wavelength of current-modulated semiconductor lasers. It is pointed out that, on the basis of an interferometer, the absolute wavelength of tunable lasers can be determined very precisely. The rudimentarily described method mentions the need for a reference wavelength, e.g., a gas absorption line [12].

To the best of our knowledge there is only one commercially available device for the determination of mid-infrared wavelengths in modulation mode. The "NLIR 2.0–5.0 µm spectrometer" of NLIR ApS (Farum, Denmark) is based on non-linear optics and transforms the laser radiation into the near-infrared range, which is subsequent analyzed using a diffraction grating and a CMOS sensor [13]. According to the manufacturer the maximum sampling rate of the instrument is 130 kHz. The spectral resolution of the NLIR is around 1.5 nm.

Due to the fact that the currently available methods for the spectral characterization of current-modulated semiconductor lasers, especially DFB interband cascade lasers, are not sufficient to achieve a high spectral resolution, new techniques are required.

2. Materials and Methods

In the following, two methods for determining the absolute wavelength of modulated semiconductor lasers, in this case interband cascade lasers, are described. Both are based on the same experimental setup and exhibit advantages and disadvantages due to the different signal processing.

2.1. Experimental Setup

Figure 1 shows the schematic experimental setup for measuring the laser wavelength as function of the current during modulation. It is based on a homodyne Michelson interferometer with silver mirrors and a CaF_2 beam splitter [14]. The difference between the two distances a and b is of great importance, because it determines the quality of the results. If a and b approach each other, the number of maxima and minima in the interference signal decreases, which is disadvantageous for the spectral characterization. Simultaneously, the signal-to-noise ratio (SNR) increases due to the decreasing distance to the detector. This has a positive effect on the evaluation. If one of the two paths becomes significantly larger than the other, the number of maxima and minima increases, however, the SNR decreases due to the longer distance to the detector. In order to achieve a good compromise between spectral resolution and SNR, the distances have to be empirically optimized.

The Thorlabs PDA07P2 employs an InAsSb detector and provides a bandwidth of 9 MHz. The ICL 1541, manufactured by nanoplus GmbH (Gerbrunn, Germany), was characterized with an average wavelength λ_0 of 3333 nm and a spectral linewidth of less than 20 MHz. The laser can be operated at temperatures between 15 and 27 degrees Celsius. Stimulated emission occurs with operating currents between 25 and 45 mA. The average optical output power is 5.5 mW. During cw operation it can be assumed that the wavelength is proportional to the current with $d\lambda/dI$ = 0.16 nm/mA. The ICL is driven by the Thorlabs TLD001 diode driver and its temperature is controlled by the Thorlabs temperature controller TTC001. The laser diode current can be accurately set to 10 µA with

a noise level < 3 µA rms. The ICL chip is installed in a TO66 housing including a Peltier element for temperature regulation and the temperature sensor. Within the scope of the technical possibilities, the laser wavelength is optimally stabilized. A 33220A function generator (Agilent, Santa Clara, CA, USA) is used to modulate the operating current of the diode driver.

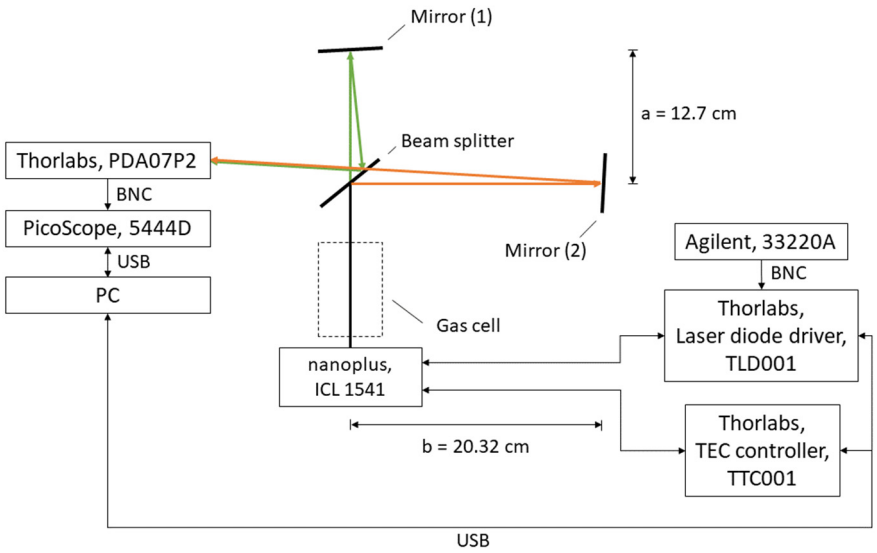

Figure 1. Experimental setup based on a Michelson interferometer.

The intensity detected by the detector is converted into a voltage signal which is sampled by a PicoScope 5444D (Pico Technology, Cambridgeshire, UK) with 16 bit resolution. The sampling rate is 62.5 MS/s. The sampled signal is then subjected to processing by means of MATLAB. After the signal is time sliced, Savitzky-Golay based filtering of the signal is performed to eliminate high frequency noise [15]. This optimizes the precision of the subsequent detection of the local maxima and minima in the interference signal. Subsequently, different mathematical equations and methods are applied according to the procedures described in Sections 2.2 and 2.3, respectively.

2.2. Non-Linear Regression

2.2.1. Spectral Characterization

The electric field (E-field) component of the ICL radiation at the location of the detector can be described as [16]:

$$E(t) = \hat{E}(t) \cdot e^{j(\omega t + \varphi_0)} \tag{1}$$

where ω is the instantaneous angular frequency of the E-field and φ_0 is the initial phase of the laser radiation. The stochastic phase noise of the laser radiation is neglected here, since it would only increase the complexity of the equation and does not add any value to the following calculations. $\hat{E}(t)$ corresponds to the amplitude and is time-dependent because the ICL is modulated.

One part of the laser beam is transmitted through the beam splitter and reflected by mirror (1). When it hits the detector, its E-Field equals:

$$E_1(t) = \hat{E}(t) \cdot e^{j(\omega t + \varphi_0)}. \tag{2}$$

The second part of the laser beam is reflected at the beam splitter, then reflected at mirror (2) and subsequently transmitted through the beam splitter. Due to the path difference $s_d = 2(b - a)$, it hits the detector delayed by a time t_d compared to $E_1(t)$:

$$t_d = \frac{2(b-a)}{c} = \frac{s_d}{c}, \tag{3}$$

where c corresponds to the speed of light. If this part of the laser beam hits the detector, the E-field component can be described with:

$$E_2(t) = E_1(t - t_d) = \hat{E}(t - t_d) \cdot e^{j(\omega(t-t_d)+\varphi_0)}. \tag{4}$$

If the laser current is modulated, the wavelength (angular frequency ω) changes continuously as a function of time. This results in the following relationships for the E-field components hitting the detector:

$$E_1(t) = \hat{E}(t) \cdot e^{j(\int_0^t \omega(\tau)d\tau+\varphi_0)}, \tag{5}$$

$$E_2(t) = \hat{E}(t - t_d) \cdot e^{j(\int_0^{t-t_d} \omega(\tau)d\tau+\varphi_0)}. \tag{6}$$

The integration of the angular frequency becomes necessary because it is not constant over time anymore.

If both partial beams hit the detector, the sum of both components equals:

$$E_S(t) = E_1(t) + E_2(t). \tag{7}$$

Since the detector only detects intensities, the relationship between the E-field components and the intensity must be applied [17]:

$$I(t) \propto |E_s(t)|^2. \tag{8}$$

Since the absolute value of the intensity is of no importance for the further considerations, the following results for the detector signal:

$$I(t) \propto \hat{E}^2(t) + \hat{E}^2(t - t_d) + 2\hat{E}(t) \cdot \hat{E}(t - t_d) \cdot \cos\left(\int_{t-t_d}^{t} \omega(\tau)d\tau\right). \tag{9}$$

Due to the extremely short interferometer delay time ($t_d < 1$ ns), it can be assumed that $E(t) \approx E(t - t_d)$, which simplifies Equation (9) to:

$$I(t) \propto 2\hat{E}^2(t) + 2\hat{E}^2(t) \cdot \cos\left(\int_{t-t_d}^{t} \omega(\tau)d\tau\right). \tag{10}$$

Therefore, the detector signal depends particularly on the interferometer delay time and corresponds theoretically to an oscillation between $4\hat{E}^2(t)$ and zero. The instantaneous angular frequency of the laser $\omega(t)$ can be derived from the phase $\varphi(t)$ of the detector signal. This is possible due to the elementary relationship between the angular frequency and the phase $\omega(t) = \frac{d\varphi(t)}{dt}$ [18]:

$$\omega_{If}(t) = \dot{\varphi}(t) = \frac{d}{dt}\left(\int_{t-t_d}^{t} \omega(\tau)d\tau\right), \tag{11}$$

where $\omega_{If}(t)$ corresponds to the angular frequency of the interferometer signal. Since the integration interval in Equation (11) corresponds to the delay time t_d, the infinitesimal value $\omega(\tau)$ can be considered approximately constant in the interval. Thus Equation (11) results in:

$$\omega_{If}(t) = \frac{d}{dt}\omega(t) \cdot t_d = 2\pi \cdot c \cdot t_d \cdot \frac{d}{dt}\frac{1}{\lambda(t)} = -\frac{2\pi \cdot c \cdot t_d}{\lambda^2(t)} \cdot \frac{d\lambda(t)}{dt}. \tag{12}$$

The square of the wavelength $\lambda^2(t)$ can be approximated by the square of the average wavelength λ_0^2 given in the data sheet of the respective semiconductor laser. Understandably, this does not apply to $\lambda(t)$ in the derivative. Resolved according to the wavelength

change as function of time and with the relationship $s_d = c \cdot t_d$ according to Equation (3), it follows that:

$$\frac{d\lambda(t)}{dt} = -\frac{f_{If}(t) \cdot \lambda_0^2}{c \cdot t_d} = -\frac{f_{If}(t) \cdot \lambda_0^2}{s_d}, \tag{13}$$

with the momentary frequency of the interference $f_{If}(t)$. The negative sign on the right side has no meaning for further calculations. Due to the symmetry of the cosine function, it is not possible to distinguish between positive and negative phases of the interferometer signal. The negative sign can therefore be omitted.

However, the wavelength change as function of the change in current is sought. The modulation of the current is, in this case, sawtooth-shaped with the rate of change k (units: $\frac{\mathrm{mA}}{\mathrm{s}}$):

$$\frac{dI(t)}{dt} = k. \tag{14}$$

Equation (14) solved for dt and inserted into Equation (13) delivers (if the sign is omitted):

$$\frac{d\lambda(I)}{dI} = \frac{f_{If}(I) \cdot \lambda_0^2}{s_d \cdot k}. \tag{15}$$

The wavelength as a function of the operating current can be determined from the differential quotient by means of integration if an absolute wavelength is known as reference point:

$$\lambda(I_1) = \int_{I_0}^{I_1} \frac{d\lambda(I)}{dI} dI + \lambda(I_0). \tag{16}$$

The reference wavelength $\lambda(I_0)$ can, for instance, be determined experimentally. If the modulated laser beam passes a cell filled with a gas that shows a strong and distinct absorption line in the expected wavelength range, the transmission of the interference signal provides the reference wavelength [19].

2.2.2. Error Estimation

The wavelength as function of current calculated according to Equation (16) is subject to deviations due to measurement errors and approximations.

Equation (15) inserted into Equation (16) results in:

$$\lambda(I_1) = \frac{\lambda_0^2}{s_d \cdot k} \int_{I_0}^{I_1} f(I) dI + \lambda(I_0). \tag{17}$$

The coefficients of the regression function $f(I)$ can be determined applying a polynomial regression of second (or larger) degree using the evaluated frequency values of the interference signal. After integration, a closed analytical expression is obtained, depending on metrologically determined quantities, which are subject to error tolerances. The maximum possible error can then be calculated by the sum of the following components:

$$\Delta\lambda(I_1)_{\lambda_0} = \frac{2\lambda_0}{s_d \cdot k} \left(\frac{a_1}{3} I_1^3 + \frac{a_2}{2} I_1^2 + a_3 I_1 - \frac{a_1}{3} I_0^3 - \frac{a_2}{2} I_0^2 - a_3 I_0 \right) \cdot \Delta\lambda_0, \tag{18}$$

$$\Delta\lambda(I_1)_{s_d} = \frac{\lambda_0^2}{s_d^2 \cdot k} \left(\frac{a_1}{3} I_1^3 + \frac{a_2}{2} I_1^2 + a_3 I_1 - \frac{a_1}{3} I_0^3 - \frac{a_2}{2} I_0^2 - a_3 I_0 \right) \cdot \Delta s_d \text{ and} \tag{19}$$

$$\Delta\lambda(I_1)_{\lambda(I_0)} = \Delta\lambda(I_0), \tag{20}$$

where $a_{1\ldots3}$ stand for the coefficients of the regression function and $\Delta\lambda_0$, Δs_d and $\Delta\lambda(I_0)$ for the absolute errors of the individual variables. The influence of the integration according to Equation (17) on the maximum error can be estimated by the Riemann sum [20]. It includes the standard deviation of the instantaneous frequency $f(I)$, which results from the non-linear regression.

An additional error is caused by approximations. One of the effects is the standard deviation σ_{If} of the interference signal which describes the distribution of the instantaneous frequencies around the regression function. For its share of the maximum wavelength error $\Delta\lambda_{\sigma If}$ applies:

$$\Delta\lambda_{\sigma If} = \frac{\lambda_0^2}{s_d \cdot k} \cdot \pm \sigma_{If} \cdot (I_1 - I_0). \tag{21}$$

The result must be added to that from Equations (18)–(20).

2.3. Direct Evaluation of Fringes

2.3.1. Spectral Characterization

The equations presented in Section 2.2 are also valid for the method labeled "direct evaluation of fringes". The cosine occurring in the interference signal, according to Equation (10), corresponds to local maxima and minima, hereafter referred to as fringes, due to constructive and destructive interference.

The conditions for constructive and destructive interference depend mainly on the path difference of the Michelson interferometer whereas:

$$s_d = n \cdot \lambda, \tag{22}$$

$$s_d = (2n+1) \cdot \frac{\lambda}{2}, \tag{23}$$

respectively, with $n \in \mathbb{Z}$ [21]. By means of a reference wavelength based on an absorption line in the transmission spectrum, the absolute wavelengths of the individual fringes according to Equations (22) and (23) can be calculated: After n of the local extremum nearest to the reference wavelength has been determined, all other extrema can be assigned by iterating n. Subsequently, the wavelengths in between the individual extreme points are calculated by non-linear regression.

2.3.2. Error Estimation

The accuracy of the results of this method depends, besides the exactness of the reference wavelength, mainly on the accuracy of the path difference s_d. Its influence on the maximum error of the frequency of fringes f_f results in:

$$\Delta f_f = n \cdot \frac{c}{s_d^2} \cdot \Delta s_d, \tag{24}$$

$$\Delta f_f = \frac{2n+1}{2} \cdot \frac{c}{s_d^2} \cdot \Delta s_d, \tag{25}$$

for constructive and destructive interference, respectively, where Δs_d corresponds to the maximum error of s_d and the natural number n to the number of fringes which lie to the left or right of the reference wavelength. Due to the linear relationship between Δf_f and n, it is advantageous to base the calculation on the frequency and convert it subsequently to wavelength.

3. Results

The two methods were tested using the nanoplus ICL 1541. For the test a sawtooth modulation between 25 and 45 mA was applied. Measurements were conducted at 15, 21 and 27 °C in order to cover the entire dynamic range. The gas used for the determination of the reference wavelength is ethane with a purity of 99.999% and 99% nitrogen content. Measurements were taken at a gas temperature of approximately 22 °C and a pressure of 1000 mbar.

Figure 2 shows exemplary results obtained by the two methods.

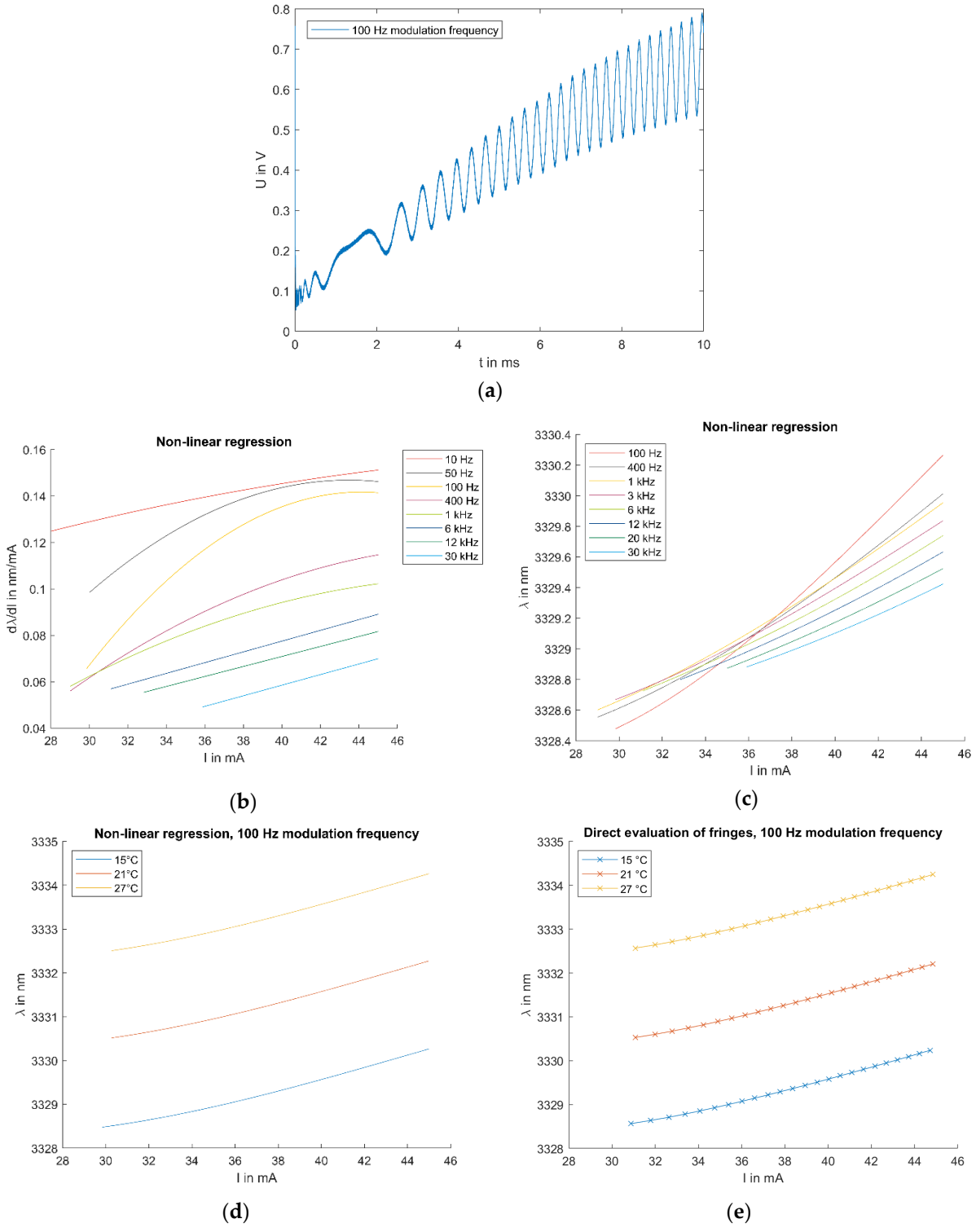

Figure 2. Measurements with the nanoplus ICL 1541 at sawtooth modulation: (**a**) Exemplary interference signal at 100 Hz modulation frequency and 15 °C laser temperature; (**b**) Change of wavelength as function of operating current for different modulation frequencies based on the non-linear regression method at 15 °C laser temperature; (**c**) Absolute wavelength as function of operating current for different modulation frequencies based on the non-linear regression method at 15 °C laser temperature; (**d**) Absolute wavelength as function of the operating current for three different laser temperatures based on the non-linear regression method at 100 Hz modulation frequency; (**e**) Absolute wavelength as function of the operating current for three different laser temperatures based on the direct evaluation of fringes at 100 Hz modulation frequency; the crosses mark the calculation points.

The measuring ranges of the two methods differ, because discontinuities in the interference signal are bridged in the non-linear regression method. They can be extracted directly from Figure 2d and e, respectively. Table 1 lists the measuring ranges as well as the wavelength errors according to Equations (18)–(21).

Table 1. Measuring ranges and wavelength errors of the two methods.

Method	Measuring Range	Wavelength Error
Non-linear Regression method	30–45 mA	$\Delta\lambda = \pm 0.12$ nm
Direct evaluation of fringes	31–45 mA	$\Delta\lambda = \pm 0.030$ nm

Table 2 presents the spectral range of the ICL as function of the modulation frequency.

Table 2. Spectral range of nanoplus ICL 1541.

Modulation Frequency (kHz)	Wavelength Range (nm)	$\Delta\lambda$ (nm)	$\Delta\lambda$ (Relative to cw)
cw	3327.52–3330.57	3.05	1.00
0.1	3328.48–3330.27	1.79	0.59
0.4	3328.55–3330.01	1.46	0.48
1	3328.60–3329.95	1.35	0.44
3	3328.67–3329.84	1.17	0.38
6	3328.73–3329.74	1.01	0.33
12	3328.80–3329.63	0.83	0.27
20	3328.87–3329.53	0.66	0.22
30	3328.88–3329.42	0.54	0.18

Figure 3 shows the spectral dynamic range $\Delta\lambda$ (relative to cw) as a function of frequency on the basis of the values in Table 2. According to the shape of the graph in Figure 3, it is reasonable to assume that the relationship shown corresponds to the natural logarithm.

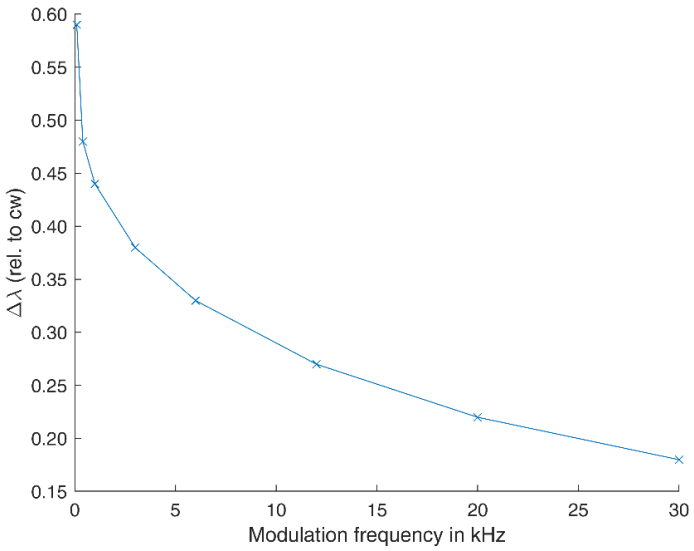

Figure 3. Spectral dynamic range $\Delta\lambda$ (relative to cw) as function of modulation frequency.

4. Discussion

4.1. Advantages and Disadvantages of Both Methods

A direct comparison of the methods in Section 2 shows that the direct evaluation of fringes requires fewer physical quantities for the calculation of the absolute wavelength and less computational effort compared to the non-linear regression method. This results in an overall higher precision.

The "non-linear regression method" on the other hand enables a compensation of discontinuities in the interference signal and, therefore, a larger measuring range compared to the direct evaluation of the fringes.

4.2. Explanatory Approach

Due to the lack of spectrometric tools, the spectral performance of mid-infrared semiconductor lasers under modulation has not yet been systematically investigated. The fact that the spectral dynamic range (i.e., the spectral modulation depth) decreases with increasing modulation frequency, as shown in Table 2 and Figure 3, was new even to the laser manufacturer. There is also no theoretical approach with which these measurement results could be compared.

However, the emission wavelength of a semiconductor laser is primarily determined by the geometric dimensions and the refractive index of the semiconductor material, and both parameters are significantly influenced by the laser temperature and thus indirectly by the injection current. A plausible explanation could therefore be a frequency-dependent temperature distribution of the semiconductor laser material. As the modulation frequency increases, there is less time available for establishing a thermal equilibrium. A changing frequency would therefore lead to a changing temperature distribution or the occurrence of (additional) inhomogeneities. Effects on the spectral emission are to be expected [22].

5. Conclusions

Figure 2a does not perfectly correspond to the mathematical description given by Equation (10). From the equation it would be expected that mutual cancellation of the DC and AC components and adding occur alternately. However, this is not observable because on the one hand Equation (10) is based on several approximations and on the other hand the alignment of the individual partial beams in the Michelson interferometer is not perfect.

An analysis of the results presented in Figure 2d,e shows that the wavelength difference between the two methods is only of the order of a few hundredths of a nanometer. Figure 2b,c demonstrate that, with increasing modulation frequency, the wavelength change as function of operating current decreases. This limits the spectral range of the ICL which is particularly relevant for wavelength modulation.

The spectral tuning characteristics of the modulated laser $d\lambda(I)/dI$ (Figure 2b) and $\lambda(I)$ (Figure 2c–e) can be approximated by quadratic polynomials and cubic polynomials, respectively. Compared to cw operation, the ICL thus shows a clearly nonlinear spectral behavior.

In cw operation, the tuning coefficient $d\lambda/dI$ for the nanoplus ICL 1541 equals approximately 0.16 $\frac{\text{nm}}{\text{mA}}$. Figure 2b shows that with decreasing modulation frequencies the individual curves approach this constant value.

The direct evaluation of fringes is a factor of four more precise than the non-linear regression method, as fewer error-prone variables are included. However, the accuracy of both methods strongly depends on the precision of the reference wavelength derived from the transmission spectrum. An advantage of the non-linear regression method over the direct evaluation of fringes is a larger measurement range.

Compared to the state of art, both methods achieve a significantly higher resolution, which does additionally have the potential to be optimized by adjusting the path length difference of the Michelson interferometer.

A heterodyne (or super-heterodyne) interferometer would not provide advantages over the applied homodyne setup, especially with regard to spectral resolution. A significant disadvantage represents the need of a second often frequency-stabilized laser.

In conclusion, it should be mentioned that both methods can be adapted to other types of modulation (e.g., sinusoidal) and applied for the analysis of spectra recorded by wavelength modulation spectroscopy [23].

Author Contributions: Writing—original draft preparations: M.-S.B.; writing—review and editing: M.W. Both authors have read and agreed to the published version of the manuscript.

Funding: This research was funded by Federal Ministry for the Environment, Nature Conservation and Nuclear Safety, grant number 67KI2075.

Data Availability Statement: Not applicable.

Acknowledgments: We would like to thank Alain Loh. He gave the initial suggestion to measure the wavelength by means of a Michelson interferometer.

Conflicts of Interest: The authors declare no conflict of interest.

References

1. Besson, J.-P.; Schilt, S.; Thévenaz, L. Multi-gas sensing based on photoacoustic spectroscopy using tunable laser diodes. *Spectrochim. Acta Part A Mol. Biomol. Spectrosc.* **2005**, *60*, 3449–3456. [CrossRef] [PubMed]
2. Demtröder, W. *Laserspektroskopie: Grundlagen und Techniken*; Springer: Berlin/Heidelberg, Germany, 2011.
3. Meyer, J.R.; Bewley, W.W.; Canedy, C.L.; Kim, C.S.; Kim, M.K.C.D.; Merritt, C.D.; Vurgaftman, I. The Interband Cascade Laser. *Photonics* **2020**, *7*, 75. [CrossRef]
4. Smith, B.C. *Fundamentals of Fourier Transform Infrared Spectroscopy*; CRC Press: Boca Raton, FL, USA, 2011. [CrossRef]
5. Available online: https://www.bristol-inst.com/bristol-instruments-products/wavelength-meters-scientific (accessed on 14 August 2021).
6. Bristol Instruments, Inc. Optical Wavelength Meter 828 Series Datasheet. 2020. Available online: https://www.bristol-inst.com/wp-content/uploads/2020/01/Bristol-828-Series-Optical-Wavelength-Meter-Specifications.pdf (accessed on 22 September 2021).
7. Veracious Statistics Research. *Global Laser Wavelength Meters Research Report 2021*; Professional Edition; Veracious Statistics Research: New Delhi, India, 2021. Available online: https://vstatisticsresearch.com/global-laser-wavelength-meters-market (accessed on 22 September 2021).
8. Du, Z.; Luo, G.; An, Y.; Li, J. Dynamic spectral characteristics measurement of DFB interband cascade laser under injection current tuning. *Appl. Phys. Lett.* **2016**, *109*, 011903. [CrossRef]
9. Schuldt, T.; Kraus, H.-J.; Weise, D.; Braxmaier, C.; Peters, A.; Johann, U. A heterodyne interferometer for high resolution translation and tilt measurement as optical readout for the LISA inertial sensor. In Proceedings of the International Conference on Space Optics 2006—CSO 2006, Noordwijk, The Netherlands, 27–30 June 2006. [CrossRef]
10. Olyaee, S.; Yoon, T.; Hamedi, S. Jones matrix analysis of frequency mixing error in three-longitudinal-mode laser heterodyne interferometer. *IET Optoelectron.* **2009**, *3*, 215–224. [CrossRef]
11. Dändliker, R.; Thalmann, R.; Prongué, D. Two-wavelength laser interferometry using superheterodyne detection. *Opt. Lett.* **1988**, *13*, 339–341. [CrossRef] [PubMed]
12. Seeley, R.; Froggatt, M.E. High Precision Wavelength Measurement and Control of a Tunable Laser. U.S. Patent 10,502,632 B2, 10 December 2019.
13. Available online: https://nlir.com/2-0-5-0-%c2%b5m-spectrometer (accessed on 14 August 2021).
14. Steel, W.H. *Interferometry*; Cambridge University Press: Cambridge, UK, 1983.
15. Press, W.; Teukolsky, S.A. Savitzky-Golay Smoothing Filters. *Comput. Phys.* **1990**, *4*, 669. [CrossRef]
16. Peatross, J.; Ware, M.J. *Physics of Light and Optics (Black & White)*; Brigham Young University, Department of Physics: Provo, UT, USA, 2015.
17. Kull, H. Back Matter. In *Laserphysik*; Oldenbourg Wissenschaftsverlag: Munich, Germany, 2011. [CrossRef]
18. Giancoli, D.C. *Physics for Scientists & Engineers with Modern Physics*; Pearson: London, UK, 2013.
19. Stewart, G. *Laser and Fiber Optic Gas Absorption Spectroscopy*; Cambridge University Press: Cambridge, UK, 2021. [CrossRef]
20. McGregor, C.; Nimmo, J.; Stothers, W. *Fundamentals of University Mathematics*; Elsevier: Amsterdam, The Netherlands, 2010. [CrossRef]
21. Booth, G.; Brodie, D. *As Physics Study Guide*; HarperCollins Publishers Limited: London, UK, 2008.
22. Zeller, W.; Naehle, L.; Fuchs, P.; Gerschuetz, F.; Hildebrandt, L.; Koeth, J. DFB Lasers Between 760 nm and 16 μm for Sensing Applications. *Sensors* **2010**, *10*, 2492–2510. [CrossRef] [PubMed]
23. Viveiros, D.; Ribeiro, J.; Flores, D.; Ferreira, J.; Frazão, O.; Santos, J.L.; Baptista, J.M. Gas sensing using wavelength modulation spectroscopy. In Proceedings of the Second International Conference on Applications of Optics and Photonics, Aveiro, Portugal, 26–30 May 2014.

Journal of Quantitative Spectroscopy & Radiative Transfer 286 (2022) 108216

Contents lists available at ScienceDirect

Journal of Quantitative Spectroscopy & Radiative Transfer

journal homepage: www.elsevier.com/locate/jqsrt

Determining the most suitable spectral range for TDLS – a quantitative approach

Marc-Simon Bahr[a,b,*], Bernd Baumann[a], Marcus Wolff[a]

[a] Heinrich Blasius Institute of Physical Technologies, Hamburg University of Applied Sciences, Berliner Tor 21, Hamburg 20099, Germany
[b] School of Computing, Engineering and Physical Sciences, University of the West of Scotland, High Street, Paisley PA1 2BE, UK

ARTICLE INFO

Article history:
Received 29 March 2022
Revised 12 April 2022
Accepted 12 April 2022
Available online 14 April 2022

Keywords:
Spectroscopy
Gas analysis
Detection sensitivity
Selectivity
Specificity
Semiconductor laser
Tunable diode laser

ABSTRACT

We present a mathematical method which allows determination of an optimal spectral range for gas mixture analysis based on theoretical absorption spectra. The resulting center wavelength is particularly suited for tunable diode laser spectroscopy (TDLS). The procedure contains several steps of numerical calculations which can easily be implemented in almost any programming language. We apply our method to three exemplary mixtures of hydrocarbons and present and validate the individual results.

1. Introduction

Optical spectroscopy is nowadays a well-established method for the analysis of gaseous mixtures. As soon as a high spectral resolution is required, spectrometers usually apply lasers as radiation sources [1–3]. In order to be able to probe different absorption features with a single laser, it is advantageous if its emission wavelength can be varied. Therefore, semiconductor lasers are predestined for this task, because they can be spectrally tuned via their operating temperature and current. The tuning range of distributed feedback interband cascade lasers is, for example, of the order of 10 nm at constant laser temperature with an emission linewidth in the single-digit megahertz range [4–7].

When designing a laser spectrometer, the definition of the laser's emission wavelength or, if tunable, its spectral range is crucial for its potential applications. As a matter of course, all the components of interest should exhibit absorption within the range. Furthermore, it is desirable that the absorption strengths of all components are high in order to achieve high detection sensitivity. Simultaneously, interferences of the absorbing compounds should be excluded to the greatest possible extent in pursuance of avoiding metrological ambiguity and, thus, reach high detection selectivity [1,2].

The identification of the optimal spectral range for a certain application, i.e. for the analysis of a certain mixture of gases, is not trivial. In practice it is usually an educated guess based on the known spectra [2,8,9]. The spectra evaluation, i.e. the determination of the concentrations of the individual components, is then typically carried out using a multivariate calibration such as partial least squares regression. However, the quality of the results, especially the selectivity, strongly depends on the selected wavelength range and the selection becomes increasingly difficult if the single spectra strongly overlap, and even more so if the single components are very similar and their spectra differ only slightly.

In the following we present, to the best of our knowledge, the first quantitative method to determine a well suited spectral range for sensitive and selective gas analysis. The procedure is customized for lasers of a certain tuning range, such as semiconductor lasers, and delivers its optimal center wavelength. The following section describes the mathematical procedure. After that we present exemplary application results.

2. Mathematical procedure

For the application of the method, knowledge of the absorption spectra of all gaseous components in the mixture is required. The

* Corresponding author at: Heinrich Blasius Institute of Physical Technologies, Hamburg University of Applied Sciences, Berliner Tor 21, Hamburg 20099, Germany.
E-mail address: marc-simon.bahr@haw-hamburg.de (M.-S. Bahr).

https://doi.org/10.1016/j.jqsrt.2022.108216

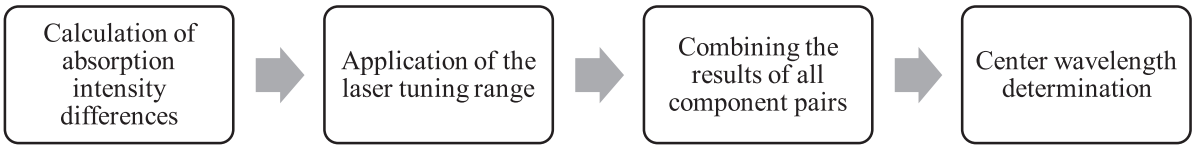

Fig. 1. Flowchart of the mathematical procedure.

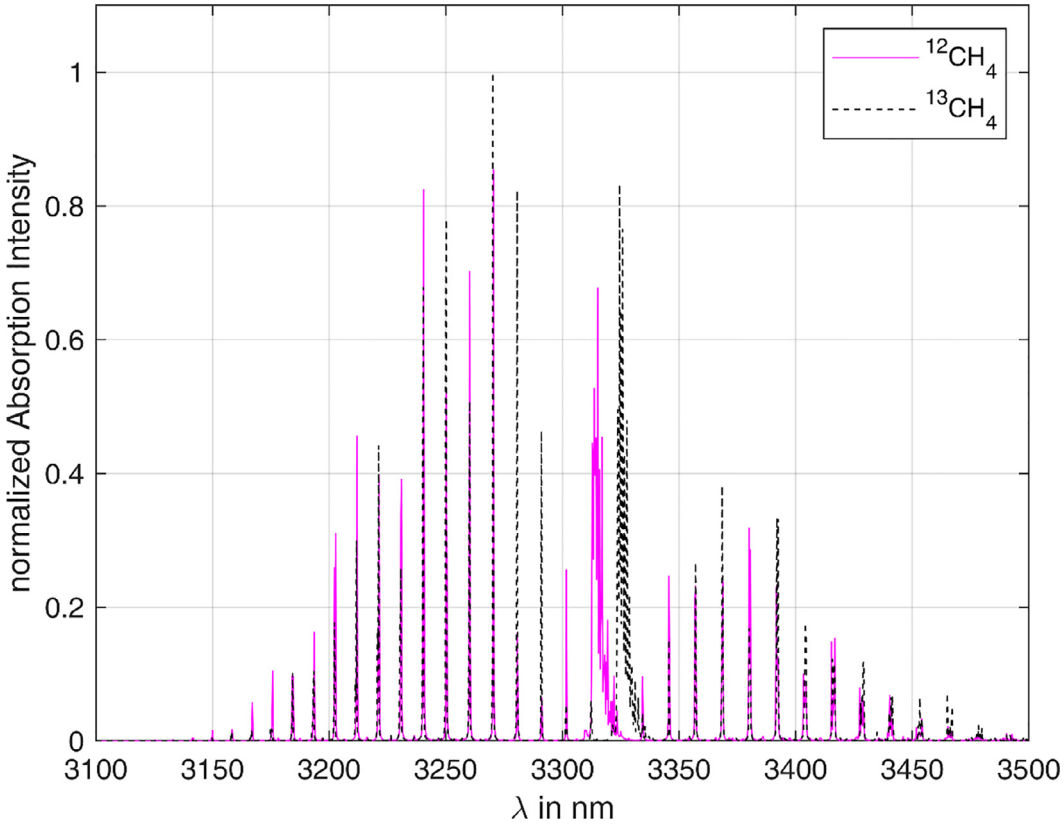

Fig. 2. Absorption spectra of $^{12}CH_4$ and $^{13}CH_4$ [20].

spectra can be measured beforehand, e.g. with a Fourier Interferometer, or extracted from databases such as HITRAN [10], GEISA [11], JPL [12] or NIST [13]. The flow chart of the method is shown in Fig. 1. The individual steps are explained in the following subsections.

2.1. Calculation of absorption intensity differences

In order to measure the individual gas components selectively or with least interference, it is necessary to identify the wavelengths at which the absorption spectra maximally differ from one another [14]. To find these spectral regions, all spectra are normalized to 1. A total number n of gases (spectra) results in:

$$\binom{n}{2} = \frac{n!}{2 \cdot (n-2)!} \tag{1}$$

dyads of spectra [15]. The individual absorption intensities of each gas $S(\lambda)$ are then used to calculate the intensity differences for each pair of gases (i and j) as function of the wavelength λ:

$$\Delta S_{ij}(\lambda) = S_i(\lambda) - S_j(\lambda). \tag{2}$$

2.2. Application of the laser tuning range

Semiconductor lasers exhibit a limited spectral tuning range. In the case of an interband cascade laser the tuning range $\Delta\lambda$ is typically of the order of 10 nm [4–7]. This has to be considered for the determination of best suited spectral range. The influence is represented by a sliding integral (Q-function) of the individual differences:

$$Q_{ij}(\lambda) = \int_{\lambda-\frac{\Delta\lambda}{2}}^{\lambda+\frac{\Delta\lambda}{2}} \left|\Delta S_{ij}(\lambda')\right| d\lambda'. \tag{3}$$

$Q_{ij}(\lambda)$ represents a measure of the spectral deviation of the species i and j in the wavelength range from $(\lambda - \frac{\Delta\lambda}{2})$ to $(\lambda + \frac{\Delta\lambda}{2})$. Due to the dependence of the integral limits on the wavelength, the integral acts like a window function. This window is sliding over the entire spectral range. Thus, the integral can also be described as a sliding integral.

Differences $\Delta S_{ij}(\lambda)$ of components with weak absorption can lead to inaccurate results in the following steps and, therefore, need to be suppressed. In order to do this, an auxiliary value D_{ij} is defined:

$$D_{ij} = \int_{\lambda_0}^{\lambda_1} \left|\Delta S_{ij}(\lambda)\right| d\lambda. \tag{4}$$

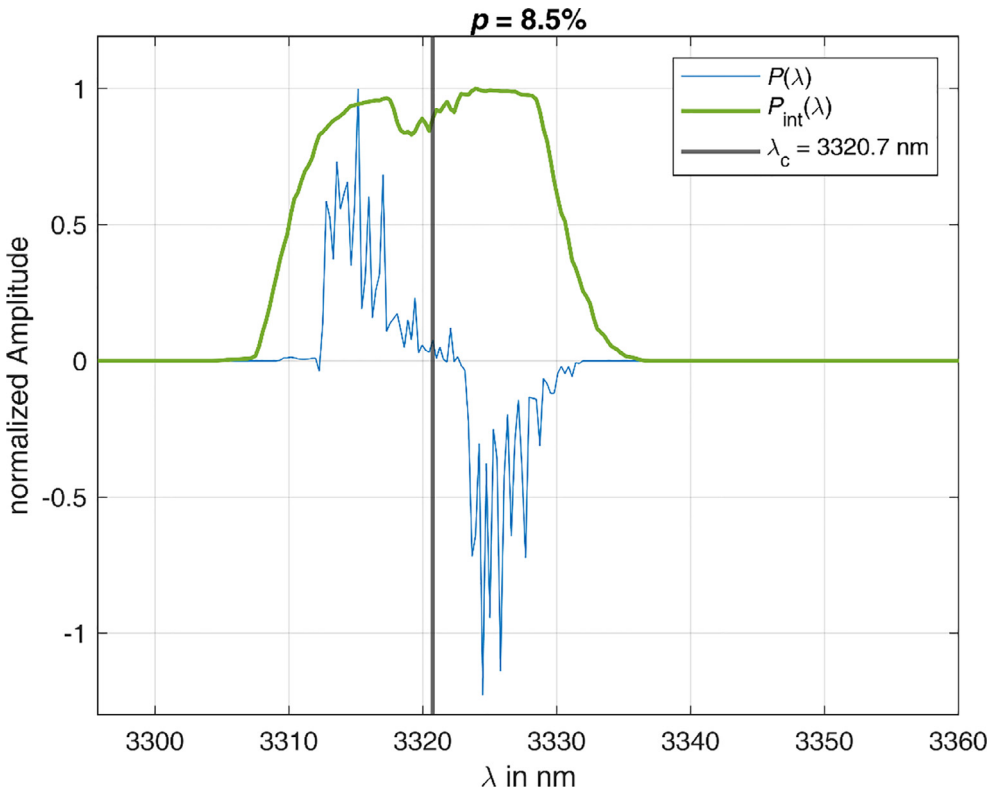

Fig. 3. Evaluation of the mixture $^{12}CH_4$ and $^{13}CH_4$, all quantities are normalized to "one".

Here, λ_0 and λ_1 are the lower and the upper boundary of the wavelength range under evaluation. Subsequently, a parameter $0 < p \ll 1$ has to be determined empirically, which is related to the threshold values of the individual Q-functions:

$$Q_{ij,th} = p \cdot D_{ij}. \tag{5}$$

The threshold values are needed to obtain an unambiguous result for the optimal laser wavelength. The parameter p is chosen optimally if Eq. (9) provides only a single range – the absolute maximum. $Q_{ij,th}$ is applied to $Q_{ij}(\lambda)$ according to:

$$\tilde{Q}_{ij}(\lambda) = \begin{cases} Q_{ij}(\lambda), & if\ Q_{ij}(\lambda) > Q_{ij,th} \\ 0, & else \end{cases}. \tag{6}$$

In a next step the Q-functions are multiplied by the difference spectra:

$$\Delta S_{ij,Q}(\lambda) = \Delta S_{ij}(\lambda) \cdot \tilde{Q}_{ij}(\lambda). \tag{7}$$

$\Delta S_{ij,Q}(\lambda)$ can be considered to be the difference spectrum for the gas pair i and j filtered by the Q-functions.

2.3. Combining the results of all component pairs

The "filtered" difference $\Delta S_{ij,Q}(\lambda)$ is large for wavelength regions, in which the spectra of a certain gas pair differs and, at the same time, absorption is strong. In order to consider the contribution of all possible gas pairs, all filtered differences are multiplied:

$$P(\lambda) = \prod_{i,j=1}^{n} \Delta S_{ij,Q}(\lambda), \quad \text{where } i < j. \tag{8}$$

The product $P(\lambda)$ is large if the previous conditions are satisfied for all gas component dyads. For absorption-weak wavelengths or wavelengths at which the spectra of the species do not differ significantly, the product $P(\lambda)$ is small. Thus, wavelength ranges with large values of $P(\lambda)$ mark the regions preferable for a sensitive and selective measurement. In order to consider the limited tuning range of semiconductor lasers an integral parameter equivalent to Eq. (3) is introduced:

$$P_{int}(\lambda) = \int_{\lambda - \frac{\Delta\lambda}{2}}^{\lambda + \frac{\Delta\lambda}{2}} \left| P(\lambda') \right| d\lambda'. \tag{9}$$

2.4. Center wavelength determination

The wavelength region around the maximum of $P_{int}(\lambda)$ indicates the spectral range in which the center wavelength of the semiconductor laser should ideally be located. We chose the median of P_{int} as center wavelength since it considers all values of P_{int} and is therefore "well-balanced".

In general, the median m of a function $f(x)$ is defined as [16]:

$$\int_{-\infty}^{m} f(x)dx = \frac{1}{2} \int_{-\infty}^{+\infty} f(x)dx. \tag{10}$$

The application of this definition leads to the optimal center wavelength λ_c of the laser:

$$\int_{\lambda_0}^{\lambda_c} P_{int}(\lambda)d\lambda = \frac{1}{2} \int_{\lambda_0}^{\lambda_1} P_{int}(\lambda)d\lambda. \tag{11}$$

With the aid of software like MATLAB [17] it is easy to extract λ_c from this equation.

3. Exemplary results

The mathematical procedure described above was programed in MATLAB and applied to assumptive gas mixtures. The absorption spectra of the single components were measured beforehand or extracted from the HITRAN database, respectively [18–20].

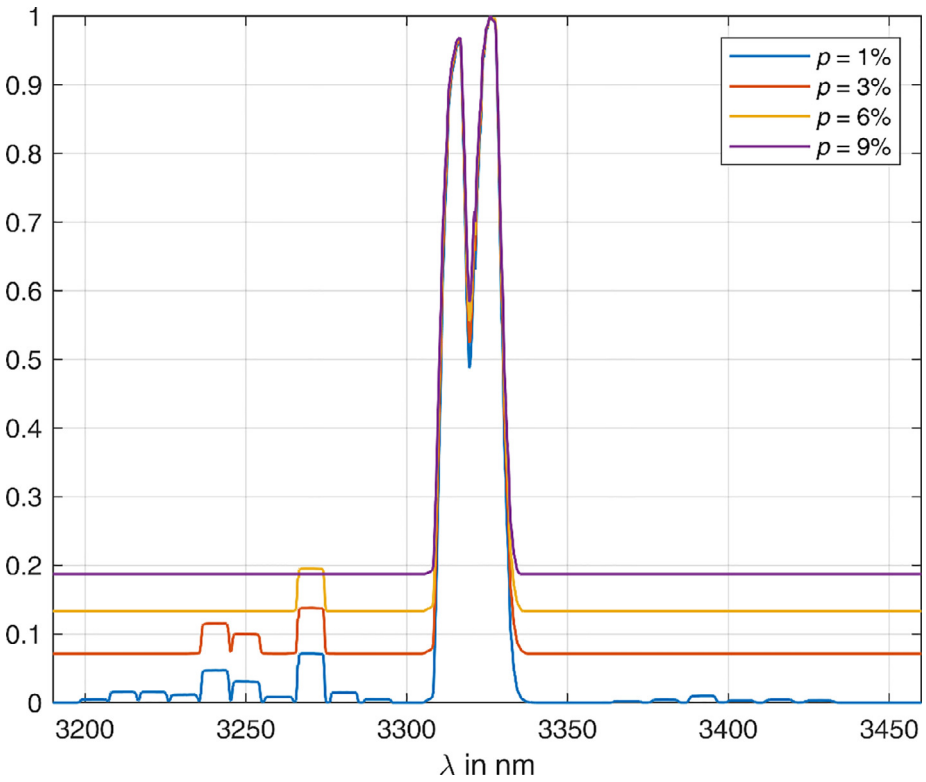

Fig. 4. Normalized $P_{\text{int}}(\lambda)$ of the mixture $^{12}CH_4$ and $^{13}CH_4$ for different values of p.

The algorithm was tested on combinations of gaseous, i.e. short-chained, hydrocarbons. Their strongest absorption is associated with the fundamental vibrations and occurs in the mid-infrared wavelength region, typically between 3 and 4 µm [21]. The lower and the upper boundary of the wavelength range under evaluation (λ_0 and λ_1) are 3000 nm and 3600 nm, respectively. Since the absorption spectra strongly overlap, it is often not possible to visually identify the optimal spectral range for the analysis.

3.1. Mixture of $^{12}CH_4$ and $^{13}CH_4$

In a first test, we investigated a mixture of the two main isotopologues of methane, $^{12}CH_4$ and $^{13}CH_4$. Fig. 2 shows both absorption spectra normalized to one. The graph of the $^{12}CH_4$ isotopologue does not reach intensity "one" because downsampling had to be performed after normalization so that the described computational operations can be applied to both isotopologues.

The two gases were selected because the spectral positions of the single rotational lines in the respective P- and R-branch are almost identical, but the positions of the Q-branches clearly differ. The $^{12}CH_4$ Q-branch is approximately located between 3310 and 3320 nm; the $^{13}CH_4$ one between 3320 and 3330 nm. Since the Q-branches additionally exhibit relatively high absorption strength, it would be expected that the laser of a perfectly suited spectrometer (tunability: 10 nm) covers a large part of these regions.

Because this mixture contains only two gases, the measure of the spectral deviation filtered with the Q-function, $\Delta S_{ij,Q}(\lambda)$, equals the product parameter $P(\lambda)$ according to Eq. (8) which is displayed in Fig. 3. $P_{int}(\lambda)$, the integral of $P(\lambda)$ over the 10 nm laser tuning range according to Eq. (9), is shown as well.

Fig. 3 shows $P_{int}(\lambda)$ for $p = 8.5\%$ on the larger scale whereas the dark grey vertical line represents its median which corresponds to the optimal center wavelength of the laser according to Eq. (11). The laser exhibits a center wavelength of 3320.7 nm and reaches from 3315.7 to 3325.7 nm. Since this covers a large part of the Q-branches of $^{12}CH_4$ and $^{13}CH_4$ as it would have been expected, the test represents an evidentiary confirmation of the mathematical procedure.

The parameter p according to Eq. (8) determines the quality of the result to a large extent. Fig. 4 shows $P_{int}(\lambda)$ around its absolute maxima at 3315 and 3326 nm for values of p between 1 and 9%. The individual curves are shifted by 0.5 relative to each other in vertical direction so that the progress can be clearly seen. With increasing p the secondary maxima between 3200 and 3300 nm and between 3350 and 3450 nm successively disappear whereas the main maximum remains almost unaffected. From 8.5% on only the absolute maximum remains, and for that reason this value was chosen in the previous paragraph.

3.2. Mixture of $^{12}CH_4$, $^{12}C_2H_6$ and $^{12}C_2H_4$

The second test of the algorithm was performed on a (simulative) mixture of methane, ethane and ethylene (all carbon atoms with the mass number 12). Fig. 5 displays the three absorption spectra normalized to one. This combination was chosen, because it is apparently not possible to visually identify the most suited wavelength range for a spectroscopic analysis with a single laser (tunability 10 nm).

Fig. 6 displays the evaluation results. It shows:

- The $\Delta S_{ij,Q}(\lambda)$ according to Eq. (7) for the three possible gas dyads $^{12}CH_4$ – $^{12}C_2H_6$, $^{12}CH_4$ – $^{12}C_2H_4$ and $^{12}C_2H_6$ – $^{12}C_2H_4$.
- $P(\lambda)$ (the product of all filtered differences according to Eq. (8)) and
- $P_{int}(\lambda)$ (the integral of $P(\lambda)$ over the 10 nm laser tuning range according to Eq. (9)).

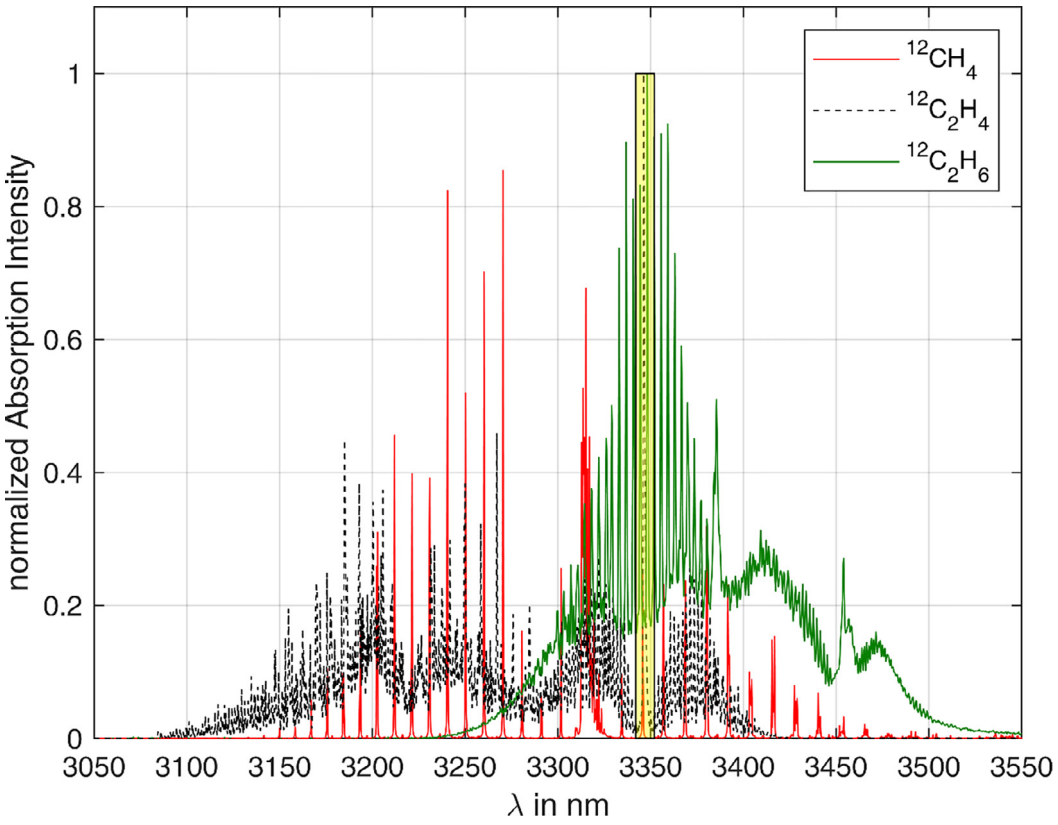

Fig. 5. Absorption spectra of $^{12}CH_4$, $^{12}C_2H_6$ and $^{12}C_2H_4$ [18–20].

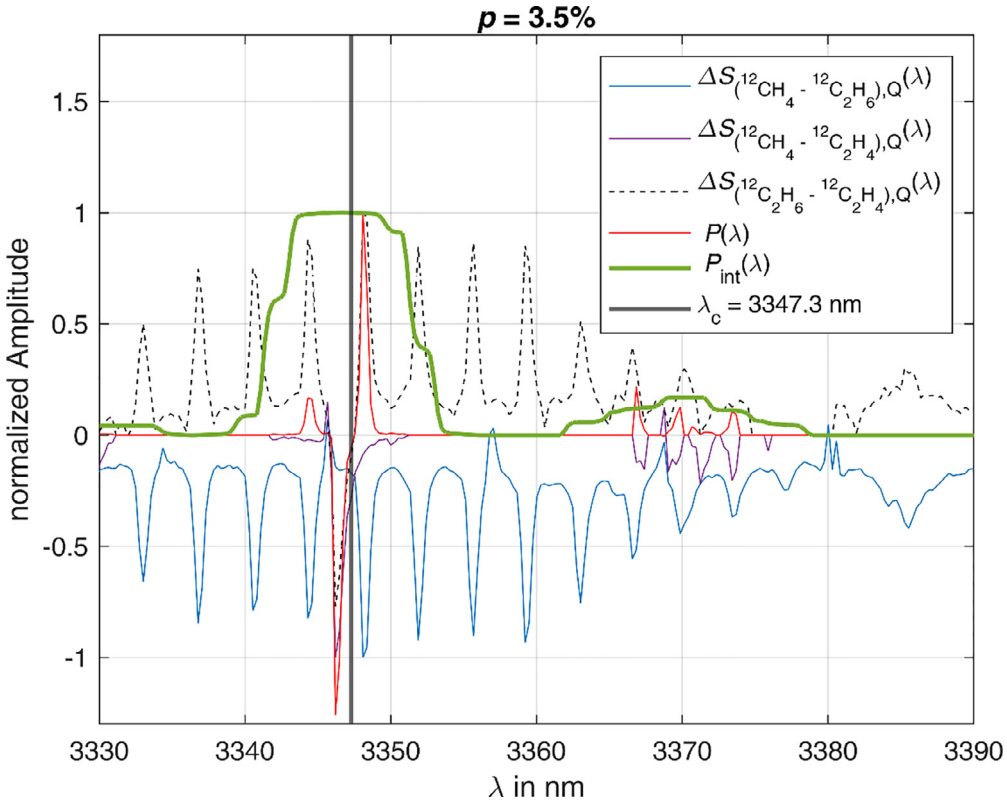

Fig. 6. Evaluation of the mixture $^{12}CH_4$, $^{12}C_2H_6$, and $^{12}C_2H_4$ all quantities are normalized to "one".

The resulting optimal center wavelength of the laser according to Eq. (11) equals 3347.3 nm. It is marked in Fig. 6 with a dark grey vertical line. The laser allows spectral tuning from 3342.3 to 3352.3 nm. It covers the characteristically high $^{12}C_2H_4$ line at ca. 3346 nm as well as the two strongest rotational lines of $^{12}C_2H_6$ and one relatively strong and discrete line of $^{12}CH_4$. The range is marked in Fig. 5 (yellow box). The result of this evaluation is very plausible and represents another confirmation for the applicability of the mathematical procedure.

4. Conclusion

We presented, to our knowledge, the first quantitative method to determine the optimal spectral range for a sensitive and selective analysis of a gaseous mixture. The method is particularly suitable for spectrometers based on tunable diode lasers. A prerequisite for its application is that absorption spectra of all gases in the mixture are known. The mathematical procedure identifies wavelength regions, in which the spectra of the single gases significantly differ and, at the same time, the absorption is strong. The definition of a threshold ensures that the best suited spectral region is found. The median of the optimal spectral range is selected as the laser's center wavelength.

The procedure was tried on two simulative gas mixtures. A first test was carried out on a mixture that allowed it to identify the perfect region through educated guessing. That the algorithm yielded the expected region is a convincing confirmation of the method. The second test of the algorithm was performed on a mixture where it was obviously not possible to visually identify the most suited wavelength range. The result of this evaluation is very plausible and represents another confirmation for the method.

Finally, it should be mentioned that the applicability depends primarily on the available spectra and that the number of components in the mixture is theoretically limited only by the available computing power. In practice, a spectrometer based on a single diode laser will probably never be applied to mixtures of more than 10 gases.

A limitation of the practical applicability is the fact that the algorithm is based on perfect spectra. Noise and other aspects of metrological reality are not taken into account. Only under these conditions are the results independent of the concentration of the individual components and their ratios.

CRediT authorship contribution statement

Marc-Simon Bahr: Conceptualization, Validation, Resources, Writing original draft, Visualization, Term. **Bernd Baumann**: Conceptualization, Validation, Writing review & editing, Term. **Marcus Wolff**: Conceptualization, Validation, Resources, Writing review & editing, Supervision, Project administration, Funding acquisition, Term.

Declaration of Competing Interest

The authors declare that they have no known competing financial interests or personal relationships that could have appeared to influence the work reported in this paper.

Funding

This research was funded by Federal Ministry for the Environment, Nature Conservation and Nuclear Safety, Grant No. 67KI2075.

References

[1] Demtröder W. Laserspektroskopie 1: grundlagen. Germany: Springer Berlin Heidelberg; 2014.
[2] Demtröder W. Laserspektroskopie 2: experimentelle techniken. Germany: Springer Berlin Heidelberg; 2014.
[3] Werle P, Slemr F, Maurer K, Kormann R, Ucke R, Anker B. Near-and mid-infrared laser-optical sensors for gas analysis. Opt Lasers Eng 2002;37:101–14. doi:10.1016/S0143-8166(01)00092-6.
[4] Nanoplus nanosystems and Technologies GmbH, DFB Interband Cascade Lasers (ICL): 2800 nm - 4000 nm https://nanoplus.com/fileadmin/user_upload/Data_sheets/nanoplus_DFB_2800-4000nm.pdf (Accessed on 08 January 2022).
[5] Zeller W, Naehle L, Fuchs P, Gerschuetz F, Hildebrandt L, Koeth J. DFB lasers between 760 nm and 16 µm for sensing applications. Sensors 2010;10(4):2492–510 MDPI AG. doi:10.3390/s100402492.
[6] Vurgaftman I, et al. Interband cascade lasers. J Phys D Appl Phys 2015. https://iopscience.iop.org/article/10.1088/0022-3727/48/12/123001.
[7] Meyer J, Bewley W, Canedy C, Kim C, Kim M, Merritt C, Vurgaftman I. The interband cascade laser. Photonics 2020;7(3):75 MDPI AG. doi:10.3390/photonics7030075.
[8] Dyroff C. Tunable diode-laser absorption spectroscopy for trace-gas measurements with high sensitivity and low drift. Germany: Universitätsverlag Karlsruhe; 2009. p. 40.
[9] Lackner M. Tunable diode laser spectroscopy in the process industries: a review. Rev Chem Eng 2007 23. 65.. doi:10.1515/REVCE.2007.23.2.65.
[10] HITRAN on the Web https://hitran.iao.ru/ (Accessed on 03 January 2022).
[11] GEISA Spectroscopic database https://geisa.aeris-data.fr/ (Accessed on 06 January 2022).
[12] California Institute of Technology, Jet Propulsion Laboratory, Molecular Spectroscopy https://spec.jpl.nasa.gov/ (accessed on 08 January 2022).
[13] National institute of Standards and Technology, NIST Chemistry WebBook, Standard Reference Database Number 69 https://webbook.nist.gov/chemistry/ (accessed on 08 January 2022).
[14] Tomberg T, Vainio M, Hieta T, et al. Sub-parts-per-trillion level sensitivity in trace gas detection by cantilever-enhanced photo-acoustic spectroscopy. Sci Rep 2018;8:1848. doi:10.1038/s41598-018-20087-9.
[15] Vialar T. Handbook of mathematics. France: HDBoM; 2016.
[16] Georgii H. Stochastik: einführung in die wahrscheinlichkeitstheorie und statistik. Germany: De Gruyter; 2015.
[17] The MathWorks, Inc., MATLAB https://de.mathworks.com/products/matlab.html (accessed on 09 January 2022).
[18] Loh A, Wolff M. Absorption cross sections of 13C ethane and propane isotopologues in the 3 μm region. JQSRT 2017;203:517–21.
[19] Loh A, Wolff M. High resolution spectra of 13C ethane and propane isotopologues photoacoustically measured using interband cascade lasers near 3.33 and 3.38 μm, respectively. JQSRT 2019;227:111–16.
[20] Gordon IE, Rothman LS, Hargreaves RJ, et al. The HITRAN2020 molecular spectroscopic database. JQSRT 2022;277:107949.
[21] Alrefae M, Es-sebbar E, Farooq A. Absorption cross-section measurements of methane, ethane, ethylene and methanol at high temperatures. J Mol Spectrosc 2014:8–14. doi:10.1016/j.jms.2014.06.007.

frontiers | Frontiers in Environmental Chemistry

TYPE Original Research
PUBLISHED 14 November 2022
DOI 10.3389/fenvc.2022.1029708

OPEN ACCESS

EDITED BY
Vincenzo Spagnolo,
Politecnico di Bari, Italy

REVIEWED BY
Andrea Zifarelli,
University of Bari Aldo Moro, Italy
Gustavo A. Zelada-Guillén,
National Autonomous University of Mexico, Mexico

*CORRESPONDENCE
Marc-Simon Bahr,
marc-simon.bahr@haw-hamburg.de

†These authors share first authorship

‡These authors share senior authorship

SPECIALTY SECTION
This article was submitted to Environmental Analytical Methods, a section of the journal Frontiers in Environmental Chemistry

RECEIVED 27 August 2022
ACCEPTED 21 October 2022
PUBLISHED 14 November 2022

CITATION
Bahr M-S and Wolff M (2022), PAS-based isotopologic analysis of highly concentrated methane.
Front. Environ. Chem. 3:1029708.
doi: 10.3389/fenvc.2022.1029708

PAS-based isotopologic analysis of highly concentrated methane

Marc-Simon Bahr[1,2*†] and Marcus Wolff[1‡]

[1]Heinrich Blasius Institute of Physical Technologies, Hamburg University of Applied Sciences, Hamburg, Germany, [2]School of Computing, Engineering and Physical Sciences, University of the West of Scotland, Scotland, United Kingdom

Photoacoustic spectroscopy (PAS) is typically used for the detection of trace gases. In this way, mixtures of short-chain hydrocarbons such as methane, ethane or propane can be analyzed with detection limits in the range of parts per million (ppm) or parts per billion (ppb) or even below. However, there are a number of applications where highly concentrated mixtures need to be analyzed. In some cases even the isotopologic composition of certain hydrocarbons needs to be determined. Examples can be found in natural gas production and planetary research. We present PAS-based isotopologic analyses of two digit percentage-level methane concentrations in nitrogen. The investigation allows conclusions to be drawn about the extent to which PAS is suitable for an isotopologic analysis of undiluted natural gas-like mixtures.

KEYWORDS

photoacoustic spectroscopy, interband cascade laser, natural gas, $^{12}CH_4$, $^{13}CH_4$

1 Introduction

While in recent years carbon dioxide (CO_2) was primarily proclaimed as the driver of global warming, methane (CH_4) as a greenhouse gas has now become a central component of climatic research processes (Nisbet et al., 2021). This is due in particular to the fact that methane has an up to 34 times higher global warming potential compared to CO_2 (Jacobson, 2021). In this context, it may become extraordinarily important that the isotopologic composition of methane differs depending on the emission source. A sensitive and selective detection of the two main isotopologues, $^{12}CH_4$ and $^{13}CH_4$, whose natural abundances are 98.9% and 1.1%, respectively, could allow it to determine whether methane traces originate from biogenic or anthropogenic sources (Schwietzke et al., 2016). The fact that anthropogenic sources tend to a have slightly higher $^{13}CH_4$ content can help identify and contain them and, thus, reduce the associated contribution to climate change (Schroll et al., 2020).

Other applications require the analysis of samples with high methane concentration. An example is the natural gas production. Raw natural gas contains between 75 and 99% methane, 1–15% ethane and 1–10% propane. However, the exact composition plays a decisive role for numerous industrial applications. Changes in the energy content, which is strongly dependent on the different alkane fractions, must be compensated by adjusting certain production parameters (Leicher et al., 2017). Temperature-sensitive processes can be controlled, for example, by adjusting the oxygen content of a mixture (Mukhopadhyay and Sen, 2019).

Furthermore, the $^{13}C/^{12}C$ concentration ratio of natural gas allows conclusions to be drawn about the type of gas and its source (Fuex, 1977). Shale gas, for instance, exhibits a specific $^{13}C/^{12}C$ ratio. It is depleted in its $^{13}CH_4$ share in comparison to other types of natural gas. Due to the fact that the fracking technique implicates increased methane emissions into the atmosphere, its identification is of utmost importance (Howarth, 2019). Furthermore, the isotope ratio can be used to determine the shale porosity and permeability. These parameters, amongst others, determine the most suitable conveyor technique. The data can also help to optimize the shale stimulation treatment, saving cost and water and thus protecting the environment. Furthermore, the isotope ratio represents an important parameter for the horizontal drilling control (Zhang and Krooss, 2001).

Another application that requires the isotopologic analyses of high methane concentrations can be found in planetary and cometary research. The investigation of the atmospheric composition of planets such as Neptune, Titan and Uranus delivers important information about their formation and evolution (Fletcher et al., 2009; Moses et al., 2020). Astronomic theories, e.g. the core accretion and collapse model (Pollack et al., 1996) which explains the formation scenario of the Solar System, could be confirmed in that way.

The isotopologic "signature" of methane, i.e. the concentration ratio of $^{12}CH_4$ and $^{13}CH_4$, is usually expressed as the deviation from the Pee Dee Belemnite standard in per mill (parts per thousand). This $\delta^{13}C$ value is defined as:

$$\delta^{13}C = \left(\frac{R_{sample}}{R_{std}} - 1\right) \cdot 1000\%,$$

where R_{sample} is the $^{13}CH_4/^{12}CH_4$ ratio of the sample and R_{std} = 0.0112372 (Reference and intercomparison materials for stable isotopes of light elements. Proceedings of a consultants meeting held in Vienna, 1–3 December 1993, 1995).

A very established and precise method for the analysis of gas mixtures is gas chromatography (GC). This technique allows molecular components to be separated by means of a separation column. The individual molecules are sequentially released from the separation column with a time delay, the so-called retention time, and subsequently detected by a detector, e.g., a flame ionization detector. The resulting chromatogram shows which types of molecules were present in the sample and their respective concentrations (Poole, 2021). However, since different isotopologues of the same molecule do hardly differ in their retention time, an isotope analysis by GC is not possible. In order to achieve this, GC is combined with mass spectrometry. The so-called isotope-ratio mass spectrometry (IRMS) represents the gold standard for isotope analyses (Sessions, 2006).

An alternative to IRMS could be photoacoustic spectroscopy (PAS) (Palzer, 2020). PAS is mainly suitable for the detection of trace gases but has been shown to enable the identification and quantification of methane isotopologues in the single-digit per mill range (Giglio et al., 2022) down to the parts per million (ppm) range (Loh and Wolff, 2019). The latter corresponds to typical concentrations in the atmosphere (van Amstel, 2012).

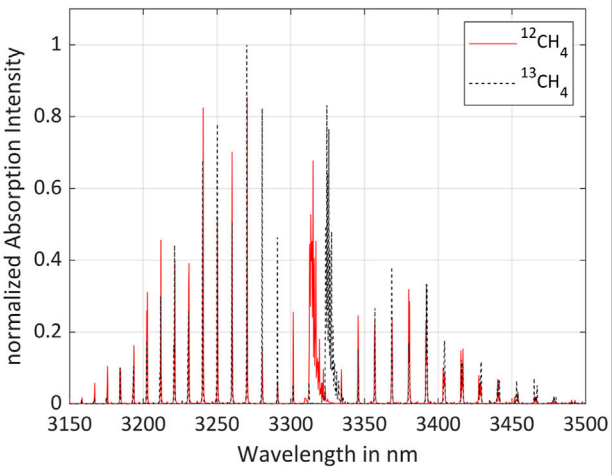

FIGURE 1
Fundamental vibrational absorption spectra of $^{12}CH_4$ and $^{13}CH_4$ (Gordon et al., 2022).

To the best of our knowledge, we investigate for the first time the applicability of PAS for isotopologic analysis of highly concentrated methane samples. We present first measurements of $^{13}CH_4/^{12}CH_4$ mixtures in nitrogen with concentrations of 25–70% and 0.28–3.00%, respectively, under laboratory conditions. The measurement results are then evaluated using cross-validation in conjunction with Partial Least Squares Regression (PLSR). This process is also used for sensor calibration. Chapter 2 shows the relevant methane absorption spectra and describes the experimental setup and the measurement procedure. The third chapter presents the resulting measurements, which are subsequently discussed in Chapter 4.

2 Methods and material

2.1 $^{12}CH_4$ and $^{13}CH_4$ absorption spectra

The isotopologic analysis has been performed using a spectrally tunable interband cascade laser (ICL) emitting in the spectral range of the fundamental vibration of $^{12}CH_4$ and $^{13}CH_4$. Figure 1 shows the absorption spectra of the two isotopologues at room temperature (296 K) and atmospheric pressure (1,013.25 hPa) (HITRAN on the Web, 2022). The optimum center wavelength of the laser has been determined using a mathematical algorithm (Bahr et al., 2022). Figure 2 displays the Q-branches of the fundamental vibrational absorption together with the tuning range of the laser, represented by the yellow box.

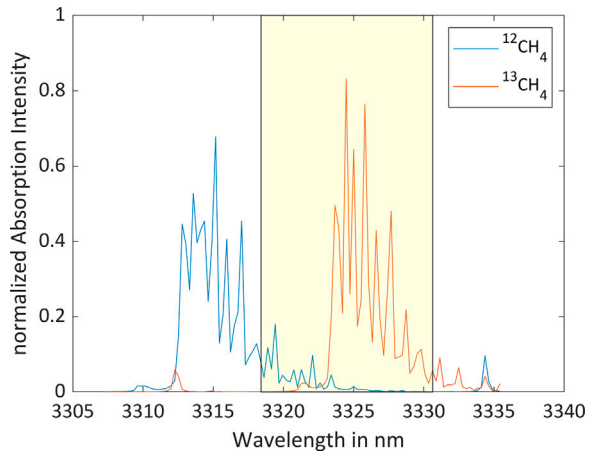

FIGURE 2
Q-branches of the fundamental vibrational absorption spectra of $^{12}CH_4$ and $^{13}CH_4$ (Gordon et al., 2022) together with the tuning range of the ICL (yellow box).

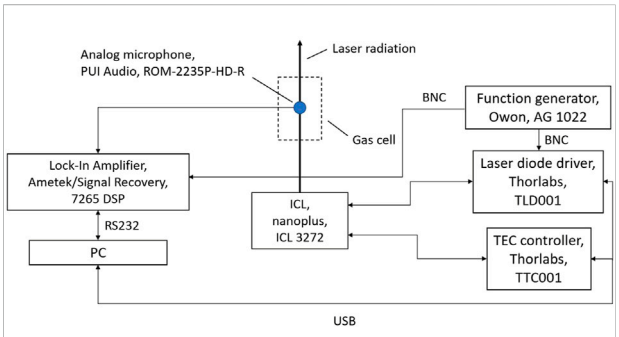

FIGURE 3
Experimental setup.

2.2 Measurement setup

The measurement setup is schematically shown in Figure 3. The ICL 3272 used in this investigation was manufactured by nanoplus GmbH (Gerbrunn, Germany). It exhibits a center wavelength of 3,323 nm with a spectral linewidth below 20 MHz. The laser can be operated at temperatures between 20 and 30°C. Stimulated emission occurs with electric currents between 19 and 120 mA. The ICL is operated using the Thorlabs (Newton, MA/United States) laser diode driver TLD001 and its temperature is controlled by the Thorlabs controller TTC001. The laser current can be set with an accuracy of 10 µA. The noise level is below 3 µA rms. The ICL chip has been installed in a TO66 housing including a Peltier element and a temperature sensor for temperature regulation. The laser provides single-mode emission that is spectrally continuously tunable between 3,318.41 nm and 3,330.64 nm. The maximum output power is approximately 15 mW. The laser beam passes centrally through the cylindrically symmetrical photoacoustic cell. The custom-made cell is designed according to the established H geometry featuring a longitudinal resonance around 3 kHz (Nodov 1978). The resonance tube is 60 mm long with a diameter of 6 mm and the buffer volumes at both ends of the cell have each a length of 30 mm and a diameter of 24 mm, resulting in a total absorption length of 120 mm. The photoacoustics signal is detected by the analog microphone ROM-2235P-HD-R from PUI Audio (Fairborn, OH/United States) which is mounted in the center of the cell with the membrane flush with the inner wall. It exhibits a diameter of 5.8 mm and a detection sensitivity of -35 ± 3 dB at 1 kHz and 50 cm distance. The Ametek/Signal Recovery lock-in amplifier DSP LIA (Berwyn, IL/United States) performs the phase-sensitive detection of the microphone signal. The Owon (Zhangzhou, China) function generator AG 1022 provides the frequency reference for the ICL modulation and the lock-in detection. The entire experimental setup is controlled using a MATLAB script on a PC. The PLSR algorithm including the leave-one-out cross-validation is implemented in a MATLAB script and performed by the PC.

The gas flow system is schematically shown in Figure 4. Gas is provided in three containers:

(1) CH_4 of natural isotopologue abundance (1 L geometric volume, 12 bar filling pressure, purity: 4.5, distributor: Westfalen AG),
(2) $^{13}CH_4$ (416 ml geometric volume, 2.3 bar filling pressure, purity: 99%, distributor: Merck/Sigma Aldrich),
(3) N_2 (10 L geometric volume, 200 bar filling pressure, purity: 5.0, distributor: Westfalen AG).

Mixtures are generated using the 6 Channel Gas mixer from QCAL (Munich, Germany) which is controlled by a PC. The maximum relative error of the mixture concentrations, specified by the manufacturer, is up to 2%. To ensure the correctness of the mixer performance, all compositions are analyzed by the gas chromatograph 9130 from Fisons (Ipswich, United Kindgom). The photoacoustic measurements were performed under static conditions after the gas mixtures were injected into the gas cell.

2.3 Measurement procedure

Photoacoustic spectroscopy is based on the absorption of modulated radiation and the subsequent conversion of the absorbed energy by collisions into a thermal wave and consequently into a pressure wave. This sound wave can be amplified taking advantage of an acoustic resonance of the sample cell and is usually detected by a microphone (Demtröder, 2007; Demtröder, 2013).

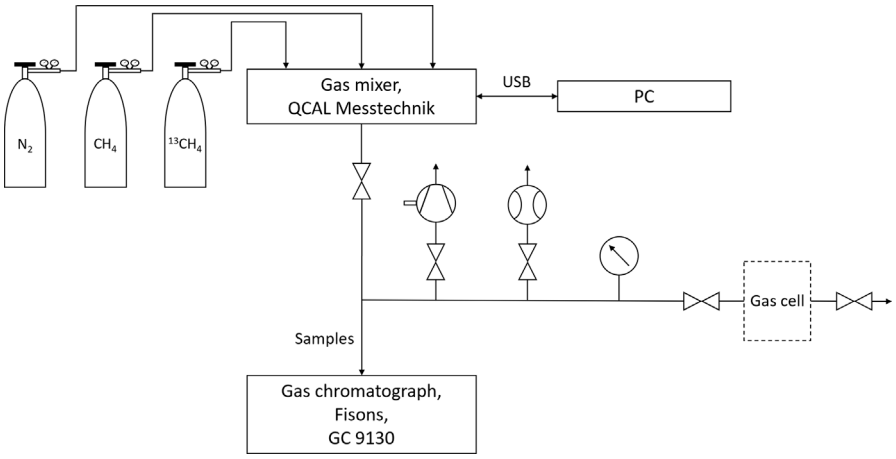

FIGURE 4
Gas flow system.

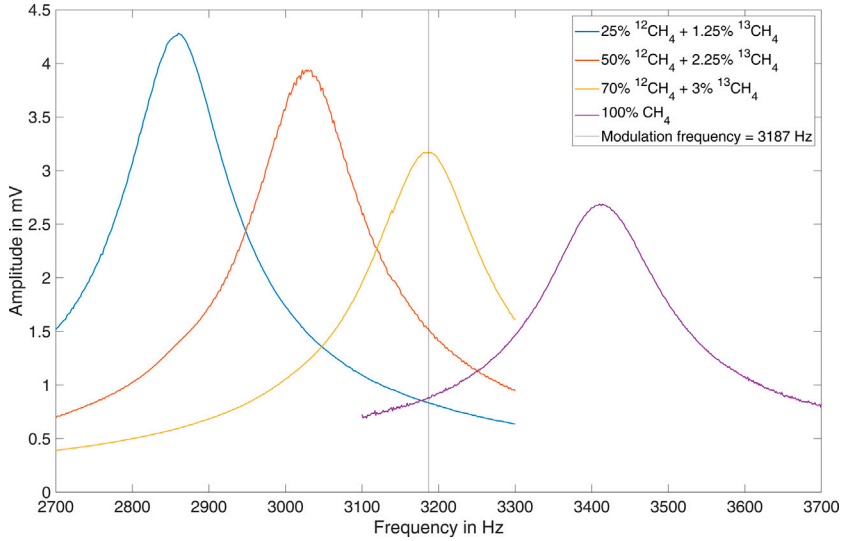

FIGURE 5
Photoacoustics signal as function of the modulation frequency for different mixtures.

The ICL applied in this investigation is directly injection-current modulated at a constant operation temperature of 20°C. The current consists of one part that is continuously tuned between 75 and 120 mA covering a spectral range of approximately 12 nm and a second, sinusoidally modulated part that is responsible for the generation of the PA signal. The latter exhibits a modulation amplitude of 1.24 mA which corresponds to a spectral range of approximately 0.1 nm.

The frequency of the reference signal fed into the lock-in amplifier equals the resonance frequency of the measurement cell. This leads to a $1f$ wavelength modulation, as a result of which the recorded spectra correspond to the derivative of the absorption spectra. The advantage of this modulation method is that changes in the spectra are emphasized. This makes it easier to distinguish different gas components.

The acoustic resonance of a sample cell depends sensitively on the speed of sound. Due to the significant mass difference, doubling or tripling a methane concentration of 25% in an N_2 matrix considerably changes the speed of sound resulting in a large shift of the cell's resonance frequency (Selvaraj et al., 2019).

Figure 5 illustrates this phenomenon. It shows the PA signal as function of the modulation frequency for (total) methane concentrations of 26.25%, 52.25%, 73.00% and 100.00%. Shifts in the resonant frequency due to temperature fluctuations of a few degrees Celsius are comparatively negligible. The subsequent analytical measurements were all performed at a modulation frequency of 3,187 Hz.

Over a large range, the PA signal is proportional to the concentration of the absorbing molecules. However, if the absorption is extremely strong, as in the case of the fundamental asymmetric stretching ν_3 of methane, and/or the concentration of the absorbing species is very high, saturation occurs and deviations from this linear relationship arise (Menduni et al., 2022). In Figure 5 it can be observed that the PA signal at the respective resonance frequency decreases as the methane concentration increases from 26.25% to 100.00%. The reason for this is twofold. Firstly, the majority of the absorption takes place in an increasingly shorter path length behind the entrance window. As a consequence, the overlap between the longitudinal mode and the intensity distribution of the laser will be weaker and the cell resonance is stimulated less effectively (Baumann et al., 2006; Baumann et al., 2007). The linear dependency between concentration and photoacoustic signal that applies in the ppm and ppb range is then no longer observable. For methane concentrations in the single digit percentage level the photoacoustic signal still increases with increasing concentration, however the dependence is non-linear (Zeninari et al., 2016). If concentrations are in the high percentage range, as shown in Figure 5, there is a reduction in amplitude with further increasing concentration.

This phenomenon is superimposed by a second effect. The photoacoustic signal generation is based on the transfer of internal energy of excited molecules (mainly vibration but also rotation) into kinetic energy of neighboring molecules (translation) via inelastic collisions. Therefore, the composition of the gas matrix significantly affects the relaxation dynamics and thus the photoacoustic response. Due to the high purity of the gas samples, the controlled laboratory environment and the evacuable gas flow system it is not expected that water vapor or other impurities play a major role in the relaxation process. Since there are no significant differences between the relaxation times of the two methane isotopologues, the $^{13}CH_4/^{12}CH_4$ ratio should also not have a substantial influence on the photoacoustic signal (Giglio et al., 2022). As no efficient vibro-vibrational (V-V) transition between the ν_3 state of CH_4 (CH_4^*) and N_2 exists, only three non-radiative relaxation channels are possible (Schilt et al., 2006):

(1) CH_4^*-N_2 collision followed by a vibro-translational (V-T) transition. This relaxation channel represents the main source of the PA signal if N_2 is present in the mixture.
(2) CH_4^*-CH_4 collision followed by V-V transitions. This relaxation channel does not contribute to the PA signal.
(3) CH_4^*-CH_4 collisions followed by a V-T transition. This relaxation channel represents an additional source of the PA signal. The respective signal is phase-shifted in relation to the CH_4^*-N_2 signal. If no N_2 is present in the mixture, it is the only source of the PA signal.

TABLE 1 $^{12}CH_4$ and $^{13}CH_4$ concentrations of the nine investigated mixtures (rest: N_2).

Figure no.	$^{12}CH_4$ concentration	$^{13}CH_4$ concentration
6	25%	- 0.28%
		- 0.75%
		- 1.25%
7	50%	- 0.56%
		- 1.75%
		- 2.25%
8	70%	- 0.78%
		- 2.25%
		- 3.00%

In our analytical measurements we are varying the (total) methane concentration between 25 and 73%. This changes the number of nitrogen molecules available for the according V-T collisions considerably and thus determines the efficiency of the photoacoustic signal generation.

The evaluation algorithm responsible for the sensor calibration has to be able to compensate the changing dependencies originating from the effectivity of the acoustic resonance stimulation as well as the matrix effects arising from changes in the gas composition.

3 Results

Table 1 lists the nine isotopologue mixtures that were investigated. The residual gas to 100% was always N_2. The $^{12}CH_4$ concentrations were chosen to cover the two-digit percentage range as complete as possible. The choice of $^{13}CH_4$ concentrations was severely restricted due to the flow limitations of the gas mixer. Figures 6–8 show the respective photoacoustic spectra, i.e. the PA signal as function of the average laser current. All measurements were taken at a sample temperature of 26°C and a pressure of 1,016 hPa.

Considering the complexity of the collected spectra a sensor calibration in the form of a quantitative multivariate approach is implemented to validate the methane isotopologue concentrations and to test the suitability of the method. In particular, Partial Least Squares Regression (PLSR) proved to be applicable for determining the concentrations of mixture components from photoacoustic spectra (Loh and Wolff, 2020; Saalberg and Wolff, 2018).

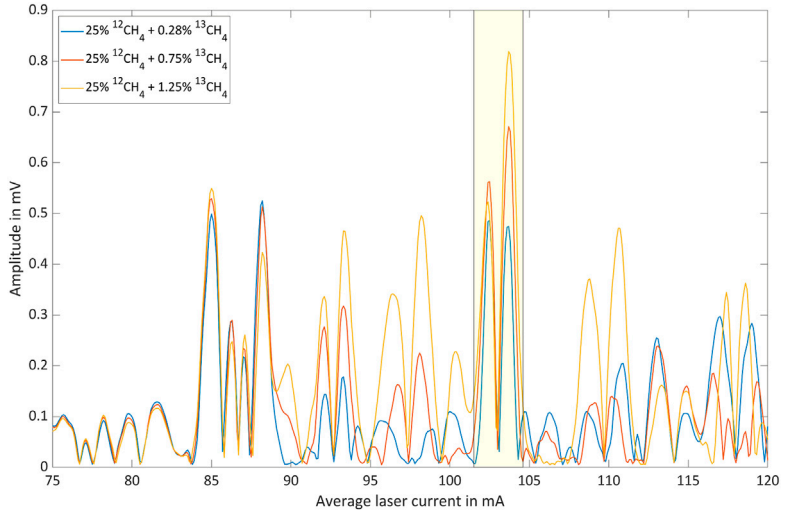

FIGURE 6
Photoacoustic signal as function of the average laser current for 25% $^{12}CH_4$ with three different $^{13}CH_4$ shares in nitrogen.

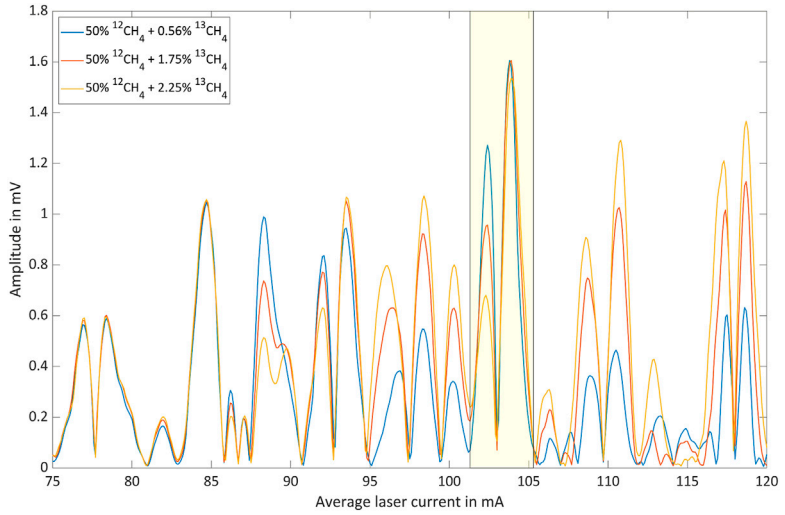

FIGURE 7
Photoacoustic signal as function of the average laser current for 50% $^{12}CH_4$ with three different $^{13}CH_4$ shares in nitrogen.

Figure 9 shows the true and the predicted methane isotopologue concentrations, after a leave-one-out cross-validation based on PLSR was applied to all nine investigated mixtures. The mixture numbers in Figure 9 correspond to the order given in Table 1. The absolute root-mean-square-errors for the predicted $^{12}CH_4$ and $^{13}CH_4$ concentrations were calculated to 3.08% and 0.29%, respectively.

4 Discussion

Figures 6–8 show wavelength-modulated photoacoustic spectra that were measured using the single modulation frequency ($1f$) as reference for the lock-in amplification. Therefore, they represent approximately the derivative of the absorption spectrum (Demtröder, 2007; Demtröder, 2013). However, due to the nonlinear spectral behavior of

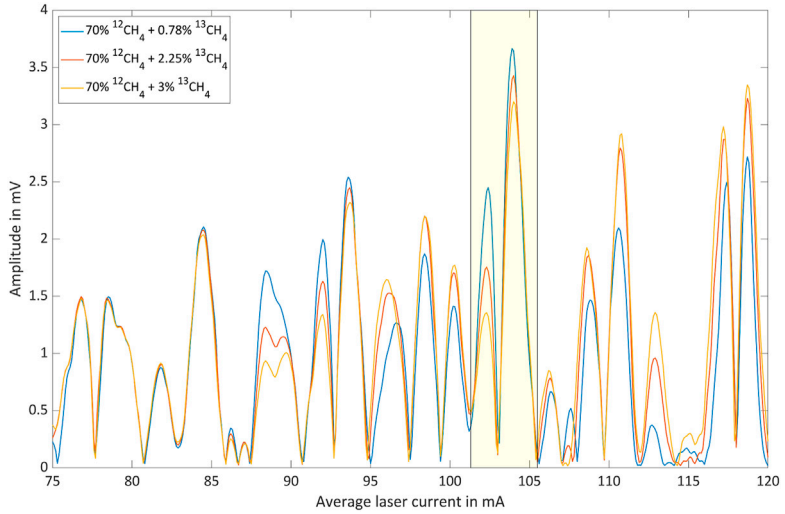

FIGURE 8
Photoacoustic signal as function of the average laser current for 70% $^{12}CH_4$ with three different $^{13}CH_4$ shares in nitrogen.

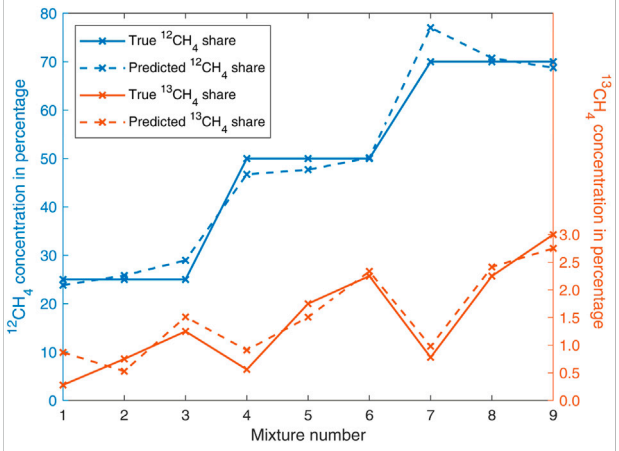

FIGURE 9
Evaluation of the investigated methane isotopologue mixtures by leave-one-out cross-validation based on PLSR.

injection current modulated semiconductor lasers, the agreement is not perfect (Bahr and Wolff, 2021). In addition, the spectra are not normalized with respect to the emission power of the laser and the output depends considerably on the modulation amplitude.

The spectral tuning range of the laser was selected using an optimization algorithm in such a way that not only characteristic absorption lines of both isotopologues are accessible, but that these lines also have absorption strengths of the same order of magnitude around the isotopologue ratio of interest (natural abundance). The latter is important as it ensures that the signal levels are comparable.

The spectral region associated with average laser currents between 75 mA and 85 mA is clearly dominated by $^{12}CH_4$ lines. This is illustrated by the fact that the according peaks are only weakly dependent on the $^{13}CH_4$ concentration. However, the dependence of the photoacoustic signal on the $^{12}CH_4$ concentration is significant. The spectral region associated with average laser currents between 85 mA and 120 mA, on the other hand, is obviously characterized by $^{13}CH_4$ absorption. However, $^{12}CH_4$ exhibits a considerable contribution in this range leading to a base-signal that increases with increasing $^{12}CH_4$ concentration. The $^{13}CH_4$ concentration dependent signal inversion, which is for instance observable between 25% and 50% $^{12}CH_4$ around 103 mA, marked by yellow boxes, can be explained as a result of two opposing effects:

(1) Increasing signal with increasing concentration due to higher absorption.
(2) Decreasing signal with increasing concentration due to less effective stimulation of cell resonance (see subsection 2.3).

The inversion can only be observed at selected average laser currents because the phenomenon requires a specific combination of absorption path length, absorption coefficient and concentration, in which the contributions of the two isotopologues add up.

In conclusion it can be stated that, even though the number of investigated mixtures of the two main methane isotopologues $^{12}CH_4$ and $^{13}CH_4$ is, with nine samples, quite

limited and the error of the gas mixer used is significant, the measurements displayed in Figures 6–8 and the evaluation based on PLSR displayed in Figure 9 prove to a satisfactory extent that photoacoustic spectroscopy is a suitable method for the isotopologic analysis of highly concentrated methane. The accuracy of the sensor can be considerably improved by adding more measurements to the training data of the PLSR algorithm. The presented results with samples in the high double-digit percentage range make it appear possible to analyze undiluted natural gas samples. However, the presence of other hydrocarbons would make this task significantly more challenging. In any case, it is important to consider the resonance frequency shift associated with concentration changes.

Data availability statement

The original contributions presented in the study are included in the article/supplementary material, further inquiries can be directed to the corresponding author.

Author contributions

Writing, original draft preparations: M-SB; writing—review and editing: MW. Both authors contributed to manuscript revision, read, and approved the submitted version.

Funding

This research was funded by the German Federal Ministry for the Environment, Nature Conservation and Nuclear Safety, Grant No. 67KI2075. We acknowledge support for the article processing charge by the Open Access Publication Fund of Hamburg University of Applied Sciences.

Conflict of interest

The authors declare that the research was conducted in the absence of any commercial or financial relationships that could be construed as a potential conflict of interest.

Publisher's note

All claims expressed in this article are solely those of the authors and do not necessarily represent those of their affiliated organizations, or those of the publisher, the editors and the reviewers. Any product that may be evaluated in this article, or claim that may be made by its manufacturer, is not guaranteed or endorsed by the publisher.

References

Bahr, M.-S., Baumann, B., and Wolff, M. (2022). Determining the most suitable spectral range for TDLS – A quantitative approach. *J. Quantitative Spectrosc. Radiat. Transf.* 286, 108216. doi:10.1016/j.jqsrt.2022.108216

Bahr, M.-S., and Wolff, M. (2021). Interferometric technique for the spectral characterization of high frequency current-modulated mid-infrared semiconductor lasers. *Photonics* 8 (10), 443. doi:10.3390/photonics8100443

Baumann, B., Kost, B., Groninga, H., and Wolff, M. (2006). Eigenmode analysis of photoacoustic sensors via finite element method. *Rev. Sci. Instrum.* 77 (4), 044901. doi:10.1063/1.2186808

Baumann, B., Wolff, M., Kost, B., and Groninga, H. (2007). Finite element calculation of photoacoustic signals. *Appl. Opt.* 46 (7), 1120–1125. doi:10.1364/ao.46.001120

Demtröder, W. (2013). *Laserspektroskopie 2: Experimentelle techniken*. 6th edn. Berlin, Heidelberg: Springer Berlin Heidelberg. [Online]. Available at: https://books.google.de/books?id=Z5IhBAAAQBAJ.

Demtröder, W. (2007). *Laserspektroskopie: Grundlagen und Techniken*. 5th edn. Berlin, Heidelberg: Springer-Verlag Berlin Heidelberg. [Online]. Available at: https://books.google.de/books?id=AhckBAAAQBAJ.

ETDEWEB (1995). "Reference and intercomparison materials for stable isotopes of light elements," in *Proceedings of a consultants meeting held in Vienna*, 1–3. December 1993 [Online]. Available at: https://www.osti.gov/etdeweb/biblio/195611.

Fletcher, L. N., Orton, G. S., Teanby, N. A., Irwin, P., and Bjoraker, G. L. (2009). Methane and its isotopologues on saturn from cassini/CIRS observations. *Icarus* 199 (2), 351–367. doi:10.1016/j.icarus.2008.09.019

Fuex, A. (1977). The use of stable carbon isotopes in hydrocarbon exploration. *J. Geochem. Explor.* 7, 155–188. doi:10.1016/0375-6742(77)90080-2

Giglio, M., Olivieri, M., Sukhinets, A., Di Gioia, M., Elefante, A., Menduni, G., et al. (2022). "Measurement of the methane isotopologues relaxation rate exploiting quartz-enhanced photoacoustic spectroscopy", in *Quantum Sensing and Nano Electronics and Photonics XVIII*. San Francisco, United States: SPIE/International Society for Optical Engineering, 56. 1/22/2022 - 2/28/2022.

Gordon, I. E., Rothman, L. S., Hargreaves, R. J., Hashemi, R., Karlovets, E. V., Skinner, F. M., et al. (2022). The HITRAN2020 molecular spectroscopic database. *J. Quantitative Spectrosc. Radiat. Transf.* 277, 107949. [Online]. doi:10.1016/j.jqsrt.2021.107949

HITRAN on the Web (2022). *HITRAN on the Web*. [Online]. Available at: https://hitran.iao.ru/(Accessed July 12, 2022).

Howarth, R. W. (2019). Ideas and perspectives: Is shale gas a major driver of recent increase in global atmospheric methane? *Biogeosciences* 16 (15), 3033–3046. [Online]. doi:10.5194/bg-16-3033-2019

Jacobson, M. Z. (2021). *100% clean, renewable energy and storage for everything*. Cambridge: Cambridge University Press.

Leicher, J., Giese, A., Görner, K., Werschy, M., Krause, H., and Dörr, H. (2017). Natural gas quality fluctuations – surveys and statistics on the situation in Germany. *Energy Procedia* 120, 165–172. doi:10.1016/j.egypro.2017.07.161

Loh, A., and Wolff, M. (2020). Multivariate analysis of photoacoustic spectra for the detection of short-chained hydrocarbon isotopologues. *Mol. (Basel, Switz.* 25, 2266–2269. doi:10.3390/molecules25092266

Loh, A., and Wolff, M. (2019). "Photoacoustic detection of short-chained hydrocarbon isotopologues," in *7th international symposium on sensor science* (Basel Switzerland: MDPI), 23.

Menduni, G., Zifarelli, A., Sampaolo, A., Patimisco, P., Giglio, M., Amoroso, N., et al. (2022). High-concentration methane and ethane QEPAS detection employing partial least squares regression to filter out energy relaxation dependence on gas matrix composition. *Photoacoustics* 26, 100349. doi:10.1016/j.pacs.2022.100349

Moses, J. I., Cavalié, T., Fletcher, L. N., and Roman, M. T. (2020). Atmospheric chemistry on Uranus and Neptune, *Philosophical Trans. Ser. A, Math. Phys. Eng. Sci.* 378 (2187), 20190477.

Mukhopadhyay, A., and Sen, S. (2019). *Fundamentals of combustion engineering [online]*. Milton: Chapman and Hall/CRC. Available at: https://search.ebscohost.com/login.aspx?direct=true&scope=site&db=nlebk&db=nlabk&AN=2036012.

Nisbet, E. G., Dlugokencky, E. J., Fisher, R. E., France, J. L., Lowry, D., Manning, M. R., et al. (2021). Atmospheric methane and nitrous oxide: Challenges alongthe path to net zero. *Phil. Trans. R. Soc. A* 379 (2210), 20200457. doi:10.1098/rsta.2020.0457

Nodov, E. (1978). Optimization of resonant cell design for optoacoustic gas spectroscopy (H-type). *Appl. Opt.* 17 (7), 1110–1119. doi:10.1364/ao.17.001110

Palzer, S. (2020). Photoacoustic-based gas sensing: A review. *Sensors (Basel, Switz.* 20, 2745–2749. doi:10.3390/s20092745

Pollack, J. B., Hubickyj, O., Bodenheimer, P., Lissauer, J. J., Podolak, M., and Greenzweig, Y. (1996). Formation of the giant planets by concurrent accretion of solids and gas. *Icarus* 124 (1), 62–85. [Online]. doi:10.1006/icar.1996.0190

Poole, C. (2021). *Gas chromatography*. Second Edition. [Online], Amsterdam, Elsevier. Available at: https://www.sciencedirect.com/science/book/9780128206751.

Saalberg, Y., and Wolff, M. (2018). Multivariate analysis as a tool to identify concentrations from strongly overlapping gas spectra. *Sensors (Basel, Switz.* 18 (5), 1562. doi:10.3390/s18051562

Schilt, S., Besson, J.-P., and Thévenaz, L. (2006). Near-infrared laser photoacoustic detection of methane: The impact of molecular relaxation. *Appl. Phys. B* 82 (2), 319–328. [Online]. doi:10.1007/s00340-005-2076-y

Schroll, M., Keppler, F., Greule, M., Eckhardt, C., Zorn, H., and Lenhart, K. (2020). The stable carbon isotope signature of methane produced by saprotrophic fungi. *Biogeosciences* 17 (14), 3891–3901. [Online]. doi:10.5194/bg-17-3891-2020

Schwietzke, S., Sherwood, O. A., Bruhwiler, L. M. P., Miller, J. B., Etiope, G., Dlugokencky, E. J., et al. (2016). Upward revision of global fossil fuel methane emissions based on isotope database. *Nature* 538 (7623), 88–91. [Online]. doi:10.1038/nature19797

Selvaraj, R., Vasa, N. J., and Shiva Nagendra, S. M. (2019). Off-resonant photoacoustic spectroscopy for analysis of multicomponent gas mixtures at high concentrations using broadband vibrational overtones of individual gas species. *Appl. Opt.* 58 (15), 4118–4126. doi:10.1364/ao.58.004118

Sessions, A. L. (2006). Isotope-ratio detection for gas chromatography. *J. Sep. Sci.* 29 (12), 1946–1961. [Online]. doi:10.1002/jssc.200600002

van Amstel, A. (2012). Methane. A review. *J. Integr. Environ. Sci.* 9 (1), 5–30. doi:10.1080/1943815x.2012.694892

Zeninari, V., Vallon, R., Risser, C., and Parvitte, B. (2016). Photoacoustic detection of methane in large concentrations with a helmholtz sensor: Simulation and experimentation. *Int. J. Thermophys.* 37 (1), 7–11. [Online]. doi:10.1007/s10765-015-2018-9

Zhang, T., and Krooss, B. M. (2001). Experimental investigation on the carbon isotope fractionation of methane during gas migration by diffusion through sedimentary rocks at elevated temperature and pressure. *Geochimica Cosmochimica Acta* 65 (16), 2723–2742. doi:10.1016/s0016-7037(01)00601-9

References

Alrefae, M., Es-sebbar, E.-t., & Farooq, A. (2014). Absorption cross-section measurements of methane, ethane, ethylene and methanol at high temperatures [PII: S0022285214001350]. *Journal of Molecular Spectroscopy*, *303*, 8–14. https://doi.org/10.1016/j.jms.2014.06.007

Bahr, M.-S., Baumann, B., & Wolff, M. (2022). Determining the most suitable spectral range for tdls – a quantitative approach. *Journal of Quantitative Spectroscopy and Radiative Transfer*, *286*, 108216. https://doi.org/10.1016/j.jqsrt.2022.108216

Bahr, M.-S., & Wolff, M. (2021). Interferometric technique for the spectral characterization of high frequency current-modulated mid-infrared semiconductor lasers [PII: photonics8100443]. *Photonics*, *8*(10), 443. https://doi.org/10.3390/photonics8100443

Bahr, M.-S., & Wolff, M. (2022). Pas-based isotopologic analysis of highly concentrated methane. *Frontiers in Environmental Chemistry*, *3*. https://doi.org/10.3389/fenvc.2022.1029708

Baumann, B., Kost, B., Groninga, H., & Wolff, M. (2006). Eigenmode analysis of photoacoustic sensors via finite element method. *Review of Scientific Instruments*, *77*(4), 044901. https://doi.org/10.1063/1.2186808

Baumann, B., Wolff, M., Kost, B., & Groninga, H. (2007). Finite element calculation of photoacoustic signals [Journal Article]. *Applied optics*, *46*(7), 1120–1125. https://doi.org/10.1364/ao.46.001120

Bell, A. G. (1880). On the production and reproduction of sound by light. *American Journal of Science*, *s3-20*(118), 305–324. https://doi.org/10.2475/ajs.s3-20.118.305

Besson, J.-P., Schilt, S., & Thévenaz, L. (2004). Multi-gas sensing based on photoacoustic spectroscopy using tunable laser diodes [Journal Article]. *Spectrochimica Acta Part A: Molecular and Biomolecular Spectroscopy*, *60*(14), 3449–3456. https://doi.org/10.1016/j.saa.2003.11.046

Bristol. (2020). *Bristol 828 series optical wavelength meter specifications*. Retrieved August 17, 2023, from https://www.bristol-inst.com/wp-content/uploads/2020/01/Bristol-828-Series-Optical-Wavelength-Meter-Specifications.pdf

Bristol. (2023). *Bristol wavemeter*. Retrieved August 17, 2023, from https://www.bristol-inst.com/bristol-instruments-products/wavelength-meters-scientific

Brodie, D., & Booth, G. (2010). *Aqa physics: Study guide*. Letts and Lonsdale.

Brown, A. S., Milton, M. J. T., Cowper, C. J., Squire, G. D., Bremser, W., & Branch, R. W. (2004). Analysis of natural gas by gas chromatography reduction of correlated uncertainties by normalisation [Journal Article Research Support, Non-U.S. Gov't]. *Journal of Chromatography A*, *1040*(2), 215–225. https://doi.org/10.1016/j.chroma.2004.04.007

Burdett, R. (2005). Amplitude modulated signals: The lock–in amplifier. In P. H. Sydenham & R. Thorn (Eds.), *Handbook of measuring system design*. Wiley. https://doi.org/10.1002/0471497398.mm588

Compur Monitors. (2021). *Infrared gas detectorstatox 501 lc ir und mc ir for combustible gases*. Retrieved October 24, 2023, from https://www.compur.com/en/stationary-gas-detectors/combustible-gas-detector-statox-501-lc-and-mc-ir/

D. Viveiros, J. Ribeiro, D. Flores, J. Ferreira, O. Frazao, J. L. Santos, & J. M. Baptista. (2014). Gas sensing using wavelength modulation spectroscopy. In SPIE (Ed.). D. Viveiros, J. Ribeiro, D. Flores, J. Ferreira, O. Frazão, J. L. Santos, & J. M. Baptista (Eds.), *Second international conference on applications of optics and photonics* (pp. 510–513, Vol. 9286). SPIE. https://doi.org/10.1117/12.2063811

Dąbrowski, K. M., Kuczyński, S., Barbacki, J., Włodek, T., Smulski, R., & Nagy, S. (2019). Downhole measurements and determination of natural gas composition using raman spectroscopy. *Journal of Natural Gas Science and Engineering*, *65*, 25–31. https://doi.org/10.1016/j.jngse.2019.02.003

Dändliker, R., Thalmann, R., & Prongué, D. (1988). Two-wavelength laser interferometry using superheterodyne detection [Journal Article]. *Optics Letters*, *13*(5), 339–341. https://doi.org/10.1364/OL.13.000339

Decourt, B., Debarre, R., & Alias, S. (2014). *Introduction to natural gas* (A.T. Kearney Energy Transition Institute, Ed.). Retrieved August 11, 2023, from https://www.energy-transition-institute.com/documents/17779499/17781903/Introduction+to+Natural+Gas_FactBook.pdf/cb59da84-42b6-936b-83dc-7f04688654e4?t=1561052377799

Demoulin, O., Le Clef, B., Navez, M., & Ruiz, P. (2008). Combustion of methane, ethane and propane and of mixtures of methane with ethane or propane

on pd/y-al2o3 catalysts. *Applied Catalysis A: General*, *344*(1-2), 1–9. https://doi.org/10.1016/j.apcata.2008.03.026

Demtröder, W. (2014a). *Laserspektroskopie 1: Grundlagen*. Springer Berlin Heidelberg.

Demtröder, W. (2014b). *Laserspektroskopie 2: Experimentelle techniken*. Springer Berlin Heidelberg.

Du, Z., Luo, G., An, Y., & Li, J. (2016). Dynamic spectral characteristics measurement of dfb interband cascade laser under injection current tuning. *Applied Physics Letters*, *109*(1), 011903. https://doi.org/10.1063/1.4955411

Duchowny, A., Mohnke, O., Thern, H., Dupuy, P. M., Widerøe, H. C., Faanes, A., Paulsen, A., Küppers, M., Blümich, B., & Adams, A. (2022). Composition analysis of natural gas by combined benchtop nmr spectroscopy and mechanistical multivariate regression [PII: S2352484722005364]. *Energy Reports*, *8*, 3661–3670. https://doi.org/10.1016/j.egyr.2022.02.289

Dyroff. (2009). *Tunable diode-laser absorption spectroscopy for trace-gas measurements with high sensitivity and low drift*. Universitätsverlag Karlsruhe.

Elliott, D. F. (Ed.). (1987). *Handbook of digital signal processing: Engineering applications*. Academic Press. http://www.sciencedirect.com/science/book/9780080507804

Engelberg, S. (2008). *Digital signal processing: An experimental approach*. Springer. https://doi.org/10.1007/978-1-84800-119-0

Faramawy, S., Zaki, T., & Sakr, A.-E. (2016). Natural gas origin, composition, and processing: A review [PII: S1875510016304139]. *Journal of Natural Gas Science and Engineering*, *34*, 34–54. https://doi.org/10.1016/j.jngse.2016.06.030

Federal Environmental Agency Germany. (2023). *Methane concentration in the atmosphere (monthly and annual averages)* (Federal Environmental Agency Germany, Ed.). Retrieved August 11, 2023, from https://www.umweltbundesamt.de/bild/methan-konzentration-in-der-atmosphaere-monats

Fletcher, L. N., Orton, G. S., Teanby, N. A., Irwin, P., & Bjoraker, G. L. (2009). Methane and its isotopologues on saturn from cassini/cirs observations [PII: S0019103508003643]. *Icarus*, *199*(2), 351–367.

Fuex, A. (1977). The use of stable carbon isotopes in hydrocarbon exploration [PII: 0375674277900802]. *Journal of Geochemical Exploration*, *7*, 155–188. https://doi.org/10.1016/0375-6742(77)90080-2

Gasnetz Hamburg GmbH. (2023). *Hamburg gas analysis 06/2023* (Gasnetz Hamburg GmbH, Ed.). Retrieved October 24, 2023, from https://filehub.admiralcloud.com/v5/deliverFile/f319f405-f8bf-411d-aa1f-93de20f26b9d?download=true

GEISA. (2022). *Https://geisa.aeris-data.fr*. Retrieved August 16, 2023, from https://geisa.aeris-data.fr/

Georgii. (2015). *Stochastik: Einführung in die wahrscheinlichkeitstheorie und statistik*. De Gruyter.

Germer, M., & Wolff, M. (2010). Photoacoustic investigation of qcl modulation techniques. *Journal of Physics: Conference Series*, *214*, 012067. https://doi.org/10.1088/1742-6596/214/1/012067

Giancoli, D. C. (2023). *Physics for scientists & engineers with modern physics* (Fifth edition, Global edition). Pearson Education Limited. https://elibrary.pearson.de/book/99.150005/9781292440354

Giglio, M., Olivieri, M., Sukhinets, A., Di Gioia, M., Elefante, A., Menduni, G., Zifarelli, A., Patimisco, P., Sampaolo, A., & Spagnolo, V. (2022). Measurement of the methane isotopologues relaxation rate exploiting quartz-enhanced photoacoustic spectroscopy. In M. Razeghi (Ed.), *Quantum sensing and nano electronics and photonics xviii* (p. 56). SPIE / International Society for Optical Engineering. https://doi.org/10.1117/12.2608851

Gordon, I. E., Rothman, L. S., Hargreaves, R. J., Hashemi, R., Karlovets, E. V., Skinner, F. M., Conway, E. K., Hill, C., Kochanov, R. V., Tan, Y., Wcisło, P., Finenko, A. A., Nelson, K., Bernath, P. F., Birk, M., Boudon, V., Campargue, A., Chance, K. V., Coustenis, A., … Yurchenko, S. N. (2022). The hitran2020 molecular spectroscopic database. *Journal of Quantitative Spectroscopy and Radiative Transfer*, *277*, 107949. https://doi.org/10.1016/j.jqsrt.2021.107949

Haghi, R. K., Yang, J., & Tohidi, B. (2017). Fourier transform near-infrared (ftnir) spectroscopy and partial least-squares (pls) algorithm for monitoring compositional changes in hydrocarbon gases under in situ pressure. *Energy & Fuels*, *31*(9), 10245–10259. https://doi.org/10.1021/acs.energyfuels.7b01677

Hammer, G., Lübcke, T., Kettner, R., Pillarella, M. R., Recknagel, H., Commichau, A., Neumann, H.-.-J., & Paczynska–Lahme, B. (2003). Natural gas. In M. Bohnet & F. Ullmann (Eds.), *Ullmann's encyclopedia of industrial chemistry* (6., completely revised ed.). Wiley-VCH. https://doi.org/10.1002/14356007.a17_073.pub2

HITRAN. (2022). *Hitran on the web*. Retrieved July 12, 2022, from https://hitran.iao.ru/

Howarth, R. W. (2019). Ideas and perspectives: Is shale gas a major driver of recent increase in global atmospheric methane? *Biogeosciences*, *16*(15), 3033–3046. https://doi.org/10.5194/bg-16-3033-2019

IEA. (2023). *Methane tracker 2020 – analysis - iea* [Copyright: (c) 2023 IEA]. Retrieved August 10, 2023, from https://www.iea.org/reports/methane-tracker-2020

ISO (Ed.). (2012, May 1). Natural gas — determination of composition and associated uncertainty by gas chromatography — part 1: General guidelines and calculation of composition. Retrieved August 31, 2023, from https://www.iso.org/standard/55839.html

Iwaszenko, S., Kalisz, P., Slota, M., & Rudzki, A. (2021). Detection of natural gas leakages using a laser-based methane sensor and uav. *Remote Sensing*, *13*(3), 510. https://doi.org/10.3390/rs13030510

Jacobson, M. Z. (2021). *100% clean, renewable energy and storage for everything* [Jacobson, Mark Z. (VerfasserIn)]. Cambridge University Press.

JPL. (2022). *Https://spec.jpl.nasa.gov*. Retrieved August 16, 2023, from https://spec.jpl.nasa.gov/

Karpash, O., Darvay, I., & Karpash, M. (2010). New approach to natural gas quality determination [PII: S0920410510000033]. *Journal of Petroleum Science and Engineering*, *71*(3-4), 133–137. https://doi.org/10.1016/j.petrol.2009.12.012

Kiefer, J., Seeger, T., Steuer, S., Schorsch, S., Weikl, M. C., & Leipertz, A. (2008). Design and characterization of a raman-scattering-based sensor system for temporally resolved gas analysis and its application in a gas turbine power plant [PII: S0957-0233(08)79148-3]. *Measurement Science and Technology*, *19*(8), 085408. https://doi.org/10.1088/0957-0233/19/8/085408

Kosterev, A. A., Bakhirkin, Y. A., Curl, R. F., & Tittel, F. K. (2002). Quartz-enhanced photoacoustic spectroscopy [Journal Article]. *Optics Letters*, *27*(21), 1902–1904. https://doi.org/10.1364/ol.27.001902

Kull, H.-J. (Ed.). (2010). *Laserphysik: Physikalische grundlagen des laserlichts und seine wechselwirkung mit materie* [Kull, Hans-Jörg (VerfasserIn)]. Oldenbourg Verlag.

Lackner, M. (2007). Tunable diode laser absorption spectroscopy (tdlas) in the process industries – a review. *Reviews in Chemical Engineering*, *23*(2). https://doi.org/10.1515/REVCE.2007.23.2.65

Leicher, J., Giese, A., Görner, K., Werschy, M., Krause, H., & Dörr, H. (2017). Natural gas quality fluctuations – surveys and statistics on the situation in germany [PII: S1876610217327315]. *Energy Procedia*, *120*, 165–172. https://doi.org/10.1016/j.egypro.2017.07.161

Li, X., Liang, J., Lin, S., Zimin, Y., Zhang, Y., & Ueda, T. (2012). Nir spectrum analysis of natural gas based on hollow-core photonic bandgap fiber. *IEEE Sensors Journal*, *12*(7), 2362–2367. https://doi.org/10.1109/JSEN.2012.2188099

Loh, A., & Wolff, M. (2017). Absorption cross sections of 13c ethane and propane isotopologues in the 3 µm region [PII: S002240731730081X]. *Journal of Quantitative Spectroscopy and Radiative Transfer*, *203*, 517–521. https://doi.org/10.1016/j.jqsrt.2017.05.012

Loh, A., & Wolff, M. (2019a). High resolution spectra of 13c ethane and propane isotopologues photoacoustically measured using interband cascade lasers near 3.33 and 3.38 µm, respectively [PII: S0022407318309038]. *Journal of Quantitative Spectroscopy and Radiative Transfer*, *227*, 111–116. https://doi.org/10.1016/j.jqsrt.2019.01.027

Loh, A., & Wolff, M. (Eds.). (2019b). *Photoacoustic detection of short-chained hydrocarbon isotopologues* [PII: proceedings2019015023]. MDPI. https://doi.org/10.3390/proceedings2019015023

Loh, A., & Wolff, M. (2020). Multivariate analysis of photoacoustic spectra for the detection of short-chained hydrocarbon isotopologues [Journal Article]. *Molecules (Basel, Switzerland)*, *25*(9). https://doi.org/10.3390/molecules25092266

Luo, P., Harrist, J., Menduni, G., Mesdour, R., StMichel, N., & Sampaolo, A. (2022). Simultaneous detection of methane, ethane, and propane by qepas sensors for on-site hydrocarbon characterization and production monitoring. *ACS Omega*, *7*(4), 3395–3406. https://doi.org/10.1021/acsomega.1c05645

Ma, Y. (2018). Review of recent advances in qepas-based trace gas sensing. *Applied Sciences*, *8*(10), 1822. https://doi.org/10.3390/app8101822

MATLAB. (2022). *Https://de.mathworks.com/products/matlab.html* (The MathWorks, Inc., MATLAB, Ed.). Retrieved August 16, 2023, from https://de.mathworks.com/products/matlab.html

McGregor, C., Nimmo, J., & Stothers, W. (2011). Fundamentals of university mathematics [McGregor, Colin (Auteur.) Nimmo, Jonathan (Auteur.) Stothers, Wilson (Auteur.)]. https://doi.org/10.1533/9780857092243

Meiners, H. G., Denneborg, M., Müller, F., Bergmann, A., Weber, F.-A., Dopp, E., Hansen, C., Schüth, C., Gaßner, H., Buchholz, G., Sass, I., Homuth, S., & Priebs, R. (2013). Environmental impacts of fracking related to exploration and exploitation of unconventional natural gas depostits: Risk assessment, recommendations for action and evaluation of relevant existing legal provisions and administrative structures. Retrieved September 5, 2023, from https://www.umweltbundesamt.de/sites/default/files/medien/378/publikationen/texte_83_2013_environmental_impacts_of_fracking.pdf

Menduni, G., Zifarelli, A., Sampaolo, A., Patimisco, P., Giglio, M., Amoroso, N., Wu, H., Dong, L., Bellotti, R., & Spagnolo, V. (2022). High-concentration methane and ethane qepas detection employing partial least squares regression to filter out energy relaxation dependence on gas matrix composition. *Photoacoustics*, *26*, 100349. https://doi.org/10.1016/j.pacs.2022.100349

Meyer, J., Bewley, W., Canedy, C., Kim, C., Kim, M., Merritt, C., & Vurgaftman, I. (2020). The interband cascade laser [PII: photonics7030075]. *Photonics*, *7*(3), 75. https://doi.org/10.3390/photonics7030075

Miklós, A., & Hess, P. (2000). Peer reviewed: Modulated and pulsed photoacoustics in trace gas analysis. *Analytical Chemistry*, *72*(1), 30 A–37 A. https://doi.org/10.1021/ac002681m

Moses, J. I., Cavalié, T., Fletcher, L. N., & Roman, M. T. (2020). Atmospheric chemistry on uranus and neptune [Journal Article]. *Philosophical transactions. Series A, Mathematical, physical, and engineering sciences*, *378*(2187), 20190477. https://doi.org/10.1098/rsta.2019.0477

Mueller-Elektronik AG. (2023). *Gas sensor methane (ir)*. Retrieved October 24, 2023, from https://www.mueller-elektronik.ch/en/gas-warning-systems/gas-sensors/me-1250/flammable-gases/methane/methane-ir/

nanoplus. (2023). *Nanoplus dfb interband cascade lasers (icl): 2800 nm - 4000 nm* (nanoplus Nanosystems and Technologies GmbH, Ed.). Retrieved August 16, 2023, from https://nanoplus.com/fileadmin/user_upload/Data_sheets/nanoplus_DFB_Standard_2800-4000nm.pdf

NIST. (2022). *Https://webbook.nist.gov/chemistry*. Retrieved August 16, 2023, from https://webbook.nist.gov/chemistry/

NLIR. (2022). *S2050 mid-infrared spectrometer data sheet* (NLIR, Ed.). Retrieved August 17, 2023, from https://nlir.com/wp-content/uploads/NLIR-S2050-MIR-Spectrometer-Datasheet-5.pdf

Nodov, E. (1978). Optimization of resonant cell design for optoacoustic gas spectroscopy (h-type) [Journal Article]. *Applied optics*, *17*(7), 1110–1119. https://doi.org/10.1364/AO.17.001110

Our World in Data. (2022). *Global direct primary energy consumption*. Retrieved August 14, 2023, from https://ourworldindata.org/grapher/global-primary-energy?stackMode=relative

Palzer, S. (2020). Photoacoustic-based gas sensing: A review [Journal Article Review Journal Article Review]. *Sensors (Basel, Switzerland)*, *20*(9). https://doi.org/10.3390/s20092745

Pană, I., Gheţiu, I. V., Stan, I. G., Dinu, F., Brănoiu, G., & Suditu, S. (2022). The use of hydraulic fracturing in stimulation of the oil and gas wells in romania. *Sustainability*, *14*(9), 5614. https://doi.org/10.3390/su14095614

Pandey, S., van Nistelrooij, M., Maasakkers, J. D., Sutar, P., Houweling, S., Varon, D. J., Tol, P., Gains, D., Worden, J., & Aben, I. (2023). Daily detection and quantification of methane leaks using sentinel-3: A tiered satellite observation approach with sentinel-2 and sentinel-5p. *Remote Sensing of Environment*, *296*, 113716. https://doi.org/10.1016/j.rse.2023.113716

Park, C., Oh, S., Kim, C., Choi, Y., & Ha, Y. (2021). Effect of natural gas composition and gas interchangeability on performance and emission characteristics in an air–fuel controlled natural gas engine. *Fuel*, *287*, 119501. https://doi.org/10.1016/j.fuel.2020.119501

Paulus, N., & Lemort, V. (2023). Establishing the energy content of natural gas residential consumption : Example with belgian field-test applications. *IOP Conference Series: Earth and Environmental Science*, *1185*(1), 012013. https://doi.org/10.1088/1755-1315/1185/1/012013

Peatross, J., & Ware, M. (2015). *Physics of light and optics (black & white)*. https://optics.byu.edu/docs/opticsbook.pdf

Petrov, D. V., Matrosov, I. I., Zaripov, A. R., & Tanichev, A. S. (2022). Raman natural gas analyzer: Effects of composition on measurement precision [Journal Article The authors declare no conflict of interest.]. *Sensors*, *22*(9), 3492. https://doi.org/10.3390/s22093492

PICARRO, INC. (2022). *G2210-i analyzer datasheet | picarro* (PICARRO, INC., Ed.). Retrieved August 16, 2023, from https://www.picarro.com/support/library/documents/g2210i_analyzer_datasheet

Pollack, J. B., Hubickyj, O., Bodenheimer, P., Lissauer, J. J., Podolak, M., & Greenzweig, Y. (1996). Formation of the giant planets by concurrent

accretion of solids and gas [PII: S0019103596901906]. *Icarus*, *124*(1), 62–85. https://doi.org/10.1006/icar.1996.0190

Poole, C. (Ed.). (2021). *Gas chromatography (second edition)* (Second edition). Elsevier. https://www.sciencedirect.com/science/book/9780128206751

Press, W. H., & Teukolsky, S. A. (1990). Savitzky-golay smoothing filters. *Computers in Physics*, *4*(6), 669. https://doi.org/10.1063/1.4822961

R. Seeley, M. F. (2019). *High precision wavelength measurement and control of a tunable laser*. https://patents.google.com/patent/us10502632b2/en

Reference and intercomparison materials for stable isotopes of light elements. proceedings of a consultants meeting held in vienna, 1-3 december 1993. (1995). https://www.osti.gov/etdeweb/biblio/195611

Rhoderick, G. C. (2003). Analysis of natural gas: The necessity of multiple standards for calibration [Journal Article]. *Journal of Chromatography A*, *1017*(1-2), 131–139. https://doi.org/10.1016/j.chroma.2003.08.002

Rodrigues, C., Maia, R., Lauteri, M., Brugnoli, E., & Máguas, C. (2013). Chapter 4 - stable isotope analysis. In M. de La Guardia & A. Gonzálvez (Eds.), *Comprehensive analytical chemistry : Food protected designation of origin* (pp. 77–99, Vol. 60). Elsevier. https://doi.org/10.1016/B978-0-444-59562-1.00004-9

Rosipal, R., & Krämer, N. (2006). Overview and recent advances in partial least squares, 34–51. https://doi.org/10.1007/11752790_2

Saalberg, Y., & Wolff, M. (2018). Multivariate analysis as a tool to identify concentrations from strongly overlapping gas spectra [Journal Article The authors declare no conflict of interest. Journal Article The authors declare no conflict of interest.]. *Sensors (Basel, Switzerland)*, *18*(5). https://doi.org/10.3390/s18051562

Sampaolo, A., Patimisco, P., Giglio, M., Zifarelli, A., Wu, H., Dong, L., & Spagnolo, V. (2022). Quartz-enhanced photoacoustic spectroscopy for multi-gas detection: A review [Journal Article Review Declaration of competing interest The authors declare that they have no known competing financial interests or personal relationships that could have appeared to influence the work reported in this paper.]. *Analytica Chimica Acta*, *1202*, 338894. https://doi.org/10.1016/j.aca.2021.338894

Schilt, S., Besson, J.-P., & Thévenaz, L. (2006). Near-infrared laser photoacoustic detection of methane: The impact of molecular relaxation. *Applied Physics B*, *82*(2), 319–328. https://doi.org/10.1007/s00340-005-2076-y

Schroll, M., Keppler, F., Greule, M., Eckhardt, C., Zorn, H., & Lenhart, K. (2020). The stable carbon isotope signature of methane produced by

saprotrophic fungi. *Biogeosciences*, *17*(14), 3891–3901. https://doi.org/10.5194/bg-17-3891-2020

Schuldt, T., Kraus, H.-J., Weise, D., Braxmaier, C., Peters, A., & Johann, U. (2017). A heterodyne interferometer for high resolution translation and tilt measurement as optical readout for the lisa inertial sensor. In SPIE (Ed.). T. Schuldt, H.-J. Kraus, D. Weise, C. Braxmaier, A. Peters, & U. Johann (Eds.), *International conference on space optics 2006 - cso 2006*. SPIE. https://doi.org/10.1117/12.2308065

Schwietzke, S., Sherwood, O. A., Bruhwiler, L. M. P., Miller, J. B., Etiope, G., Dlugokencky, E. J., Michel, S. E., Arling, V. A., Vaughn, B. H., White, J. W. C., & Tans, P. P. (2016). Upward revision of global fossil fuel methane emissions based on isotope database [Journal Article Research Support, Non-U.S. Gov't]. *Nature*, *538*(7623), 88–91. https://doi.org/10.1038/nature19797

Selvaraj, R., Vasa, N. J., & Shiva Nagendra, S. M. (2019). Off-resonant photoacoustic spectroscopy for analysis of multicomponent gas mixtures at high concentrations using broadband vibrational overtones of individual gas species [Journal Article]. *Applied optics*, *58*(15), 4118–4126. https://doi.org/10.1364/AO.58.004118

Sessions, A. L. (2006). Isotope-ratio detection for gas chromatography [Journal Article Research Support, U.S. Gov't, Non-P.H.S. Review]. *Journal of separation science*, *29*(12), 1946–1961. https://doi.org/10.1002/jssc.200600002

Sigrist, M. W. (1995). Trace gas monitoring by laser-photoacoustic spectroscopy. *Infrared Physics & Technology*, *36*(1), 415–425. https://doi.org/10.1016/1350-4495(94)00093-Z

Smith, B. C. (2011). *Fundamentals of fourier transform infrared spectroscopy* (2nd ed.) [Smith, Brian C., (author.)]. CRC Press. https://doi.org/10.1201/b10777

Steel, W. H. (1983). *Interferometry* (2. ed.). Univ. Pr.

Stewart, G. (2021). *Laser and fiber optic gas absorption spectroscopy* [Stewart, George, (author.)]. Cambridge University Press. https://doi.org/10.1017/9781316795637

Tomberg, T., Vainio, M., Hieta, T., & Halonen, L. (2018). Sub-parts-per-trillion level sensitivity in trace gas detection by cantilever-enhanced photoacoustic spectroscopy [Journal Article Research Support, Non-U.S. Gov't The authors declare that they have no competing interests.]. *Scientific Reports*, *8*(1), 1848. https://doi.org/10.1038/s41598-018-20087-9

van Amstel, A. (2012). Methane. a review. *Journal of Integrative Environmental Sciences*, *9*(sup1), 5–30. https://doi.org/10.1080/1943815X.2012.694892

Veracious Statistics Research. (2021). *Global laser wavelength meters research report 2021*. https://vstatisticsresearch.com/global-laser-wavelength-meters-market

Vialar. (2016). *Handbook of mathematics*. HDBoM.

Vurgaftman, I., Weih, R., Kamp, M., Meyer, J. R., Canedy, C. L., Kim, C. S., Kim, M., Bewley, W. W., Merritt, C. D., Abell, J., & Höfling, S. (2015). Interband cascade lasers. *Journal of Physics D: Applied Physics*, *48*(12), 123001. https://doi.org/10.1088/0022-3727/48/12/123001

Wang, Z. L., Tian, C. W., Liu, Q., Chang, J., Zhang, Q. D., & Zhu, C. G. (2018). Wavelength modulation technique-based photoacoustic spectroscopy for multipoint gas sensing [Journal Article]. *Applied optics*, *57*(11), 2909–2914. https://doi.org/10.1364/AO.57.002909

Wei, Z., Li, M., Li, S., Wang, R., & Wang, C. (2021). Development of natural gas chemical kinetic mechanisms and application in engines: A review [Journal Article Review The authors declare no competing financial interest. Journal Article Review The authors declare no competing financial interest.]. *ACS Omega*, *6*(37), 23643–23653. https://doi.org/10.1021/acsomega.1c03197

Werle, P., Slemr, F., Maurer, K., Kormann, R., Mücke, R., & Jänker, B. (2002). Near- and mid-infrared laser-optical sensors for gas analysis. *Optics and Lasers in Engineering*, *37*(2-3), 101–114. https://doi.org/10.1016/S0143-8166(01)00092-6

Wiersberg, T., & Erzinger, J. (2007). Real-time mud gas monitoring: A technique to obtain information on the composition and distribution of gases at depth while drilling. *Scientific Drilling*, *SpecialIssue*(Special, No. 1), 71–72. https://doi.org/10.2204/iodp.sd.s01.36.2007

Yoon, T. H., Hamedi, S., & Olyaee, S. (2009). Jones matrix analysis of frequency mixing error in three-longitudinal-mode laser heterodyne interferometer. *IET Optoelectronics*, *3*(5), 215–224. https://doi.org/10.1049/iet-opt.2009.0015

Zeller, W., Naehle, L., Fuchs, P., Gerschuetz, F., Hildebrandt, L., & Koeth, J. (2010). Dfb lasers between 760 nm and 16 um for sensing applications [Journal Article Research Support, Non-U.S. Gov't]. *Sensors*, *10*(4), 2492–2510. https://doi.org/10.3390/s100402492

Zeninari, V., Vallon, R., Risser, C., & Parvitte, B. (2016). Photoacoustic detection of methane in large concentrations with a helmholtz sensor: Simulation and experimentation [PII: 2018]. *International Journal of Thermophysics*, *37*(1), 1–11. https://doi.org/10.1007/s10765-015-2018-9

Zhang, T., & Krooss, B. M. (2001). Experimental investigation on the carbon isotope fractionation of methane during gas migration by diffusion through sedimentary rocks at elevated temperature and pressure [PII: S0016703701006019]. *Geochimica et Cosmochimica Acta*, *65*(16), 2723–2742. https://doi.org/10.1016/S0016-7037(01)00601-9

Zifarelli, A., Giglio, M., Menduni, G., Sampaolo, A., Patimisco, P., Passaro, V. M. N., Wu, H., Dong, L., & Spagnolo, V. (2020). Partial least-squares regression as a tool to retrieve gas concentrations in mixtures detected using quartz-enhanced photoacoustic spectroscopy. *Analytical Chemistry*, *92*(16), 11035–11043. https://doi.org/10.1021/acs.analchem.0c00075